

**The Nonlinear Optical Properties of GaAs/AlAs
Superlattice-Core Waveguides at
Telecommunications Wavelengths**

Second Edition

Sean J. Wagner

Copyright © 2008 Sean J. Wagner

NOTICE

This document has not been submitted for academic credit and does not necessarily conform to the requirements for a degree. It is an update to the original thesis published by the author. It contains corrections that have not received formal evaluation and scrutiny by the University of Toronto or any other institution. The original thesis may be obtained from the University of Toronto library or the Canadian National Archives.

Abstract

The Nonlinear Optical Properties of GaAs/AlAs Superlattice-Core Waveguides at
Telecommunications Wavelengths

Sean J. Wagner

Master of Applied Science

Graduate Department of the

Edward S. Rogers Sr. Department of Electrical and Computer Engineering

University of Toronto

2006

This thesis examines the nonlinear optical properties of 14:14 GaAs/AlAs superlattice-core waveguides at wavelengths in the 1550 nm telecommunications range. The linear optical properties of as-grown superlattice show polarization dependencies that are attributed to the difference in the half-bandgap for TE and TM polarizations and the structural anisotropy of the superlattice. Two-photon absorption measurements in as-grown superlattice yielded polarization-dependent coefficients between 1.5 cm/W to 4.0 cm/W, which are larger than in bulk AlGaAs. Spectral broadening induced by self-phase modulation was observed to give nonlinear refraction coefficients n_2 of 1.5 cm²/W to 5.5 cm²/W with TE modes having values as much as twice as large as the TM mode. The ratio of self- to cross-phase modulation between polarizations showed a polarization dependence. Intermixing superlattice resulted in a reduction in n_2 by one order of magnitude. Figure of merit values show superlattice is a viable material for nonlinear optical devices.

Revision History

Aug. 13, 2007	<ul style="list-style-type: none">• Corrected Table 2.2, Intermixed TM “B” polynomial value• Corrected Figure 3.6 with expanded error bars• Corrected Equations 4.30, 4.31, 4.33 with “j” in front of group velocity terms
---------------	--

Acknowledgements

First and foremost, I would like to thank my supervisors, Prof. J. Stewart Aitchison and Prof. Amr Helmy. Their support, resources, advice, experience, and guidance were instrumental in the completion of this work. Discussions with them were helpful and insightful. I look forward to continuing my studies with both of them.

Many thanks and much appreciation are owed to Prof. David C. Hutchings and Prof. Marc Sorel, both of the University of Glasgow. They provided the superlattice samples that were characterized in this thesis. Without their generosity, this work would not have been possible. Furthermore, Prof. Hutchings provided theoretical data that was necessary in the predictions of the properties of superlattice. Discussions with Prof. Hutchings either in person or via E-mail helped a great deal.

Dr. Daniele Modotto of the Università di Brescia deserves much appreciation for his contributions to this work. Dr. Modotto's BPM simulation code for SPM was instrumental for quantifying the nonlinear properties of superlattice. Without it, this work would not have been possible.

I would also like to extend my gratitude to several of my fellow students and colleagues who carried out some of the work that was used in this thesis. Dr. Joachim Meier helped immensely by setting up and maintaining the laboratory facilities that were used in the experiments. Dr. Meier also provided much guidance on laboratory practices and nonlinear optics theory. Aaron Zilkie also helped out with much of the laboratory work and my discussions with him were always helpful. Phil Scrutton measured the photoluminescence of the superlattice samples and his data led to many of the conclusions reached in this thesis. Brian Fung provided new intermixed superlattice samples that will be studied at a later date and his efforts are appreciated. Dr. Sonia Garcia-Blanco and Dr. Henry Lee both deserve my gratitude for instructing me on how to fabricate microchips in the cleanroom. Thank you as well to Rajiv Iyer and Kevin Vora

for their many insightful discussions, helpful advice, and work in the laboratory and in the cleanroom.

I would like to thank my committee member Prof. Tony Chan Carusone, Prof. Li Qian, and Prof. John Sipe for volunteering their time and efforts. I also extend my gratitude to the department for their financial support through fellowships and teaching assistantships.

Lastly, to my friends and family, your support in this endeavor was very much appreciated and I am forever grateful.

Contents

LIST OF FIGURES	x
LIST OF TABLES	xv
CHAPTER 1: INTRODUCTION	1
1.1 INTRODUCTION TO THESIS AND MOTIVATION	1
1.2 NONLINEAR OPTICS	3
1.3 NONLINEAR OPTICS IN SEMICONDUCTORS	5
1.4 SUPERLATTICE AND QUANTUM WELL INTERMIXING	6
1.5 OUTLINE OF THESIS	11
CHAPTER 2: LINEAR OPTICAL PROPERTIES OF SUPERLATTICE WAVEGUIDES	12
2.1 INTRODUCTION	12
2.2 WAFER STRUCTURE	13
2.3 PHOTOLUMINESCENCE	14
2.4 LINEAR REFRACTIVE INDEX	17
2.4.1 Refractive Index Models for As-grown Superlattice	18
2.4.2 Back-calculation of Measured Index	20
2.5 WAVEGUIDE PROPERTIES	22
2.5.1 Sample Fabrication	22
2.5.2 Mode Profiles and Confinement Factor	23
2.5.3 Mode Effective Index and Group Velocity Dispersion	26
2.6 LINEAR LOSS	31
2.6.1 Experimental Methods	31
2.6.2 Results	33
2.7 CONCLUSIONS	36

CHAPTER 3: NONLINEAR ABSORPTION IN AS-GROWN AND INTERMIXED SUPERLATTICE

3.1	INTRODUCTION	37
3.2	TWO-PHOTON ABSORPTION IN AS-GROWN SUPERLATTICE	38
3.2.1	Theory	38
3.2.2	Previous Studies of TPA in Semiconductors	42
3.2.3	Experimental Methods	43
3.2.4	Contribution of AlGaAs Buffer and Cladding Layers	45
3.2.5	Calculation of Third-order Effective Area	47
3.2.6	Results	48
3.3	THREE-PHOTON ABSORPTION IN INTERMIXED SUPERLATTICE	50
3.3.1	Theory	50
3.3.2	Previous Studies of 3PA in Semiconductors	52
3.3.3	Calculation of Fifth-order Effective Area and Contribution of Bulk Layers	53
3.3.4	Results	54
3.3.5	Comparison of 3PA to Other Sources of Optical Loss	56
3.4	RE-EMISSION FROM NONLINEAR ABSORPTION	57
3.5	CONCLUSIONS	58

CHAPTER 4: NONLINEAR REFRACTION BY SELF- AND CROSS-PHASE MODULATION

4.1	INTRODUCTION	60
4.2	SELF-PHASE MODULATION IN AS-GROWN AND INTERMIXED SUPERLATTICE	61
4.2.1	Background Theory on Self-Phase Modulation and Spectral Broadening	61
4.2.2	Previous Studies of SPM in Semiconductors	66
4.2.3	Nonlinear Refraction in the Buffer and Cladding Layers	68
4.2.4	Theoretical Predictions for Superlattice	73
4.2.5	Experimental Methods	76
4.2.6	Computer Simulation by the Split-step Fourier Method	77
4.2.7	Results for As-grown Superlattice	79
4.2.8	Results for Intermixed Superlattice	84
4.3	CROSS-PHASE MODULATION IN AS-GROWN SUPERLATTICE	85
4.3.1	Theory	85
4.3.2	Previous Studies of XPM in Semiconductors	88

4.3.3	Theoretical Predictions for Superlattice	88
4.3.4	Experimental Methods	90
4.3.5	Measured Results	91
4.4	CONCLUSIONS	94
CHAPTER 5: APPLICATIONS OF SUPERLATTICE TO NONLINEAR OPTICAL SIGNAL PROCESSING DEVICES		96
5.1	INTRODUCTION	96
5.2	FIGURE OF MERIT	97
5.3	NONLINEAR DIRECTIONAL COUPLER	99
5.4	NONLINEAR MACH-ZEHNDER INTERFEROMETER	101
5.5	CONCLUSIONS	103
CHAPTER 6: CONCLUSIONS		104
6.1	SUMMARY	104
6.2	FUTURE WORK	107
APPENDIX A: QUANTUM WELL ENERGY CALCULATIONS		109
APPENDIX B: MATLAB CODE FOR THE SPLIT-STEP FOURIER METHOD		123
REFERENCES		137

List of Figures

- Figure 1.1: Example of a photonic integrated circuit (PIC) with linear waveguides, a nonlinear directional coupler (NLDC), a nonlinear Mach-Zehnder interferometer (NLMZI), a nonlinear microring resonators (NMR), a quasi-phase matched grating (QPM), and a laser source 2
- Figure 1.2: Layer stack of a compositional superlattice. A periodic set of coupled quantum wells form as shown on the right. 7
- Figure 1.3: Electronic band structure of a superlattice. The solid black lines represent the conduction and valence band edges of the well and barrier materials. The grey areas represent the superlattice minibands formed due to strong coupling between quantum wells. 8
- Figure 1.4: Quantum-well intermixing process. The material undergoes disordering which creates defects and interstitials. After annealing, interdiffusion causes the interfaces between the two materials (GaAs and AlAs) to smear resulting in an altered bandstructure and larger bandgap. 9
- Figure 2.1: GaAs/AlAs superlattice wafer structure 13
- Figure 2.2: Traces of the photoluminescence peak across the as-grown superlattice wafer cross-section for the TE polarization and TM polarization. The top of the wafer is on the right side. 15
- Figure 2.3: Unintended GaAs quantum well at ends of superlattice core layer. 16
- Figure 2.4: Traces of the photoluminescence peak across the intermixed superlattice wafer cross-section for the TE polarization and TM polarization. The top of the wafer is on the right side. 17

Figure 2.5: Predicted values of the refractive index of superlattice for the TE and TM polarizations based on the form birefringence model using the bulk AlGaAs index models of Gehrsitz and Adachi. Values produced by the Deri model are virtually identical to the values produced by the Gehrsitz model.	19
Figure 2.6: Back-calculated values of the measured refractive index of as-grown superlattice for a) TE and b) TM modes. Also shown are predicted values using the Gehrsitz and Adachi models.	21
Figure 2.7: Back-calculated index of refraction values for intermixed superlattice. Also shown are index values for $\text{Al}_{0.50}\text{Ga}_{0.50}\text{As}$ calculated from the Gehrsitz model	22
Figure 2.8: Superlattice rib waveguide structure	23
Figure 2.9: Photographs of a) as-grown and b) intermixed superlattice waveguides taken under a microscope at 500x magnification.	23
Figure 2.10: Mode profiles of as-grown superlattice rib waveguides at 1550 nm for the a) TE mode and b) TM mode.	24
Figure 2.11: Rib waveguide confinement factor	25
Figure 2.12: Effective index of refraction for 3.0 μm -wide rib waveguides	27
Figure 2.13: Linear birefringence for superlattice-core rib waveguides	28
Figure 2.14: Group velocity mismatch between the TE and TM polarizations for rib waveguides	29
Figure 2.15: Group velocity dispersion for rib waveguides	30
Figure 2.16: Experimental setup for Fabry-Perot loss measurement	32
Figure 2.17: Fabry-Perot transmission spectrum around 1545 nm in the TE mode for as-grown superlattice.	33
Figure 2.18: Spectral dependence of linear loss coefficients for 1.2 cm-long as-grown superlattice rib waveguides	34

Figure 2.19: Spectral dependence of linear loss coefficients for 0.5 cm-long intermixed superlattice rib waveguides	35
Figure 3.1: Band structure of a typical semiconductor showing direct and indirect electron transitions by TPA. Reproduced from [50].	38
Figure 3.2: Experimental setup for measurement of nonlinear optical properties of superlattice waveguides using an OPO-based ultrafast laser system	44
Figure 3.3: Measured inverse transmission of an as-grown superlattice waveguide at 1525 nm in the TE mode	45
Figure 3.4: Measured TPA coefficients for bulk $\text{Al}_{0.18}\text{Ga}_{0.82}\text{As}$ [20], and scaled values for $\text{Al}_{0.56}\text{Ga}_{0.44}\text{As}$ and $\text{Al}_{0.60}\text{Ga}_{0.40}\text{As}$	46
Figure 3.5: Core third-order effective mode area for as-grown superlattice rib waveguides	47
Figure 3.6: Dispersion of the TPA coefficients for as-grown superlattice below the half-bandgap	49
Figure 3.7: Three-photon absorption process between valence and conduction band. Reproduced from [50].	50
Figure 3.8: Fifth-order core nonlinear effective areas for intermixed superlattice rib waveguides	54
Figure 3.9: Measured inverse transmission squared curve for intermixed superlattice with TM polarized light at 1550 nm	55
Figure 3.10: Measured 3PA values for intermixed superlattice	56
Figure 3.11: Re-emission spectra from recombination of carrier generated by nonlinear absorption.	58
Figure 4.1: SPM-induced frequency shifts by the rising (top) and falling (bottom) edges of an optical pulse	64
Figure 4.2: Spectral broadening patterns and associated phase shifts for a Gaussian pulse. Replicated from Ref. [3]	64

Figure 4.3: Spectral dependence of n_2 for $\text{Al}_{0.56}\text{Ga}_{0.44}\text{As}$ and $\text{Al}_{0.60}\text{Ga}_{0.40}\text{As}$ scaled from measured values of $\text{Al}_{0.18}\text{Ga}_{0.82}\text{As}$	69
Figure 4.4: Cladding third-order effective area for as-grown superlattice waveguides	72
Figure 4.5: Waveguide third-order effective area for as-grown superlattice waveguides.	73
Figure 4.6: Theoretical n_2 values for as-grown superlattice calculated from Ref. [28]	74
Figure 4.7: Theoretical n_2 values for intermixed superlattice calculated from Ref. [28]	75
Figure 4.8: Spectral broadening pattern with increasing input power at 1545 nm in as-grown superlattice waveguides for the TE mode (top) and TM mode (bottom)	80
Figure 4.9: Nonlinear refraction coefficients for as-grown superlattice calculated from measured data using the simple modeling method. Values shown underestimate the value of n_2 since dispersion and nonlinear absorption are not accounted for. Thus, n_2 values from the more comprehensive model should be used instead.	81
Figure 4.10: Simulated spectral broadening in an as-grown superlattice waveguide for the TE mode at 1545 nm	82
Figure 4.11: Measured nonlinear refraction coefficients for SPM in as-grown superlattice produced by numerical solutions to the GNLSE	83
Figure 4.12: XPM-induced frequency shifts on co-propagating pulses shifted from each other in time by group velocity mismatch	86
Figure 4.13: Theoretical n_{χ^2} values for as-grown superlattice calculated from Ref. [28]	89
Figure 4.14: Theoretical XPM/SPM ratios for as-grown superlattice calculated from Ref. [28]	89
Figure 4.15: Measured XPM-induced spectral broadening on a TE probe by a TM pump at a wavelength of 1545 nm	91

Figure 4.16: Simulated XPM-induced spectral broadening of TE probe acted on by TM pump for as-grown superlattice at 1545 nm	92
Figure 4.17: Measured nonlinear refraction coefficients for XPM in as-grown superlattice	93
Figure 4.18: Measured XPM/SPM ratios for as-grown superlattice	94
Figure 5.1: TPA Figure of merit for as-grown superlattice	98
Figure 5.2: Schematic of a directional coupler	99
Figure 5.3: Output switching fraction versus input power for an NLDC with different T values [76]	100
Figure 5.4: Required switching power versus figure of merit for a NLDC [76]	101
Figure 5.5: Schematic of a Mach-Zehnder interferometer	102
Figure A.1: GaAs quantum well potential profile with relevant energy quantities	112

List of Tables

Table 2.1: Coefficients for quadratic regression for the index of refraction for TE and TM polarizations in as-grown and intermixed material. The form of the regression is $n = A\lambda^2 + B\lambda + C$ where λ is the wavelength (m).	22
Table 2.2: Coefficients for quadratic regression for the waveguide effective index for TE and TM modes in as-grown and intermixed material. The form of the regression is $n_{eff} = A\lambda^2 + B\lambda + C$ where λ is the wavelength (m).	27
Table 4.1: Parameters for calculation of nonlinear refraction constant for indirect bandgap of AlGaAs buffer and cladding layers	71
Table 4.2: Sources of error in n_2 for as-grown superlattice	84
Table 4.3: Sources of error in n_2 for intermixed superlattice	85
Table 5.1: Figures of merit T in various semiconductors for TPA-dominated loss	98
Table A.1: Parameters for GaAs quantum well calculations. Note that x represents the Al content ratio.	111
Table A.2: Calculated quantities for GaAs ASQWs	112

Chapter 1

Introduction

1.1 Introduction to Thesis and Motivation

Optical telecommunications and data networks continue to improve in performance as new technologies have allowed increased data rates. Future projected demands for high-bandwidth services in data networks will require further improvements in optical technology. However, current optical networks are limited in performance by their dependency on microelectronics. While microelectronics have continued to improve in performance beyond expectations, further scaling of transistors will be limited by the achievable resolution with available fabrication technologies, gate dielectric thickness and materials, and current leakage in deep-submicron device lengths. Thus, the theoretical physical limitations of microelectronics will forbid further improvements in transmission and processing speed. The optics industry has responded as the microelectronics industry has with added parallelism in the form of wavelength division multiplexing (WDM) for increasing the aggregate transmission speed. However, many other functions are still performed by microelectronics and require optical-electrical-optical (OEO) conversions. Thus, it is necessary to develop new technologies based entirely on optics to realize the full potential of optical networks.

Nonlinear optics provides a solution by enabling all-optical components. These devices would provide basic functions such as all-optical signal routing and direct frequency conversions without reliance on electronic components. More advanced operations such as all-optical logic are also possible. Several such devices based on

nonlinear optical effects have been developed such as nonlinear-optical loop mirrors (NOLM) [1] and terahertz optical asymmetric demultiplexers (TOAD) [2]. However, many of these devices are large, expensive, and impractical. It would be beneficial to create compact, low cost devices that can be placed onto the same chip to make photonic integrated circuits (PICs). As shown in Figure 1.1, such chips would have a mix of linear, nonlinear, and active devices. The limitation in achieving this goal has so far been the materials available for nonlinear optics. Most exhibit weak nonlinear effects that require them to be large and unsuitable for integration. For materials that do have large nonlinearities, mixing linear and nonlinear components onto the same chip is problematic and costly. Also, many of these materials cannot be used to create lasers and photodetectors.

In this thesis, an engineered semiconductor called GaAs/AlAs superlattice is evaluated as a material for nonlinear optics. This material has the potential for enabling the creation of complex PICs by allowing the integration of active and passive components onto the same chip. In addition, quantum well intermixing enables patternable changes in the electronic bandgap and nonlinear properties of the superlattice after wafer growth, which is not possible with bulk semiconductors. This allows the creation of unique optical devices based on the modulation of the nonlinear coefficients, and allows for integration of both linear and nonlinear components. As will

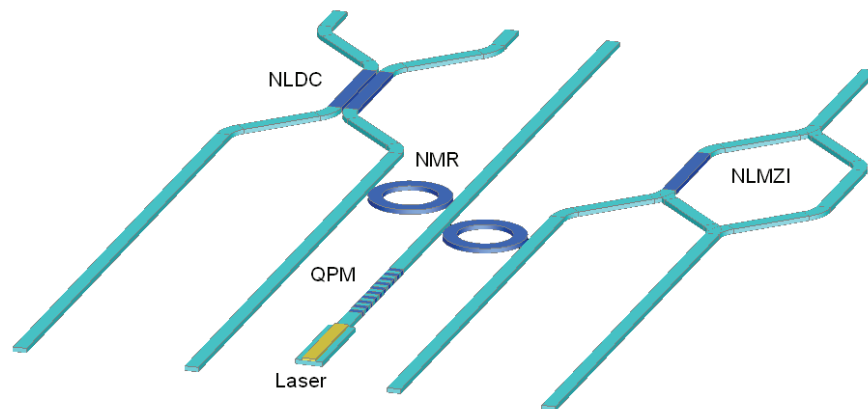


Figure 1.1: Example of a photonic integrated circuit (PIC) with linear waveguides, a nonlinear directional coupler (NLDC), a nonlinear Mach-Zehnder interferometer (NLMZI), a nonlinear microring resonators (NMR), a quasi-phase matched grating (QPM), and a laser source

be shown, superlattice exhibits many unique features and has sufficiently strong nonlinear behaviour to realize compact structures for all-optical switching and signal processing.

1.2 Nonlinear Optics

Nonlinear optical effects in materials are the result of a nonlinear dependence of the polarization density on an applied electric field. In general, this is expressed as [3]

$$\vec{P} = \chi^{(1)} \vec{E} + \chi^{(2)} : \vec{E}\vec{E} + \chi^{(3)} : \vec{E}\vec{E}\vec{E} + \dots \quad (1.1)$$

where \vec{E} is the applied electric field intensity, and $\chi^{(N)}$ is the N -th order electric susceptibility. In general, the electric field and polarization density are vectors and the susceptibilities are tensors of rank $N+1$. The linear response of the material is represented by the term containing the linear susceptibility $\chi^{(1)}$. The subsequent terms represent the nonlinear response. In most materials, nonlinearities of fourth-order or greater are infinitesimal and are usually ignored. However, the terms involving $\chi^{(2)}$ and $\chi^{(3)}$ can be significant at sufficiently high field intensities achievable with high-power lasers. Thus, second-order and third-order nonlinearities lead to several measurable and useful effects.

Second-order nonlinear effects are the result of asymmetry in the crystal structure of a material. For materials that lack inversion symmetry, the $\chi^{(2)}$ tensor elements can be strong enough to cause interactions between both static and time varying fields. Three-wave mixing is a second-order phenomenon in which two optical fields interact to produce a third optical field of a different frequency. This effect is commonly used in parametric wavelength conversion for research laser systems. With further research, three-wave mixing can potentially be used in compact all-optical wavelength conversion devices with wide-ranging applications in telecommunications and sensor systems.

For all-optical switching, third-order nonlinear effects are of great interest. Most notably is the optical Kerr effect. In this nonlinear effect, an intense optical field causes an instantaneous change in the refractive index according to the equation

$$n = n_0 + n_2 I \quad (1.2)$$

where n_0 is the linear index of refraction, n_2 is the Kerr coefficient (also known as the nonlinear index of refraction), and I is the intensity of the optical field. By changing the refractive index, the phase velocity of light changes and the optical field accumulates an extra phase shift. This effect is known as self-phase modulation (SPM) since light causes a phase change on itself. Changes in the refractive index and phase shifts can also be created by a second optical field which is either at a different wavelength or on a different polarization. This type of interaction is called cross-phase modulation (XPM). Such optically-induced phase shifts used in several types of interferometric and dual-mode structures for optical switching [4].

The Kerr effect also allows for a phenomenon known as self-focusing. A beam of light with sufficient intensity can cause a localized increase in the refractive index directly along its path creating a small index contrast with the surrounding material. At a particular power level, the self-focusing effect exactly balances diffraction and the beam travels through the material intact without spreading out. This is known as a spatial soliton. Discrete spatial solitons in waveguide arrays have been demonstrated [5]. Preliminary evidence of soliton emission from an asymmetric waveguide structure has been measured [6]. Spatial solitons have a wide range of possible applications in all-optical switching and beam steering [4].

Multi-photon absorption is an effect related to the odd-numbered nonlinearities. Two or more photons with a total energy equaling the energy gap between two electronic bands can excite an electron from the low energy band to the high energy band. If only the third- and fifth-order nonlinear absorption are accounted for, the total absorption coefficient can be expressed as

$$\alpha = \alpha_0 + \alpha_2 I + \alpha_3 I^2 \quad (1.3)$$

where α_0 is the linear absorption coefficient, α_2 is the third-order nonlinear absorption coefficient, and α_3 is the fifth-order nonlinear absorption coefficient. Third-order nonlinear absorption is related to two-photon absorption (TPA), while fifth-order

nonlinear absorption is related to three-photon absorption (3PA). TPA is strongest at photon energies near to one-half of the bandgap energy. Likewise, 3PA is strongest at photon energies near to one-third of the bandgap energy. Nonlinear absorption is useful for creating certain types of devices such as photodetectors [7], optical limiters [8], and autocorrelators [9]. However, optical losses of any kind are detrimental to devices based on the optical Kerr effect since they limit the optical intensity [10]. Thus, an efficient switching device should minimize the amount of nonlinear absorption in order to maximize the amount of nonlinear index change and phase-shift.

Nonlinear refraction and two-photon absorption are linked to each other by the Kramers-Krönig relations [11]. As a result, n_2 changes rapidly at wavelengths near the peak in α_2 . Thus, it is advantageous to operate a device based on the Kerr effect at wavelengths near the α_2 peak. Above the half-bandgap, TPA in semiconductors is usually large and continually increases with shorter wavelengths. Thus, device operation becomes impractical above the half-bandgap energy. Instead, nonlinear devices should be operated below the half-bandgap where TPA is minimal but close enough to the half-bandgap to take advantage of the enhancement in n_2 .

1.3 Nonlinear Optics in Semiconductors

Semiconductors have several advantages over most dielectrics as nonlinear materials. First, the electronic bandgap in semiconductors is much smaller than in dielectrics. In most cases, materials with smaller bandgaps tend to have large optical nonlinearities [12]. Second, the nonlinear behaviour of a material is enhanced near the electronic resonances [13]. The resonances for common semiconductors fall within photon energies in the visible and near infrared spectral bands. Thus, semiconductors can be used to create compact devices with strong nonlinearities in the spectral ranges useful for telecommunications and spectroscopy. For example, the Kerr effect in crystalline silicon is over 100-times stronger at wavelengths near 1550 nm than in silica. Silicon has been used in several demonstrations of stimulated Raman scattering for lasers [14, 15], electro-optic modulation [16, 17], and all-optical switching in microring resonators [18]. However, its optical bandgap of ~ 1100 nm (1.12 eV) leads to a large amount of nonlinear

absorption for wavelengths near 1550 nm which are typically used in telecommunications systems. Moreover, carrier-induced plasma dispersion effects [19] used to achieve large nonlinear refractive index changes required for all-optical switching and electro-optic modulation operate slowly compared with the instantaneous Kerr effect. Lastly, silicon has an indirect bandgap which makes it impractical for creating optical sources.

The GaAs/Al_xGa_{1-x}As material system has many advantages over other semiconductors. Like several other III-V compound semiconductors, GaAs has a direct bandgap which makes it suitable for creating optical sources. However, unlike other III-V materials such as InP/InGaAsP, all compositions of Al_xGa_{1-x}As from GaAs to AlAs are lattice matched. Thus, it is possible to grow thick layers of perfectly crystalline AlGaAs of one composition on top of another with a different composition without the formation of defects or undesired structures. Creating slab waveguide structures requires mixing layers of different compositions, and thus AlGaAs is a natural platform for make such waveguides. GaAs/AlGaAs also benefits from having mature fabrication processes.

As a nonlinear optical material, AlGaAs is a good candidate for creating practical devices. Previous studies have shown that bulk AlGaAs exhibits a Kerr effect that is over 500-times stronger than in silica [20]. The bandgap of Al_xGa_{1-x}As varies between 1.43 eV (870 nm) and 2.17 eV (570 nm). Thus, the half-bandgap can be placed near the 1310 nm and 1550 nm spectral windows, bringing large third-order nonlinear effects which lie near the resonance point. In the most recent studies of AlGaAs, focus has been placed specifically on Al_{0.18}Ga_{0.82}As since its bandgap is ~1.645 eV which places its half-bandgap near 1500 nm. This AlGaAs composition has been used in a variety of devices including discrete soliton waveguide arrays [5], nonlinear directional couplers [21], and nonlinear Bragg gratings [22].

1.4 Superlattice and Quantum Well Intermixing

Quantum-confined structures in semiconductors offer several advantages over devices made of bulk material. First, the density of carrier states is reduced yielding narrow spectral features. This is beneficial for creating lasers with narrow linewidths, which is necessary in DWDM systems. Second, the energy of confined states are

sensitive to both the material composition and the dimensions of the well and barrier regions. Thus, the wavelength of the emission/absorption peaks can be tailored to suite the required application. Several well and barrier regions can be integrated into the same structure to create a multiple-quantum well structure (MQW). Lasers benefit from MQWs since the cross-section of the active layer increases yielding more gain. In the case of passive waveguides, the increased cross-section exposes more of the guided optical energy to the quantum wells and its specific optical properties. MQWs also introduce spatial asymmetry to the waveguide structure, and as a result, the optical properties can become highly polarization dependent.

Semiconductor superlattices are extensions of MQW structures. As shown in Figure 1.2, superlattice is made up of a periodic stack of alternating material layers one of which is the barrier material and the other which is the well material. However, unlike MQWs, the barrier layers are narrow enough that carriers can quantum mechanically tunnel from one well to another. As a result, the normally discrete energy states of the quantum wells broaden out to form minibands that span across the entire superlattice [23]. The resulting band structure of the superlattice as a whole, depicted in Figure 1.3, is similar to bulk semiconductors. However, there is less band overlap, which results in the formation of energy gaps between the minibands. The energy gaps between the minibands can be controlled by changing the well and barrier thicknesses, thus allowing the same degree of freedom to engineer the electronic resonances as with simple quantum

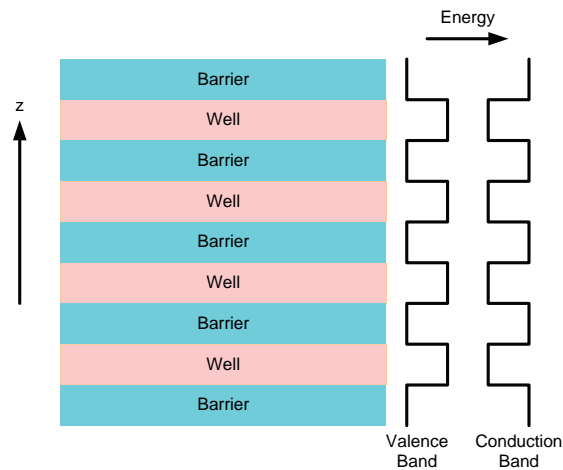


Figure 1.2: Layer stack of a compositional superlattice. A periodic set of coupled quantum wells form as shown on the right.

wells. As with bulk semiconductors, there is a set of valence bands and a set of conduction bands separated by a fundamental bandgap. Lasers in the visible [24] and infrared [25] have been fabricated in superlattices using the electron transition across the fundamental bandgap. It is also possible to obtain photon emission between conduction minibands as demonstrated in superlattice quantum cascade lasers emitting in the far infrared [26] and terahertz frequency range [27]. Thus, the unique and flexible band structure of superlattice has proved useful for several purposes.

One of the consequences of using heterostructures such as MQWs and superlattices is that translational symmetry found in bulk semiconductors is broken [28]. Superlattices lack symmetry between the directions that are in-plane of the layers (x and y) and the direction that is perpendicular to the layers (z). As a result, the electric susceptibility tensor has additional elements that are not found in bulk material. In the case of the third-order nonlinear susceptibility $\chi^{(3)}$, bulk III-V semiconductors have four independent, non-zero tensor elements. In symmetric superlattices, the degeneracy in the bulk coefficients breaks down resulting seven new independent elements for a total of eleven. This leads to polarization dependencies in the third-order nonlinear properties of superlattice that are not found in or that are weak in bulk semiconductors.

Another source of polarization dependence in the optical properties of superlattices is the lifted degeneracy between the light- and heavy-hole valence bands. As a result, the bandgap between the conduction band to the heavy-hole band differs from

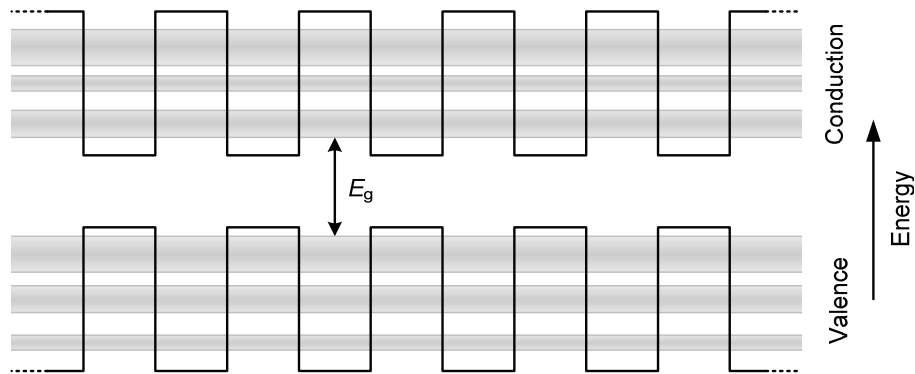


Figure 1.3: Electronic band structure of a superlattice. The solid black lines represent the conduction and valence band edges of the well and barrier materials. The grey areas represent the superlattice minibands formed due to strong coupling between quantum wells.

the bandgap involving the light-hole band. Since heavy-hole transitions are forbidden for light polarized perpendicular to the quantum well layers, the resonance points are found at different frequencies for each polarization [29]. Thus, the linear refractive index and nonlinear properties of the material depend on the polarization.

Another advantage of using quantum-wells and superlattices is the ability to change their electronic band structures by using quantum-well intermixing [30]. As shown in Figure 1.4, the intermixing process starts with the material undergoing a “disordering” process whereby defects and interstitials are created in the lattice. This can be achieved by a number of methods including impurity-free vacancy disordering (IFVD) [30] and ion-implantation [31]. Next, the disordered material is heated by rapid thermal annealing (RTA) facilitating an interdiffusion process which changes the composition at the material interfaces and repairs the crystal. The compositional change modifies the potential profile across the quantum well and shifts the energy bands of the entire superlattice. By shifting the bandgap of the superlattice, the linear and nonlinear properties of the material are changed as well. In most materials, intermixing causes the

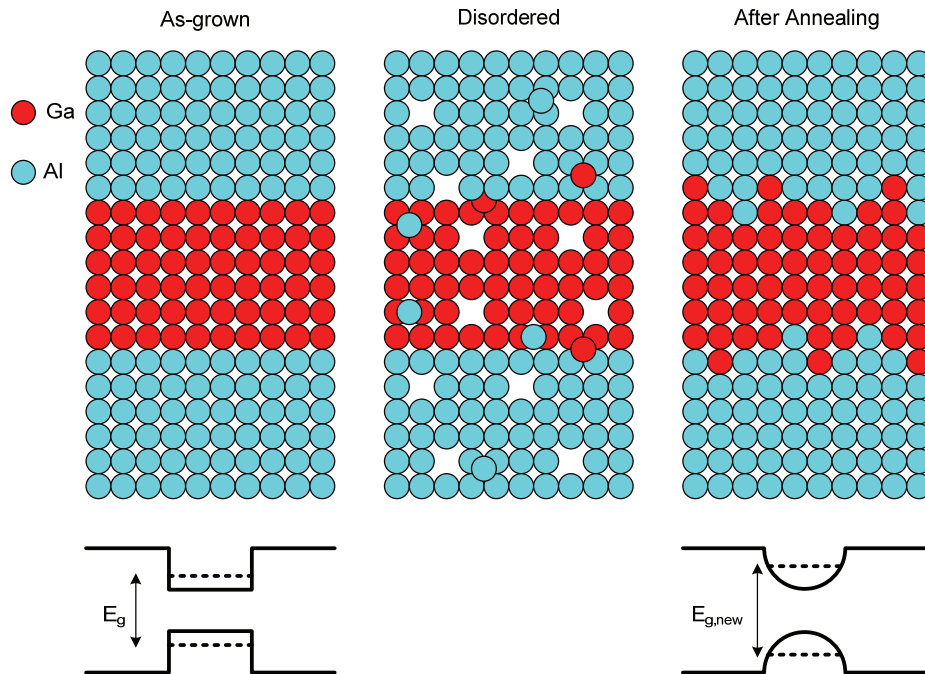


Figure 1.4: Quantum-well intermixing process. The material undergoes disordering which creates defects and interstitials. After annealing, interdiffusion causes the interfaces between the two materials (GaAs and AlAs) to smear resulting in an altered bandstructure and larger bandgap.

bandgap to increase and the nonlinear strength to decrease. Furthermore, the shift in the bandgap moves the two-photon absorption peak to shorter wavelengths and places the operating wavelengths of the device out of the material resonance. As a result, the nonlinear strength is decreased further. The amount of shift in the bandgap can be changed by varying the processing parameters. Also, intermixing can be applied to select areas of the chip while other areas are left unintermixing or with different degrees of intermixing, thus allowing the bandgap energy and nonlinearities to be patterned across the wafer. This enables a mixture of components to be integrated onto the same chip. It also allows for the creation of device structures not achievable in bulk materials.

The GaAs/Al_xGa_{1-x}As material system is of particular interest for creating superlattices. The half-bandgap of AlGaAs superlattices can be tuned over a wide range within the typical spectral ranges used in telecommunications systems. Thus, devices made in AlGaAs superlattice can benefit from the enhancement in the Kerr effect near the TPA resonance. Furthermore, with short period GaAs/AlGaAs superlattices, it is possible to “fully intermix” the superlattice with QWI. In this case, the amount of interdiffusion during annealing is high enough that the entire superlattice is mixed together. As a result, the superlattice becomes a bulk alloy of AlGaAs with a composition equivalent to the average amount of aluminum and gallium in the superlattice. Full intermixing yields the largest possible change in the bandgap of the superlattice and thus the largest modulation in the nonlinear coefficients.

The versatility of GaAs/AlGaAs superlattice allows it to be engineered to suit the desired application. Hutchings and Kleckner [32] attempted to find an optimized structure for quasi-phase matched (QPM) second-harmonic generation in the 1550 nm wavelength range. A symmetric superlattice of GaAs and AlAs was chosen to maximize the change in the alloy composition after intermixing. The width of the GaAs well layers was set to fourteen monolayers, placing the bandgap at 1.643 eV (~750 nm) and the half-bandgap at a wavelength of ~1500 nm. The AlAs barrier layer width was chosen to be fourteen monolayers where the modulation in $\chi^{(2)}$ after intermixing is maximized. This superlattice structure has been used in several QPM experiments to study the second-order nonlinear properties [33-35]. While the third-order nonlinear properties of this superlattice have been studied theoretically [28], they have yet to be measured. Such a study would be

required for creating photonic integrated circuits in superlattice with both second-order and third-order nonlinear devices.

1.5 Outline of Thesis

This thesis examines the linear and nonlinear properties of as-grown and intermixed 14:14 monolayer GaAs/AlAs superlattice-core waveguides. Chapter 2 covers measurements and calculations of the linear properties of superlattice including photoluminescence, linear index of refraction, confinement factor, waveguide dispersion, and linear loss. Accurate values for each of these linear properties are necessary to calculate the nonlinear coefficients. In Chapter 3, nonlinear absorption in superlattice waveguides is examined. This includes TPA in as-grown superlattice, and 3PA in intermixed superlattice. Again, it is necessary to obtain good values for the nonlinear absorption coefficients to evaluate other nonlinear properties. Chapter 4 examines nonlinear refraction in superlattice waveguides caused by the non-resonant optical Kerr effect below the half-bandgap. Specifically, this chapter examines self-phase modulation of a single linearly polarized waveguide mode, and cross-phase modulation between two orthogonally polarized modes. Chapter 5 looks into applications of superlattice to practical all-optical devices. In particular, figures of merit are discussed and design examples of nonlinear devices are presented.

Chapter 2

Linear Optical Properties of Superlattice Waveguides

2.1 Introduction

The design of any optical device requires good knowledge of the linear optical properties of the material and the waveguiding structures. This includes the linear index of refraction, the material absorption peaks, the dispersive properties, and the linear loss. For devices such as quasi-phase matched waveguides which use both as-grown and intermixed superlattice [34], the linear index is important for correctly determining the grating period, duty cycle, and second-harmonic conversion efficiency. Furthermore, it is necessary to accurately measure the linear properties of a waveguide in order to accurately determine the nonlinear behaviour of the device. For the specific superlattice structure studied in this thesis, low-temperature photoluminescence and the linear index of refraction of slab waveguides have already been examined by Kleckner [36]. Those properties are re-visited here in addition to several other linear properties that are required to quantify the nonlinear properties of superlattice.

This chapter examines the linear optical properties of superlattice waveguides. Measurements of room-temperature photoluminescence taken using a spatial scanning technique to isolate the superlattice layer from the rest of the structure are discussed. This method reveals details about the electronic bandstructure of the superlattice and verifies changes in the bandgap from quantum well intermixing. The linear index of refraction of

superlattice is calculated by using recent models for the index of bulk AlGaAs and by using a back-calculation method with measurements of the slab effective index. Spatial profiles of guided TE and TM modes of rib waveguides computed using a commercial mode solver are presented. From this, the amount of power confined to the superlattice core layer is found. The effective refractive index of the waveguides is calculated allowing further calculations of the birefringence, group velocity mismatch, and group velocity dispersion. Lastly, the results of linear loss measurements on both as-grown and intermixed waveguides carried out using the Fabry-Perot technique are discussed.

2.2 Wafer Structure

The structure of the superlattice wafer used is depicted in Figure 2.1. This same structure was used in Refs. [36, 37]. The core layer is a 0.6 μm -thick superlattice consisting of 75 repeating periods. Each period consists of 14 monolayers of GaAs as the quantum well material and 14 monolayers of AlAs as the barrier material for a total of 8 nm per period. Immediately on either side of the superlattice are 0.3 μm -thick buffer layers of bulk $\text{Al}_{0.56}\text{Ga}_{0.44}\text{As}$. These layers were included to improve end-fire coupling efficiency since the superlattice layer is too small to adequately collect light. Increasing

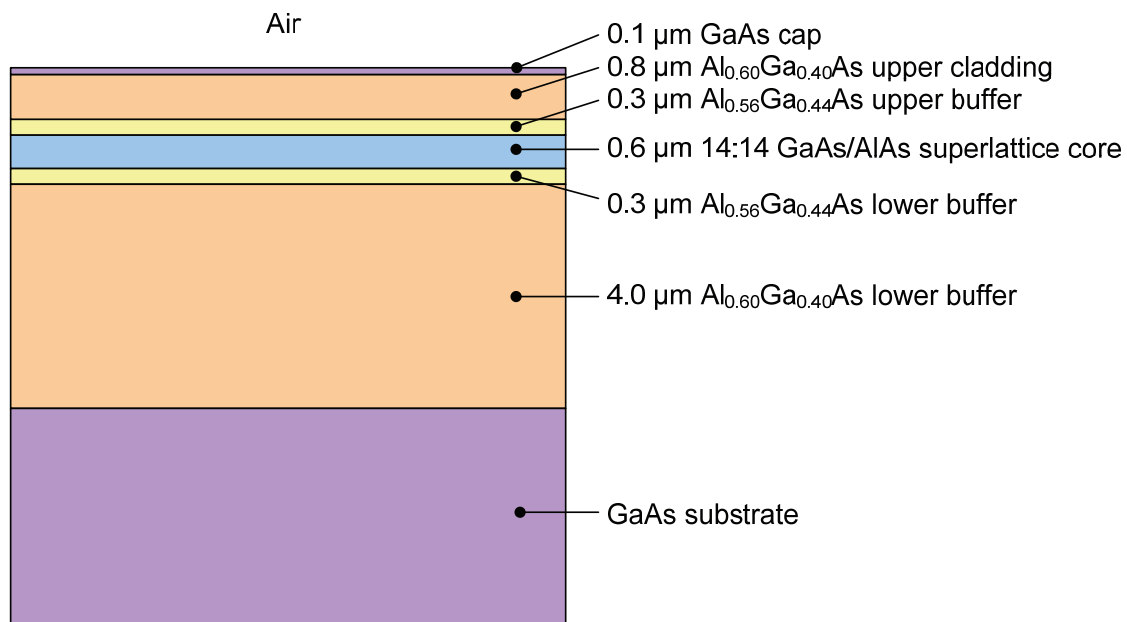


Figure 2.1: GaAs/AlAs superlattice wafer structure

the superlattice thickness would be problematic for growing the wafer by molecular-beam epitaxy (MBE) and would compromise the ability to fully intermix the superlattice. $\text{Al}_{0.56}\text{Ga}_{0.44}\text{As}$ was specifically chosen as the buffer layer since it has a larger bandgap and a smaller refractive index than $\text{Al}_{0.50}\text{Ga}_{0.50}\text{As}$, the average alloy of the superlattice that would form during complete intermixing. Thus, light would remain confined to the superlattice layer after intermixing. Cladding layers on either side of the buffer layers consist of $\text{Al}_{0.60}\text{Ga}_{0.40}\text{As}$ with the upper cladding being 0.8 μm thick and the lower cladding being 4.0 μm thick. A 0.1 μm -thick cap layer of GaAs was added to prevent oxidation of the AlGaAs cladding. All layers were grown nominally undoped by MBE on a semi-insulating GaAs substrate oriented along the [100] crystal direction.

Intermixed superlattice samples were fabricated using the sputtered silica-cap method [38]. A 50 nm layer of silica was sputtered onto the top surface of a wafer sample followed an additional 200 nm layer of silica deposited by plasma-enhanced chemical vapour deposition (PECVD). The sample then went under rapid thermal annealing (RTA) at a temperature of 850°C for 60 seconds. After annealing, the silica layers were removed with a wet etch in buffered hydrofluoric acid (HF) for 60 seconds.

2.3 Photoluminescence

Room temperature photoluminescence measurements were carried out on as-grown and intermixed superlattice using a Raman spectrometer. The excitation beam used was a Nd:YAG laser operating at a wavelength of 532 nm. Samples were oriented such that the excitation beam was incident on the cross-section of the layer structure. An electronically-controlled motion stage was used to move the sample under the beam to scan across the layers from the substrate to the cap layer. Re-emitted light was passed through polarization filters to isolate the TE and TM polarizations. At each scan point, the wavelength of the photoluminescence peaks were identified using a fit to Gaussian curves.

The results for as-grown superlattice are shown in Figure 2.2 for the TE and TM polarizations. These graphs show traces of the peak wavelength over the cross-section of the sample. The superlattice is located at the dip in the graphs between 1.5 and 2.5 μm .

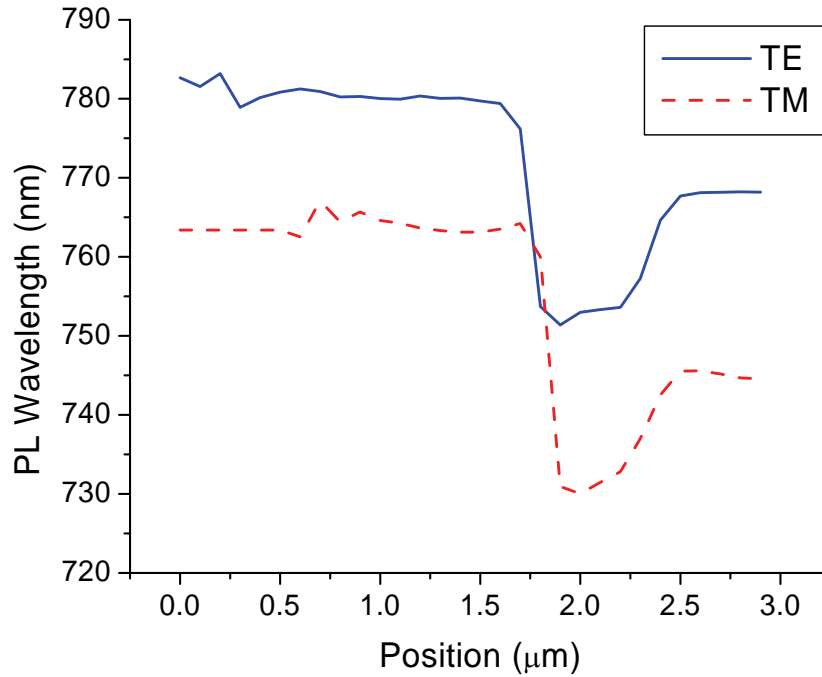


Figure 2.2: Traces of the photoluminescence peak across the as-grown superlattice wafer cross-section for the TE polarization and TM polarization. The top of the wafer is on the right side.

The width of the dip is roughly 600 nm, which agrees well with the designed thickness of the superlattice layer. For the TE polarization, the photoluminescence peak is located at 753 nm, which is close to the predicted bandgap wavelength of 750 nm. The TM polarization has a photoluminescence peak at 730 nm, which is 23 nm lower than in the TE polarization. This difference confirms the lifting of the degeneracy for the heavy-hole valence band in the superlattice.

The TE polarization results also show unexpected peaks of 780 nm and 767 nm above and below the superlattice layer respectively. The same phenomenon happens in the TM mode with peaks of 765 nm and 745 nm. These peaks do not correspond to either the $\text{Al}_{0.56}\text{Ga}_{0.44}\text{As}$ or $\text{Al}_{0.60}\text{Ga}_{0.40}\text{As}$ layers since their emission peaks should be found at wavelengths below 620 nm. Examination of the wafer structure indicates the presence of unidentified asymmetric single quantum wells (ASQW) formed at the top and bottom of the superlattice. As shown in Figure 2.3, AlAs and $\text{Al}_{0.56}\text{Ga}_{0.44}\text{As}$ form the barriers of a GaAs quantum well. Calculations of the quantum well energy levels were carried out using an algorithm developed by Street [39] and are detailed in Appendix A. The

bandgaps were computed as 787 nm for the heavy-hole transition and 756 nm for the light-hole transition, which agrees well with the photoluminescence data below the superlattice layer. By introducing an error of 10% into the GaAs well width, calculated bandgaps were 776 nm and 743 nm for the heavy-hole and light-hole transitions respectively. This agrees reasonably well with the PL peaks measured above the superlattice

Photoluminescence results from measurements of intermixed superlattice are shown in Figure 2.4. Both the TE and TM polarizations show a peak at 598 nm. This agrees with a theoretical prediction of 592 nm [28] and closely corresponds with the direct bandgap of $\text{Al}_{0.50}\text{Ga}_{0.50}\text{As}$. Furthermore, there is no longer any appreciable polarization dependence. This indicates that the superlattice has been fully intermixed. On the bottom side of the core layer are peaks occurring at around 640 nm and 635 nm for the TE and TM mode respectively. In this case, there is a small polarization dependence. This may be an indication that the bottom most layers of the superlattice were not completely intermixed.

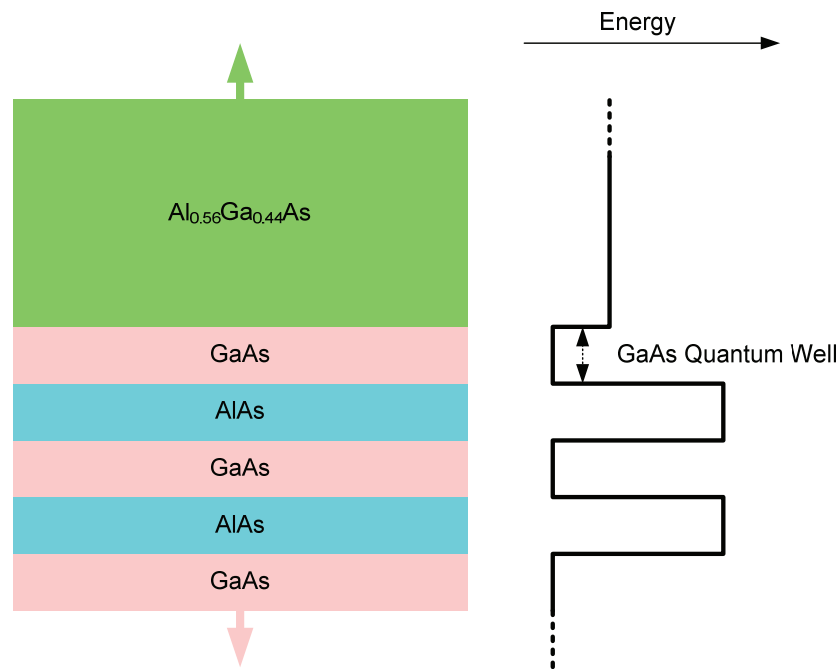


Figure 2.3: Unintended GaAs quantum well at ends of superlattice core layer.

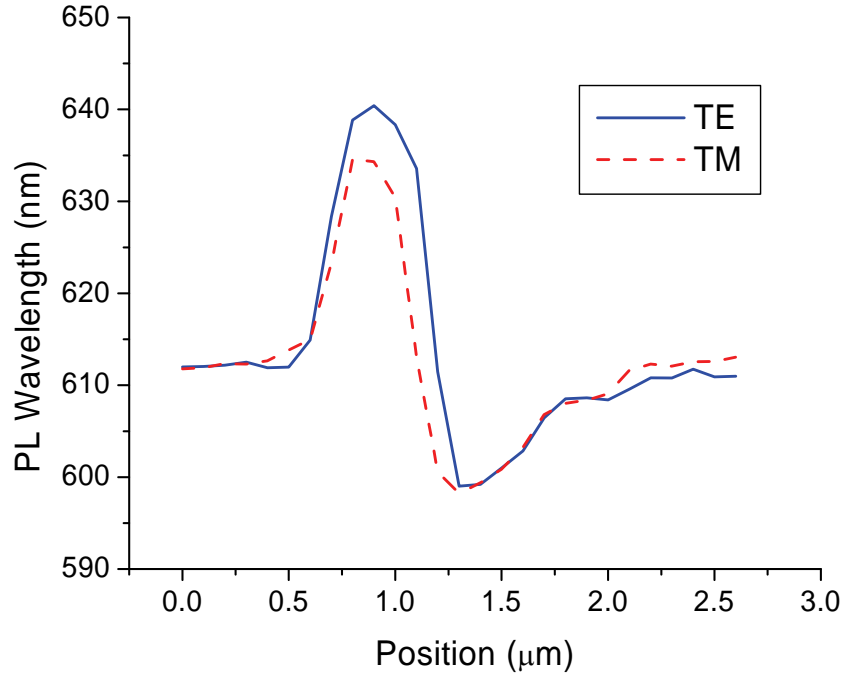


Figure 2.4: Traces of the photoluminescence peak across the intermixed superlattice wafer cross-section for the TE polarization and TM polarization. The top of the wafer is on the right side.

2.4 Linear Refractive Index

In order to calculate the mode profiles for rib waveguides, it is necessary to know values for the refractive index of the superlattice core layer. Highly accurate values are required to accurately determine the guided mode profiles. Early calculations found that a small error of less than 1% can cause variations of up to 10% in the confinement factor and mode effective areas. Such large variations will directly affect the values of the nonlinear absorption and nonlinear refraction coefficients determined from measured data. In this section, models of the refractive index for a heterostructure are used with several different models of the refractive index in bulk AlGaAs to predict the value of the refractive index for superlattice across the spectrum between 1400 nm and 1700 nm. Measured values of the slab effective index for the particular waveguide structure studied in this work are used to back-calculate the index of the superlattice core layer. Both as-grown and intermixed materials are studied with the latter being approximated as a bulk material of the average alloy.

2.4.1 Refractive Index Models for As-grown Superlattice

In previous work by Kleckner [37], theoretical refractive index values for GaAs/AlAs superlattice were predicted using the form birefringence model [40]. Index values for the GaAs and AlAs layers were derived from models of Adachi [41] and Afromowitz [42]. As was shown, the theoretically predicted values failed to accurately match experimental measurements of the effective slab index. This reason for this is twofold. First, the Adachi and Afromowitz models are semi-empirical models based on refractive index data measured at wavelengths close to the material bandgaps of GaAs and AlAs. Thus, the index values calculated from these models are not as accurate for wavelengths near the half-bandgap. Second, the form birefringence model assumes that each of the material layers acts independently on the propagating optical field. However, the response of a semiconductor to an optical field is highly dependent on the electronic structure of the material. Since the strong coupling of the quantum wells modifies the electronic band structure of the superlattice as a whole, the assumption that the layers act independently is not entirely valid. While this model is not likely to predict the index of superlattice with high accuracy, it was shown to come close [37]. Thus, it is worthwhile to use the form birefringence model to at least obtain ballpark figures.

The form birefringence model has the advantage that it takes into account the boundary conditions on the electric field at the interfaces of the layers, which are different for each polarization. Thus, the model is capable of predicting polarization dependencies in the linear index. For the TE polarization, the index of refraction is calculated as [37]

$$n_{TE} = \sqrt{\frac{t_{\text{GaAs}} n_{\text{GaAs}}^2 + t_{\text{AlAs}} n_{\text{AlAs}}^2}{t_{\text{GaAs}} + t_{\text{AlAs}}}} \quad (2.1)$$

where t_{GaAs} is the thickness of the GaAs layer, t_{AlAs} is the thickness of the AlAs layer, n_{GaAs} is the refractive index for GaAs, and n_{AlAs} is the refractive index for AlAs. The index of refraction for the TM polarization is

$$n_{TM} = \sqrt{\frac{n_{\text{GaAs}}^2 n_{\text{AlAs}}^2 (t_{\text{GaAs}} + t_{\text{AlAs}})}{t_{\text{GaAs}} n_{\text{AlAs}}^2 + t_{\text{AlAs}} n_{\text{GaAs}}^2}}. \quad (2.2)$$

The refractive index values for the GaAs and AlAs layers were derived from the semi-empirical models of Deri and Emanuel [43] and Gehrsitz *et al.* [44]. These models improve upon the models of Adachi and Afromowitz by specifically focusing on empirical data in wavelength ranges around 1550 nm. Figure 2.5 shows the predicted values of the superlattice index using the models of Adachi and Gehrsitz. The values yielded by the Deri and Gehrsitz model are virtually identical, and thus only the Gehrsitz model is shown. For both the TE and TM polarizations, the Gehrsitz model yields values lower than the Adachi model. Moreover, the amount of dispersion in the Gehrsitz curve is very different than the Adachi curve. The difference between the TE polarization index and the TM polarization index is around 0.038 for the Gehrsitz model and 0.043 for the Adachi model.

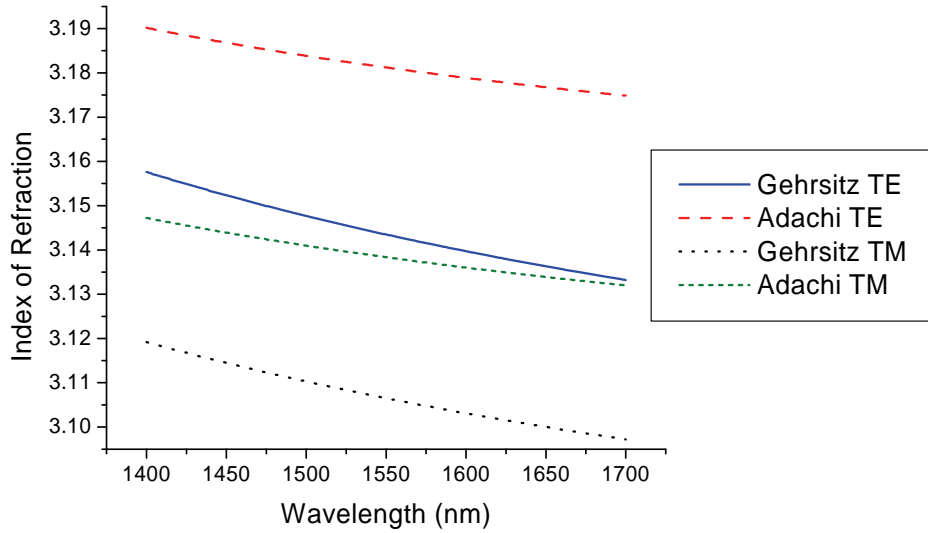


Figure 2.5: Predicted values of the refractive index of superlattice for the TE and TM polarizations based on the form birefringence model using the bulk AlGaAs index models of Gehrsitz and Adachi. Values produced by the Deri model are virtually identical to the values produced by the Gehrsitz model.

2.4.2 Back-calculation of Measured Index

Original measurements of the effective refractive index for the slab waveguide structure using the grating coupler technique were reported by Kleckner *et al.* [36]. Given known values of refractive index for the other layers in the slab waveguides, the refractive index for the core layer can be found by performing a back-calculation. Lumerical's MODE Solutions mode solver software was used in one-dimensional mode with the slab waveguide structure. Values for the effective slab index between 1400 nm and 1700 nm were calculated from a quadratic regression of the measured values [37]. The index of the core layer was varied in a trial-and-error algorithm until the calculated effective index from the mode solver matched the measured effective index.

The indexes of buffer and cladding layers were calculated from the Gehrsitz model, Adachi model, and the Deri model. Preliminary results showed that use of the Adachi and Deri models led to convergence failures in the algorithm. This took place because these models predict values for $\text{Al}_{0.56}\text{Ga}_{0.44}\text{As}$ and $\text{Al}_{0.60}\text{Ga}_{0.40}\text{As}$ that are larger than the measured effective index. This does not match experiments in which light was guided in the superlattice slab layer. For the Adachi model, the inaccuracy at wavelengths near 1550 nm is the likely source of the problem. Failure of the Deri model is likely due to interpolation that it uses to predict the bandgap for aluminum mole ratios greater than 0.45. In contrast, the Gehrsitz model is based on empirical data at wavelengths near 1550 nm and uses numerical fits to measured data for mole ratios greater than 0.45. As a result, it yields accurate values for the refractive index of the AlGaAs layers that are smaller than the slab effective index. Using the Gehrsitz model allowed the back-calculation algorithm to converge to reasonable values for the superlattice index. Thus, the Adachi and Deri models were not used in favour of the Gehrsitz model.

Figure 2.6 shows back-calculated refractive index of as-grown superlattice for TE and TM polarizations along with predicted values. Error bars of 0.001 are derived from the original error in the measured slab effective index [37]. The polarization dependence is large with the difference between the index of refraction for the TE and TM polarizations being about 0.03 for wavelengths between 1400 nm and 1700 nm. In both polarizations, the Gehrsitz model comes closer to the measured values than does the Adachi model. However, the difference between the measured values and the Gehrsitz

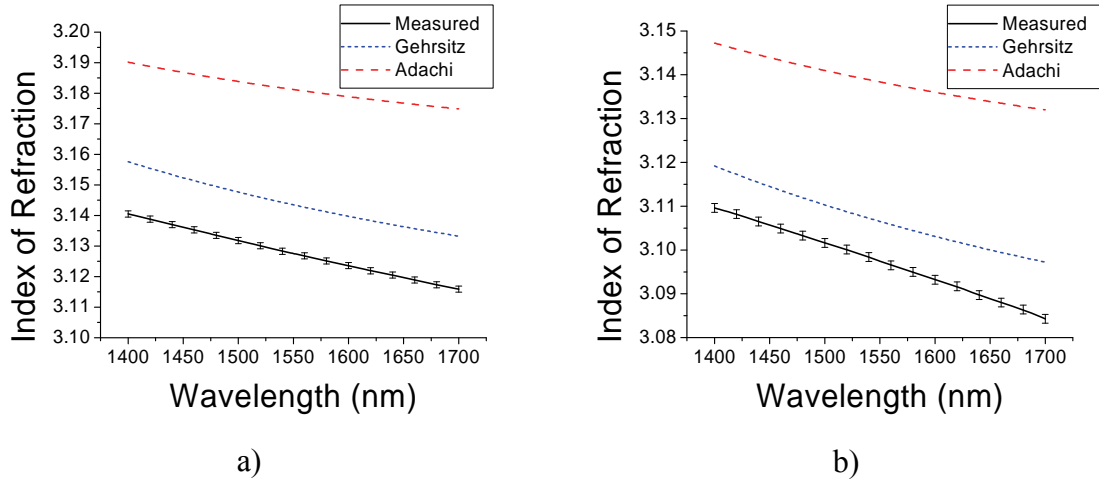


Figure 2.6: Back-calculated values of the measured refractive index of as-grown superlattice for a) TE and b) TM modes. Also shown are predicted values using the Gehrsitz and Adachi models.

model is nearly 0.02, which is large enough to significantly affect the mode profile and the location of the cutoff wavelength. Thus, neither of the theoretical models is accurate enough to reliably calculate the mode profiles for a rib waveguide. For subsequent mode solution calculations, the measured values for the index of refraction are used.

Back calculated values of the refractive index for intermixed superlattice are shown in Figure 2.7. Values for $\text{Al}_{0.50}\text{Ga}_{0.50}\text{As}$ calculated from the Gehrsitz model are provided for comparison. For the TE mode, the difference between measured index and the index for $\text{Al}_{0.50}\text{Ga}_{0.50}\text{As}$ is 0.01 at most. The difference between the TM mode and $\text{Al}_{0.50}\text{Ga}_{0.50}\text{As}$ is considerably larger at around 0.02. As with non-intermixed superlattice, the difference between the measured and theoretical values is too large to accurately calculate the mode profiles. Birefringence in the measured index for intermixed superlattice is reduced to about 0.01 from about 0.03 for as-grown material. Thus, superlattice becomes less polarization dependent after intermixing. This indicates that the intermixed superlattice is nearly equivalent to bulk $\text{Al}_{0.50}\text{Ga}_{0.50}\text{As}$, the average alloy. Quadratic regression coefficients of the back-calculated refractive index are listed in Table 2.1.

Table 2.1: Coefficients for quadratic regression for the index of refraction for TE and TM polarizations in as-grown and intermixed material. The form of the regression is $n = A\lambda^2 + B\lambda + C$ where λ is the wavelength (m).

	<i>A</i>	<i>B</i>	<i>C</i>
As-grown TE	3.1475×10^{10}	-1.8012×10^5	3.3312
As-grown TM	-2.0801×10^{10}	-1.9374×10^4	3.1776
Intermixed TE	8.6600×10^{10}	-3.6788×10^5	3.4709
Intermixed TM	-2.0420×10^{11}	5.4389×10^5	2.7489

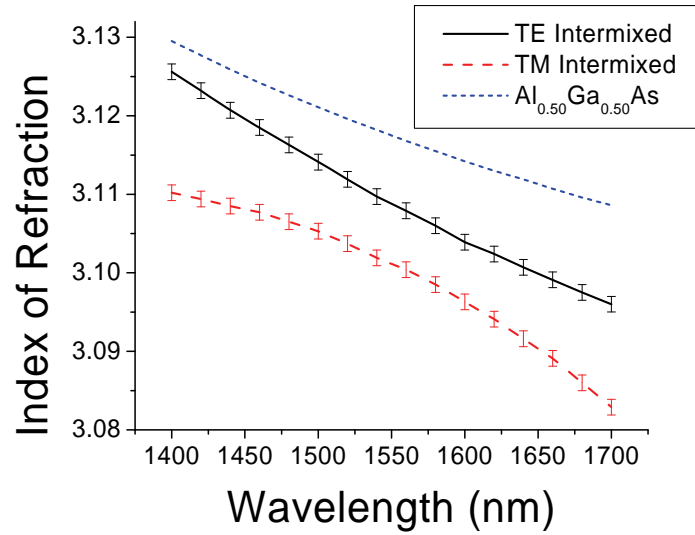


Figure 2.7: Back-calculated index of refraction values for intermixed superlattice. Also shown are index values for $\text{Al}_{0.50}\text{Ga}_{0.50}\text{As}$ calculated from the Gehrsitz model

2.5 Waveguide Properties

2.5.1 Sample Fabrication

Rib waveguides were fabricated in the wafer structure detailed in Section 2.2 for as-grown and intermixed superlattice. A 200 nm layer of silica was deposited onto the wafer samples by PECVD as hard mask layer. PMMA resist was spun onto the samples at 5000 rpm for 60 seconds. Several 3 μm -wide waveguides were directly written by electron-beam lithography (EBL). Development of the pattern took place in a 2.5:1 mixture of methyl isobutyl ketone:propanol (MIBK:IPA) over a duration of 45 seconds.

The pattern was transferred to the silica hard mask by reactive-ion etching (RIE) using a CHF_3 chemistry. The remaining resist was removed with an O_2 plasma. The GaAs and AlGaAs layers were etched to a depth of $0.8\ \mu\text{m}$ by RIE using a SiCl_4 chemistry. The silica hard mask was removed with a buffered HF wet etch. Finished waveguides are depicted in Figure 2.8. Photographs of the as-grown and intermixed samples are shown in Figure 2.9. A large amount of surface roughness is visible for the intermixed sample, while the non-intermixed sample had a relatively smooth surface. The increased roughness of the intermixed waveguides is thought to be the result of the intermixing process which produced damage to the surface.

2.5.2 Mode Profiles and Confinement Factor

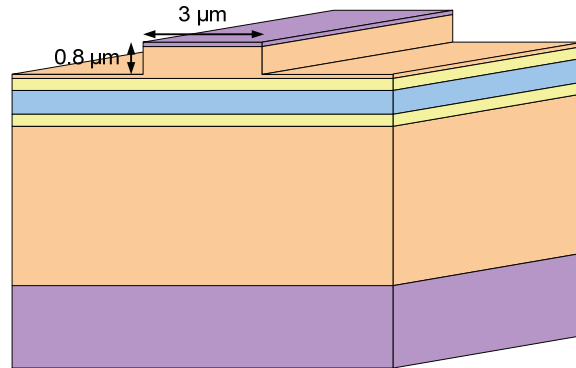


Figure 2.8: Superlattice rib waveguide structure

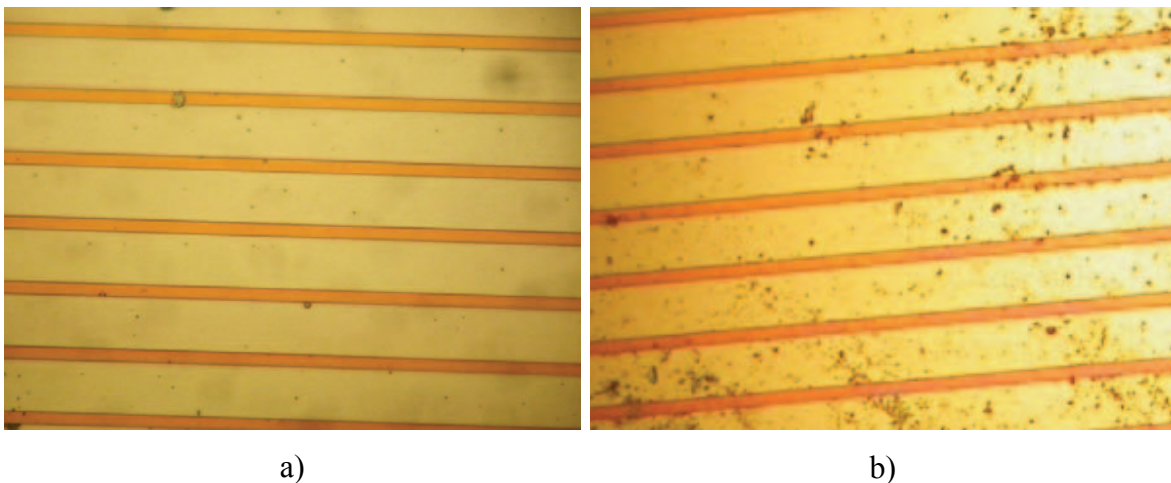
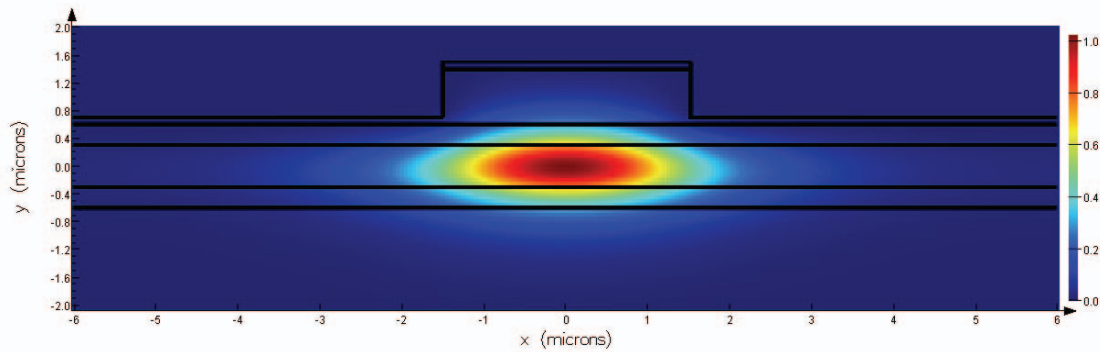
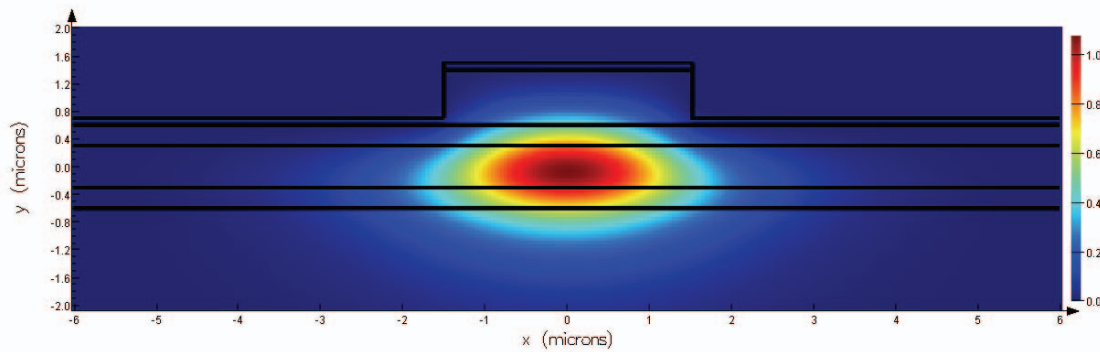


Figure 2.9: Photographs of a) as-grown and b) intermixed superlattice waveguides taken under a microscope at 500x magnification.

The spatial profiles of guided modes and effective waveguide indexes were determined using Lumerical MODE Solutions software. Refractive indexes of the bulk AlGaAs layers were derived from the Gehrsitz model. Back-calculated values of the superlattice from Section 2.4.2 were used for the core layer. Different refractive indexes were used in the solutions of the TE and TM mode. The mode solver was set in two-dimensional mode with a mesh of 240×160 points over a simulation area of $12 \mu\text{m} \times 8 \mu\text{m}$ with metal boundaries. Figure 2.10 depicts the mode profile at 1550 nm for the fundamental TE and TM modes in as-grown superlattice. Mode profiles in the intermixed superlattice are similar. In all cases, no higher-order modes were found for either polarization. Thus the waveguides are single-mode for each polarization. At longer wavelengths of the studied range, both modes were found to increase in size. In the case of the TM polarization, the mode profile extended deep into the lower cladding at wavelengths greater than 1600 nm. This also implies that the amount of leakage loss to



a)



b)

Figure 2.10: Mode profiles of as-grown superlattice rib waveguides at 1550 nm for the a) TE mode and b) TM mode.

the substrate will be greater in the TM mode. Furthermore, this indicates that the TM mode is approaching its cutoff wavelength.

The relative amount of power confined to the superlattice core layer was calculated from the mode profiles. The confinement factor is defined as [45]

$$\Gamma = \frac{\iint_{core} |f(x,y)|^2 dx dy}{\iint_{-\infty-\infty}^{\infty\infty} |f(x,y)|^2 dx dy} \quad (2.3)$$

where $f(x,y)$ is the modal distribution which is related to the irradiance by $I(x,y) \sim |f(x,y)|^2$. The upper integral is taken only over the superlattice core region, and thus represents the amount of power propagating through the core. Figure 2.16 shows the dispersion of the confinement factor for the TE and TM modes. The error bars result from the uncertainty in the index of refraction for the superlattice core and in the etch depth of the waveguides. On average, only about 50% of the total power is confined to the core layer for the TE mode. Further investigation revealed that about 30% of the power is found in the buffer layers and the remaining 20% propagates in the cladding layers. Light is less

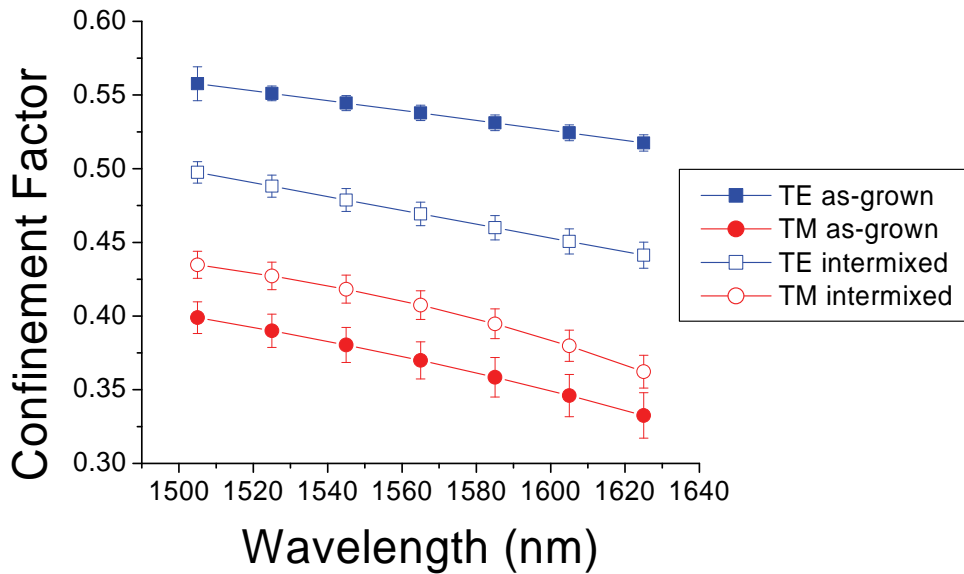


Figure 2.11: Rib waveguide confinement factor

confined in the TM mode which has confinement factors that are between 20-25% less than in the TE mode. The reduced confinement factor of the TM mode is due to a smaller index contrast of the superlattice core with the buffer and cladding layers. Light intensity in the core is significantly smaller for the TM mode, which will lead to reduced nonlinear effects.

2.5.3 Mode Effective Index and Group Velocity Dispersion

The mode solver was used to find the effective refractive index, of the guided TE and TM modes for the waveguide structure. Values of the effective index, n_{eff} , for as-grown and intermixed waveguides are shown in Figure 2.12. A small error of 0.001 results from the uncertainty in the index of the back-calculated superlattice refractive index. The lines are quadratic regressions of the form

$$n_{\text{eff}} = A\lambda^2 + B\lambda + C \quad (2.4)$$

where λ is the wavelength in meters and coefficients A , B , and C listed in Table 2.2. All of the curves show a similar trend except for the TM mode of the intermixed superlattice in which the curvature is opposite to the other curves. This implies that the group velocity dispersion is of the opposite sign for the intermixed TM mode.

Birefringence in the waveguides is defined as [46]

$$B_f = n_{\text{eff},TE} - n_{\text{eff},TM} \quad (2.5)$$

where $n_{\text{eff},TE}$ and $n_{\text{eff},TM}$ are the effective indexes of the TE mode and TM mode respectively. The spectral dependence of the birefringence for as-grown and intermixed waveguides is shown in Figure 2.13. As-grown waveguides have large birefringence values of ~ 0.015 on average. This is the result of the large polarization dependence of the

Table 2.2: Coefficients for quadratic regression for the waveguide effective index for TE and TM modes in as-grown and intermixed material. The form of the regression is $n_{\text{eff}} = A\lambda^2 + B\lambda + C$ where λ is the wavelength (m).

	<i>A</i>	<i>B</i>	<i>C</i>
As-grown TE	5.58×10^{10}	-2.69×10^5	3.37
As-grown TM	4.77×10^{10}	-2.33×10^5	3.32
Intermixed TE	9.10×10^{10}	-3.80×10^5	3.45
Intermixed TM	-2.13×10^{10}	-2.15×10^4	3.16

index of refraction of the superlattice. In contrast, birefringence in the intermixed

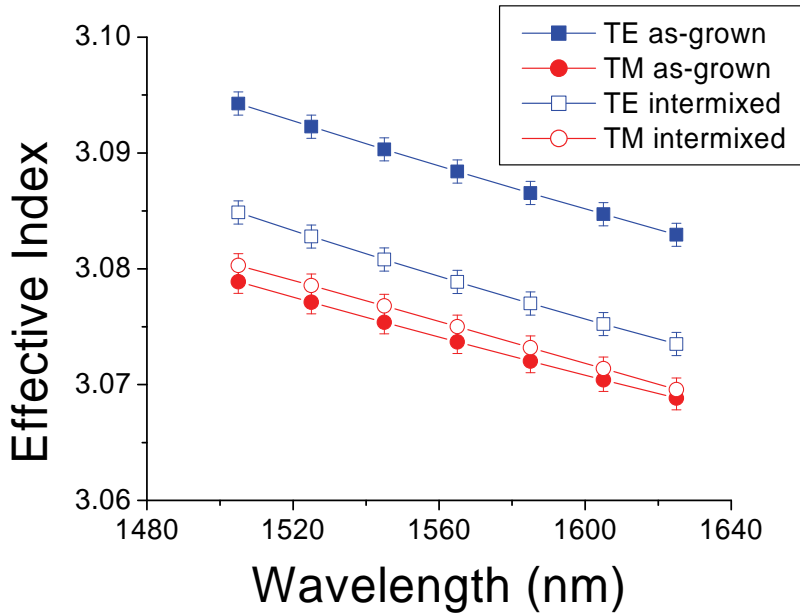


Figure 2.12: Effective index of refraction for 3.0 μm -wide rib waveguides

waveguides is small, owing to the reduced polarization dependence of the index of refraction in intermixed superlattice. The error bars are the result of the 0.001 error in the effective index values. Co-propagating TE and TM modes will go in- and out-of-phase with each other over the beat length which is defined as [3]

$$L_B = \frac{\lambda}{B}. \quad (2.6)$$

For as-grown superlattice, L_B was calculated to be $\sim 0.105 \pm 0.005$ mm across the studied spectrum. Intermixed superlattice had a larger beat length of $\sim 0.37 \pm 0.03$ mm.

Considering a 1 cm long waveguide, the beat length is much smaller than the propagation length for both as-grown and intermixed superlattice. This is important when considering nonlinear interactions between two co-propagating modes.

As a result of the birefringence, TE and TM modes will propagate with different speeds. The group velocity is defined as

$$v_g = \frac{1}{\beta_1} = \left(\frac{d\beta}{d\omega} \right)^{-1} \quad (2.7)$$

where β_1 is the first derivative of the propagation constant β for a guided mode, which is defined as

$$\beta = \frac{\omega}{c} n_{eff}(\omega). \quad (2.8)$$

Using Equation (2.4), the group velocity is calculated as

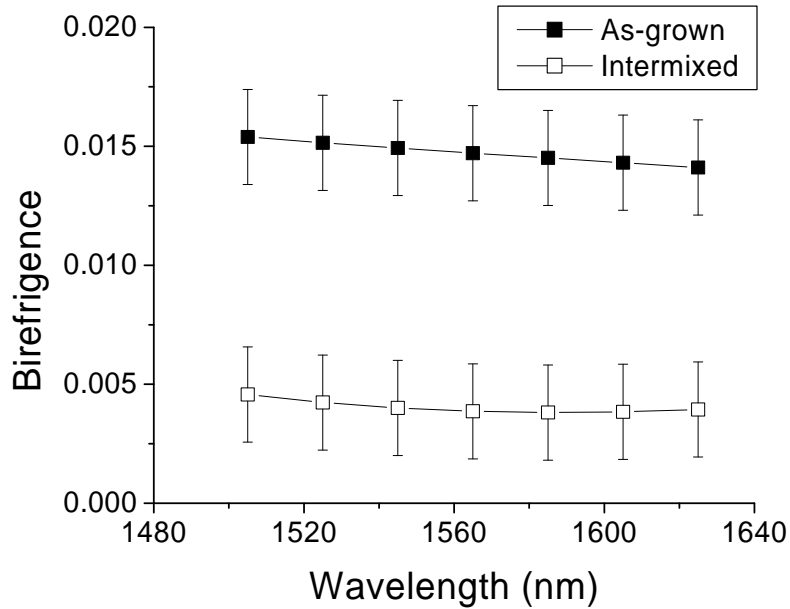


Figure 2.13: Linear birefringence for superlattice-core rib waveguides

$$v_g = \frac{c}{C - A\lambda^2} \text{ [m/s]} \quad (2.9)$$

where c is the speed of light. Figure 2.14 shows the spectral dependence of the group velocity mismatch $\Delta v_g = v_{g,TE} - v_{g,TM}$. The mismatch is large for as-grown waveguides as a result of the large birefringence. At 1545 nm, the difference in group velocity is about 88.3×10^3 m/s. For a mixed TE/TM mode input to a 1 cm-long waveguide, the TE component would lag the TM component by about 1 ps at the output. For optical pulses with durations on the order a few picoseconds, the group velocity dispersion will significantly affect the nonlinear interactions between the polarizations. In the case of the intermixed waveguides, the mismatch decreases rapidly and crosses through zero.

The group velocity dispersion is related to the second-order dispersion constant β_2 (also known as the GVD parameter) which is defined as

$$\beta_2 = \frac{d^2 \beta}{d\omega^2}. \quad (2.10)$$

Using Equations (2.4) and (2.8), the GVD parameter is calculated as

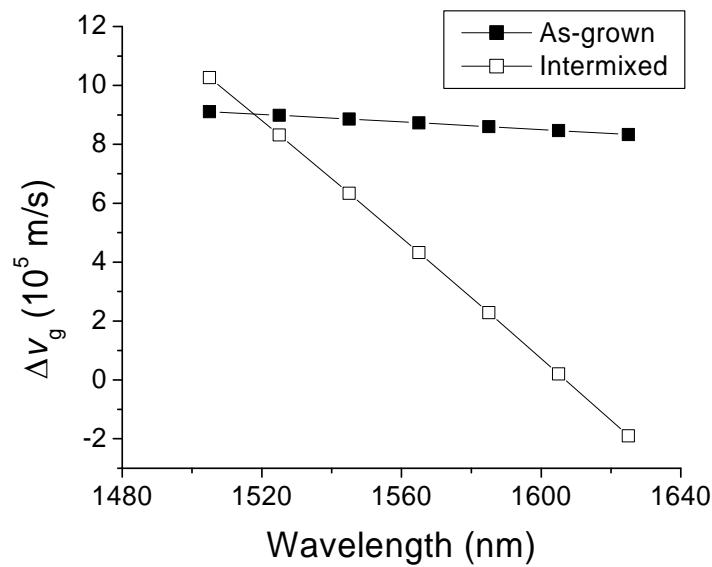


Figure 2.14: Group velocity mismatch between the TE and TM polarizations for rib waveguides

$$\beta_2 = A \frac{\lambda^3}{\pi c^2} [\text{s}^2/\text{m}]. \quad (2.11)$$

Values for β_2 are plotted in Figure 2.15 for the TE and TM modes. Across the spectrum, β_2 is on the order of $10^{24} \text{ s}^2/\text{m}$, which is on the same order of magnitude as values for bulk AlGaAs. For a Gaussian pulse, the change in the pulse length can be calculated as [3]

$$T_1 = T_0 \sqrt{1 + \left(\frac{z |\beta_2|}{T_0^2} \right)^2} \quad (2.12)$$

where T_0 is the original pulse length and z is the propagation distance. Using the GVD value in as-grown material for the TE mode at 1625 nm, where GVD is greatest, the change in a 1.5 ps long pulse after passing through a 1 cm long waveguide is less than 1%.

All values of the GVD are positive in sign except for the TM mode in intermixed waveguides. Further investigation showed that the small uncertainty in the effective index values can drastically change the coefficient A from the quadratic regression. It was found that it is possible to obtain a fit in which A is positive in value for intermixed waveguides in the TM mode. Thus, the apparent negative value of β_2 is likely the product

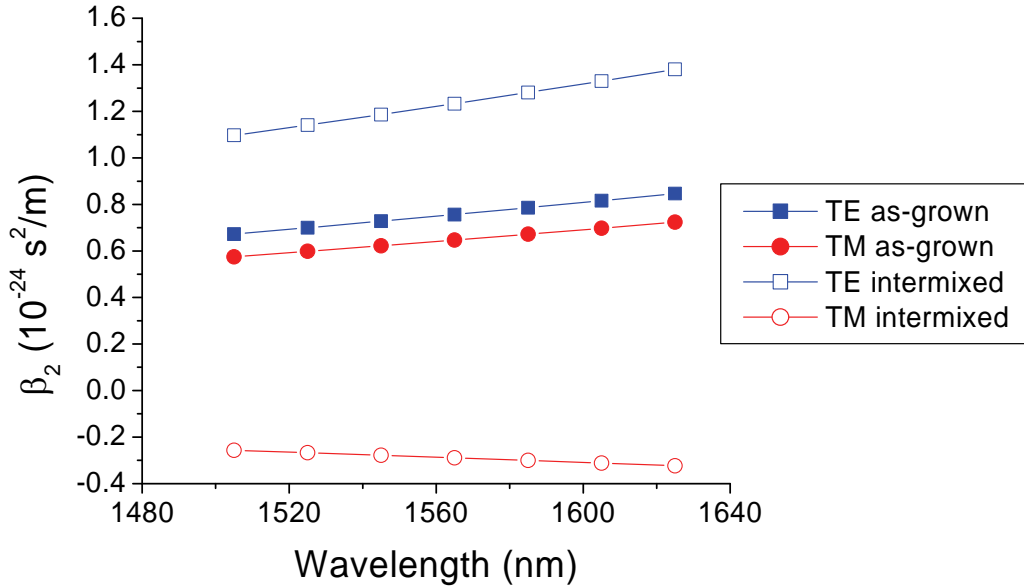


Figure 2.15: Group velocity dispersion for rib waveguides

of an imperfect curve fitting of the index data within the range of uncertainty. It is also noted that β_2 in this case is close enough to zero that it may indeed be positive. Furthermore, it is likely close in value to β_2 for the TE mode due to the reduced polarization dependence found in the other linear properties of intermixed superlattice. This conclusion is apparent from the original data for the slab effective index [37].

2.6 Linear Loss

The waveguides fabricated have linear losses associated with them that will reduce their effectiveness. Scattering losses occur because of imperfections in the material such as point defects, and from roughness on the surface and on the waveguide sidewalls. Leakage losses result from imperfect confinement of the mode to the waveguide core which leads to power being coupled to the substrate. Absorption losses are the result of carrier excitation by incident photons. Since the wavelengths which are considered in this study are at photon energies far below the bandgap, absorption losses will be small and the result of defects and impurities. Directional coupling is possible between adjacent waveguides and results in a loss in the waveguide under observation. However, the distance between waveguides is over 10 μm and thus directional coupling is minimal for sample lengths of about 1 cm. In this section, the linear losses of the as-grown and intermixed waveguides are measured using the Fabry-Perot method.

2.6.1 Experimental Methods

The Fabry-Perot technique is a simple method for determining the linear loss of a waveguide [47]. With sufficiently reflective end facets, a waveguide acts as a Fabry-Perot cavity with well defined resonator modes. The advantage of the Fabry-Perot technique is that it does not depend on the coupling efficiency at the front facet. Instead, it depends only on the effective index and length of the waveguide, both of which determine the resonator modes. Thus, it is only necessary to measure the transmission curve of the waveguide across a small spectral region around the wavelength of interest.

Linear loss coefficients, α_0 , for a Fabry-Perot cavity are calculated as [48]

$$\alpha_0 = -\frac{1}{L} \ln \left(\frac{1 - \sqrt{1 - K^2}}{RK} \right) \quad (2.13)$$

where L is the cavity length, R is the facet reflectivity, and K is the peak-to-peak transmission coefficient. With an incident light source that is perpendicular to the facet, the facet reflectivity is

$$R = \left(\frac{n_{eff} - 1}{n_{eff} + 1} \right)^2 \quad (2.14)$$

where n_{eff} is the effective index of the waveguide. The transmission coefficient is defined as

$$K = \frac{T_{max} - T_{min}}{T_{max} + T_{min}} \quad (2.15)$$

where T_{max} and T_{min} are the value of the maximum and minimum points of the Fabry-Perot transmission spectrum. The distance between maxima points is known as the free-spectral range and is calculated as

$$\Delta\lambda = \frac{\lambda^2}{2n_{eff}L} \quad (2.16)$$

The experimental setup for the Fabry-Perot technique is shown in Figure 2.16. A

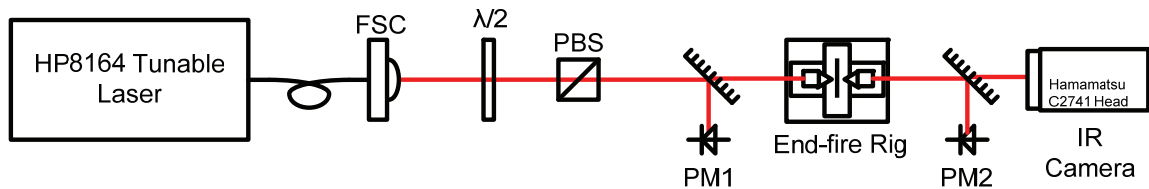


Figure 2.16: Experimental setup for Fabry-Perot loss measurement

continuous wave laser beam was generated from an HP8164 measurement system with an HP81642B tunable laser module having a 100kHz spectral linewidth. Light was guided from the tunable laser through a fibre to the free-space coupler (FSC). The polarization of the beam is set by the half-waveplate ($\lambda/2$) and the polarizing beam cube (PBS). Waveguide samples were mounted on an end-fire rig between a pair of 40 \times objective lenses. Output from the waveguides was focused onto the IR camera to aid in coupling light to one of the many waveguides on the sample. PM1 and PM2 measured the input and output power respectively. The tunable laser was set to scan in small steps over a small spectral range centered on a wavelength of interest, and the input and output powers were recorded at each step.

2.6.2 Results

As-grown and intermixed waveguide samples were 1.2 cm long and 0.5 cm long respectively. The tunable laser was set to scan in 0.01 nm steps for the as-grown sample and in 0.02 nm steps for the intermixed samples to give sufficient resolution within their free-spectral ranges. Figure 2.17 shows the transmission spectrum around 1545 nm for

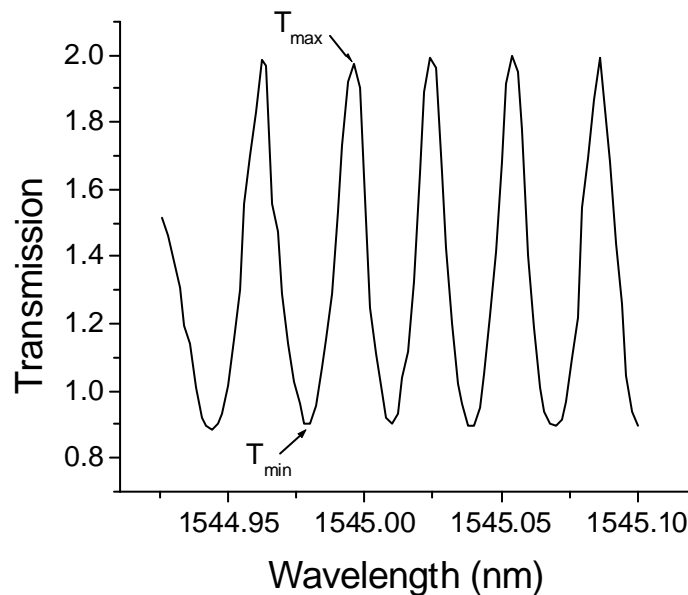


Figure 2.17: Fabry-Perot transmission spectrum around 1545 nm in the TE mode for as-grown superlattice.

the TE mode in the as-grown sample. Transmission spectra for the TM polarization and for the intermixed sample are similar. The minima and maxima points were averaged to give a mean value for K and thus a mean value for α_0 .

Linear loss coefficients for the as-grown superlattice for wavelengths between 1505 and 1640 nm are shown in Figure 2.18. The TM mode is more lossy than the TE mode, with losses being about 0.25 cm^{-1} for the TE mode and 0.70 cm^{-1} for the TM mode. This is likely due to the reduced confinement of the TM mode to the waveguide core. As a result, the light would be more susceptible to surface and sidewall roughness causing scattering. Also, leakage into the substrate may also be larger. The curve is relatively flat for the TE mode. However, the TM mode is flat only up to a wavelength of about 1565 nm. After this point, the loss increases rapidly and then flattens out just beyond 1605 nm. This indicates that the TM mode may be approaching its cutoff wavelength.

Measured loss values for intermixed waveguides are shown in Figure 2.19. Both polarizations are very lossy with α_0 values of $\sim 7.0 \text{ cm}^{-1}$. The large loss is likely due to a high density of defects that were formed during the intermixing process [49]. Trap states can result from these defects and absorb light at wavelengths at the wavelengths studied.

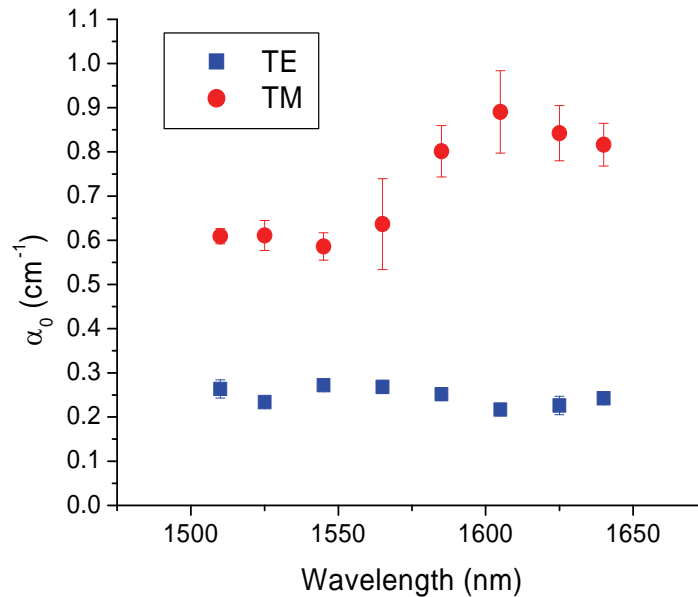


Figure 2.18: Spectral dependence of linear loss coefficients for 1.2 cm-long as-grown superlattice rib waveguides

Scattering from point defects in the lattice should not occur since they are much smaller than the wavelengths used. However, coalescence of these point defects would create imperfections large enough to result in significant scattering. From observations of the sample under a microscope, the surface of the sample was observed to be much rougher than in the as-grown samples. As a result, the scattering loss in the waveguides would be significantly higher than the as-grown sample. The TM mode has consistently higher loss than the TE mode, but the difference is not as great as in the as-grown waveguides. This is the result of the similarity in the confinement factors for the TE and TM modes in intermixed waveguides.

The uncertainty in the measured results is mostly due to variation in the value of K from one maxima/minima pair to the next in the transmission spectrum. The error in K was about 16% in one case, and less than 10% in all others, while the error in the effective index is less than 0.1% and thus it can be ignored. The measured lengths of the samples are accurate to about 0.02 cm, thus the error in the 0.5 cm intermixed sample is 2.5% while the error in the 1.2 cm as-grown sample is less than 1%.

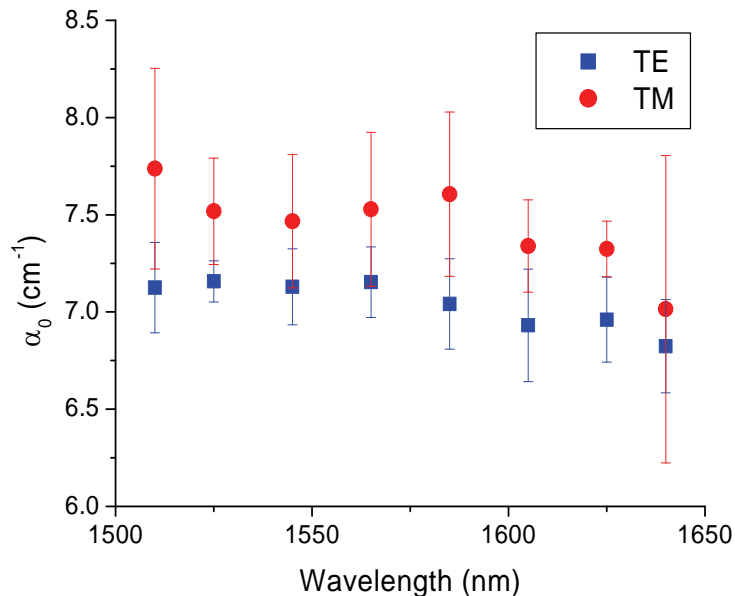


Figure 2.19: Spectral dependence of linear loss coefficients for 0.5 cm-long intermixed superlattice rib waveguides

2.7 Conclusions

In this chapter, the linear properties of as-grown and intermixed superlattice have been studied. Photoluminescence experiments exhibited the expected polarization dependence in the re-emitted light for as-grown superlattice. This indicates that heavy-hole valance band degeneracy has been lifted. Intermixed samples show photoluminescence shift of ~ 150 nm in the TE polarization and reduced polarization dependence that indicates complete intermixing. Values of the index of refraction in as-grown and intermixed superlattice were back-calculated from measurements of the slab effective index. Theoretical models of the refractive index for superlattice were not able to make adequate predictions despite the use of improved models of bulk AlGaAs from Gehrsitz and Deri. Thus, it was necessary to use measured index for all subsequent calculations and experiments on the linear properties of superlattice.

Superlattice waveguides were studied for mode confinement, dispersion, and linear loss. Mode profiles calculated showed the TE mode is more confined to the superlattice layer than the TM mode. This is due to reduced index contrast between the core and cladding layers for the TM mode. Birefringence is high and results in a large group velocity mismatch between the TE and TM polarizations. GVD is on the same order as bulk AlGaAs and is significant enough to affect the nonlinear behaviour. The linear loss is low for as-grown superlattice and shows significant polarization dependence. Intermixed waveguides are much more lossy, which is likely due to an increase in the number of defects and surface roughness. The polarization dependencies of the mode confinement and loss will greatly affect the nonlinear behaviour of the waveguides.

Chapter 3

Nonlinear Absorption in As-Grown and Intermixed Superlattice

3.1 Introduction

Nonlinear multiphoton absorption in a material can have both useful and detrimental effects. In the case of the Kerr effect, nonlinear absorption reduces the amount of power available for causing phase shifts and refractive index changes. This decreases the effective Kerr coefficient of the material. To properly characterize the actual Kerr coefficient and to later design practical devices based on nonlinear refraction, it is necessary to measure the strength of nonlinear absorption in the waveguiding structures used.

The dominant nonlinear loss mechanism depends greatly on the electronic structure of the material and the spectral range of interest. In this study, the interest is in wavelengths near the 1550 nm telecommunications band. The half-bandgap of as-grown 14:14 GaAs/AlAs superlattice lies near 1500 nm, and thus the dominant nonlinear loss mechanism will be two-photon absorption. In the case of intermixed superlattice, the half-bandgap was determined to be around 1200 nm. Since 1550 nm is far below the half-bandgap of intermixed superlattice, the dominant nonlinear loss mechanism will be three-photon absorption.

This chapter discusses nonlinear absorption in as-grown and intermixed superlattice waveguides. TPA measured in as-grown superlattice-core using the inverse

transmission method and picosecond pulses is examined. A study of 3PA measured in intermixed superlattice-core waveguides using the inverse transmission squared technique and femtosecond pulses is presented. The spectrum of light emitted from the recombination of carriers excited by nonlinear absorption is also examined.

3.2 Two-photon Absorption in As-grown Superlattice

3.2.1 Theory

Two-photon absorption is a process in which a valence band electron absorbs two photons and transitions to the conduction band. As illustrated with simplified band structure in Figure 3.1, this electron transition can be either direct or indirect [51]. Absorption of the first photon is modeled as a transition to a virtual energy level at the midgap. The second photon completes the transition to the points near the conduction band minima. In the case of indirect transitions, phonon assistance is required. Since this is a low probability event, indirect TPA is much less efficient than direct TPA for similar bandgaps. Transitions can occur from either the heavy-hole (HH) or light-hole (LH) bands.

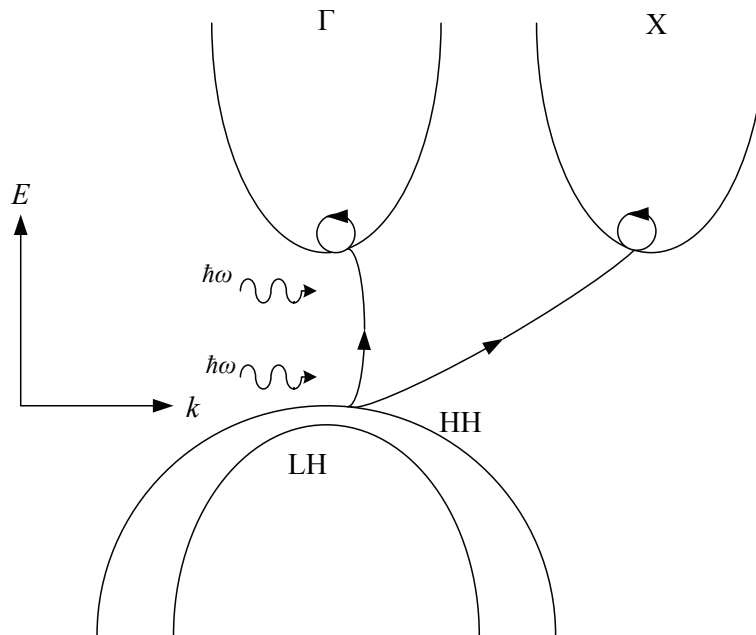


Figure 3.1: Band structure of a typical semiconductor showing direct and indirect electron transitions by TPA. Reproduced from [50].

valence bands. In the case that the valence band minima do not occur at the same energy, there will be different energy gaps and thus multiple TPA resonances. Since transitions from the heavy-hole band are forbidden with TM polarized light and thus the TPA peak for the TM mode occurs at a different wavelength than for the TE mode. In either case, TPA should only occur for photon energies above the half-bandgap points for each polarization. However, band tail states that have lower energies than the bandgap can cause a significant amount of TPA just below the half-bandgap [20].

TPA causes an increase in the absorption that is proportional to the intensity of the optical field. From Equation (1.3), the change in the loss coefficient is

$$\Delta\alpha = \alpha_2 I \quad (3.1)$$

where α_2 is the TPA coefficient and I is the intensity. At high input powers, the transmission through a waveguide will simultaneously be affected by both linear losses and TPA. The intensity is a function of the distance, z , and can be expressed as [52]

$$\frac{dI(z)}{dz} = -\alpha_0 I(z) - \alpha_2 I^2(z). \quad (3.2)$$

Accounting for the coupling efficiency, η , and the reflectivity of the waveguide facet, R , Equation (3.2) can be solved for a propagation distance L to yield the inverse of the transmission [53]

$$\frac{1}{T} = \frac{I_{in}}{I_{out}} = \frac{1}{(1-R)^2 \eta e^{-\alpha_0 L}} + \alpha_2 \frac{1 - e^{-\alpha_0 L}}{\alpha_0 (1-R) e^{-\alpha_0 L}} I_{in} \quad (3.3)$$

where I_{in} and I_{out} are the input and output intensities respectively. By measuring the transmission of a beam through a medium versus the input intensity, the value of α_2 can be calculated from the slope of the inverse transmission curve, m , according to [48]

$$\alpha_2 = m \frac{\alpha_0 (1 - R) e^{-\alpha_0 L}}{1 - e^{-\alpha_0 L}}. \quad (3.4)$$

This technique is known as the inverse transmission method.

In a waveguide structure, the intensity is not uniform across the mode profile and it is necessary to account for this when calculating the TPA coefficient. For a weakly-guiding structure, it can be assumed that the transverse mode profile does not significantly change over the propagation distance in the presence of nonlinear absorption. Using the formalism of Grant [45], the effective $\Delta\alpha$ for a waveguide can be expressed as

$$\Delta\alpha_{eff} = \frac{\int_{-\infty}^{\infty} \int_{-\infty}^{\infty} \Delta\alpha(x, y) I(x, y) dx dy}{\int_{-\infty}^{\infty} \int_{-\infty}^{\infty} I(x, y) dx dy} \quad (3.5)$$

where the spatial dependence of both I and $\Delta\alpha$ are accounted for. A waveguide can be treated as though it has a uniform nonlinearity and thus $\Delta\alpha(x, y)$ is a constant. Using Equation (3.1) for $\Delta\alpha(x, y)$, Equation (3.5) simplifies into

$$\Delta\alpha_{eff} = \alpha_{2,eff} I_{eff}^{(3)} = \alpha_{2,eff} \frac{P}{A_{eff}^{(3)}} \quad (3.6)$$

where $\alpha_{2,eff}$ is the effective TPA coefficient for the waveguide, and $I_{eff}^{(3)}$ is the third-order nonlinear effective intensity. The optical power, P , is defined as

$$P = \int_{-\infty}^{\infty} \int_{-\infty}^{\infty} I(x, y) dx dy \quad (3.7)$$

and $A_{eff}^{(3)}$ is the third-order effective mode area which is expressed as

$$A_{eff}^{(3)} = \frac{\left[\int_{-\infty}^{\infty} \int_{-\infty}^{\infty} I(x, y) dx dy \right]^2}{\int_{-\infty}^{\infty} \int_{-\infty}^{\infty} I^2(x, y) dx dy} \quad (3.8)$$

$I_{eff}^{(3)}$ can be used in Equation (3.3) in place of I_{in} . However, this gives the effective TPA coefficient for the waveguide structure as a whole. In order to quantify the behaviour of the superlattice alone, it is necessary to isolate its contribution from the whole. In a multilayered waveguide structure employing different materials each with a different constant valued $\alpha_{2,(i)}$, Equation (3.5) must be expanded as

$$\Delta\alpha_{eff} = \frac{\alpha_{2,(1)} \iint_{(1)} I^2(x, y) dx dy + \alpha_{2,(2)} \iint_{(2)} I^2(x, y) dx dy + \dots}{\int_{-\infty}^{\infty} \int_{-\infty}^{\infty} I(x, y) dx dy} \quad (3.9)$$

where the integrals are taken over the boundaries of each material. This equation may be simplified and equated to Equation (3.6) giving

$$\Delta\alpha_{eff} = \alpha_{2,eff} \frac{P}{A_{eff}^{(3)}} = \alpha_{2,(1)} \frac{P}{A_{eff,(1)}^{(3)}} + \alpha_{2,(2)} \frac{P}{A_{eff,(2)}^{(3)}} + \dots \quad (3.10)$$

where

$$A_{eff,(i)}^{(3)} = \frac{\left[\int_{-\infty}^{\infty} \int_{-\infty}^{\infty} I(x, y) dx dy \right]^2}{\iint_{(i)} I^2(x, y) dx dy} \quad (3.11)$$

are the third-order effective areas for each material i . Thus, each material contributes to the nonlinear absorption in proportion to its TPA coefficient, and by the amount and

intensity of the mode overlap with that material. The TPA coefficient of the layer of interest can be solved for given known values of α_2 for the other layers.

3.2.2 Previous Studies of TPA in Semiconductors

Two-photon absorption has been measured in a variety of bulk semiconductors and quantum confined structures. Dinu *et al.* studied TPA in bulk silicon using the Z-scan technique at wavelengths above the half-bandgap [54]. TPA coefficients were measured as 0.79 cm/GW at 1540 nm and 0.74 cm/GW at 1270 nm. Two different compositions of bulk AlGaInAs were studied by Villeneuve *et al.* at wavelengths near 1550 nm [55]. The value of α_2 was measured to be 63 cm/GW the composition with the smaller bandgap and 20 cm/GW for the other. Zilkie measured TPA in AlGaInP MQW semiconductor optical amplifiers (SOA) [48]. At 1600 nm, the TE mode had a α_2 value of ~ 300 cm/GW and the TM mode had a α_2 of ~ 400 cm/GW. In all of these cases, the TPA coefficients were measured at wavelengths above the half-bandgap where TPA is expected to be strong.

Several studies have been carried out in AlGaAs-based materials at wavelengths below the half-bandgap. TPA was measured for bulk Al_{0.18}Ga_{0.82}As-core waveguides by Aitchison *et al.* using the inverse transmission method [20]. Near the half-bandgap of 1500 nm, the value of α_2 was ~ 1.0 cm/GW for the TE mode and ~ 0.2 cm/GW for the TM mode. This confirmed the anisotropy of TPA in zinc-blende semiconductors predicted by Hutchings and Wherrett [56]. The value of α_2 quickly decreased for both modes as the wavelength was increased beyond 1500 nm until reaching a value of nearly zero in the TM mode near 1540 nm.

Bulk AlGaAs and GaAs/AlGaAs MQW waveguides were studied by Islam *et al.* at wavelengths between 1650 nm and 1700 nm, which were below the half-bandgap [57]. For the bulk waveguides, Al_{0.20}Ga_{0.80}As was chosen for the core layer. The MQW waveguides had a core layer with 200 periods of 4.0 nm GaAs wells and 7.0 nm Al_{0.30}Ga_{0.70}As barriers. The half-bandgap of the MQW was measured at ~ 1600 nm while the half-bandgap of the bulk AlGaAs is calculated as ~ 1480 nm using the numerical fit of Adachi [41]. Measurements of the TPA coefficients for bulk AlGaAs using a pump-probe technique yielded a value of 0.026 cm/GW. MQW waveguides were measured using the

inverse transmission technique and showed a 2.4-times enhancement and large polarization dependence with TE modes and TM modes having average α_2 values of 0.65 cm/GW and 0.40 cm/GW respectively. The enhancement in MQWs was attributed to strengthened exciton interactions. The polarization dependence was attributed to the differing electron transition energies of TE and TM polarized light.

Another study of GaAs/AlGaAs MQW waveguides was carried out by Yang *et al.* [58]. The core layer consisted of 85 periods of 7.0 nm GaAs wells and 10 nm Al_{0.30}Ga_{0.70}As barriers. Measurements were carried out for wavelengths between 1500 nm and 1650 nm. As with other studies of MQW waveguides, the TPA strength showed an enhancement over bulk material and strong polarization dependencies. For shorter wavelengths, peaks in the TPA dispersion matched known exciton resonances for this structure. At their peak, α_2 was as large as 11.0 cm/GW for the TM mode at around 1550 nm and ~9.0 cm/GW for the TE mode at around 1500 nm.

3.2.3 Experimental Methods

Measurement of the nonlinear properties of superlattice waveguides requires an optical field of sufficient power to cause observable effects. For the experiments in this study, a pulsed laser system was used to achieve high peak powers with moderate average powers. The laser system shown in Figure 3.2 consisted of a mode-locked Ti:sapphire laser optically pumped by a frequency-doubled Nd:YVO₄ diode-pumped laser. Output pulses were between 2.5 and 1.5 ps and were emitted at a rate of 76.5 MHz with center wavelengths from 730 nm to 820 nm. The output of the Ti:sapphire laser was converted to wavelengths between 1450 nm and 1650 nm using a KTP-based singly-resonant optical parametric oscillator (OPO). Pulse widths were measured using an autocorrelator and the center wavelength of the pulses was measured using a spectrometer.

Superlattice waveguide samples were mounted onto an end-fire rig. A 40× laser diode objective lens with an antireflection coating for wavelengths near 1550 nm was used to couple light into the waveguides. On the output end, a 40× objective lens was used to image the output light onto several instruments. Newport 1830-C optical power

meters with 818-IR detectors measured the amount of input and output power. The spectrum of the output pulses was measured with an ANDO AQ6317B optical spectrum analyzer (OSA) using light guided to it through a multi-mode fiber. An infrared camera was used to find and couple light to the waveguides on the sample. An optical attenuator was made up of a polarizing beam cube and a half-waveplate mounted in computer-controlled rotation stage. A half-waveplate was placed before the input objective to set the polarization of the beam to either TE or TM.

Pulses from the laser system were modeled as Gaussian in shape. Given the average power of the laser P_{ave} , the repetition rate f , and the full-width at half maximum (FWHM) pulse width τ_{FWHM} , the peak pulse power can be calculated as [48]

$$P_0 = P_{ave} \frac{2\sqrt{\ln(2)}}{\tau_{FWHM} f \sqrt{\pi}}. \quad (3.12)$$

The maximum average power at the front facet of the waveguide sample was ~ 100 mW, which gives a maximum peak power of ~ 800 W.

The transmission through a single waveguide was measured as a function of input peak intensity. Figure 3.3 shows a plot of this the inverse transmission for the TE mode at

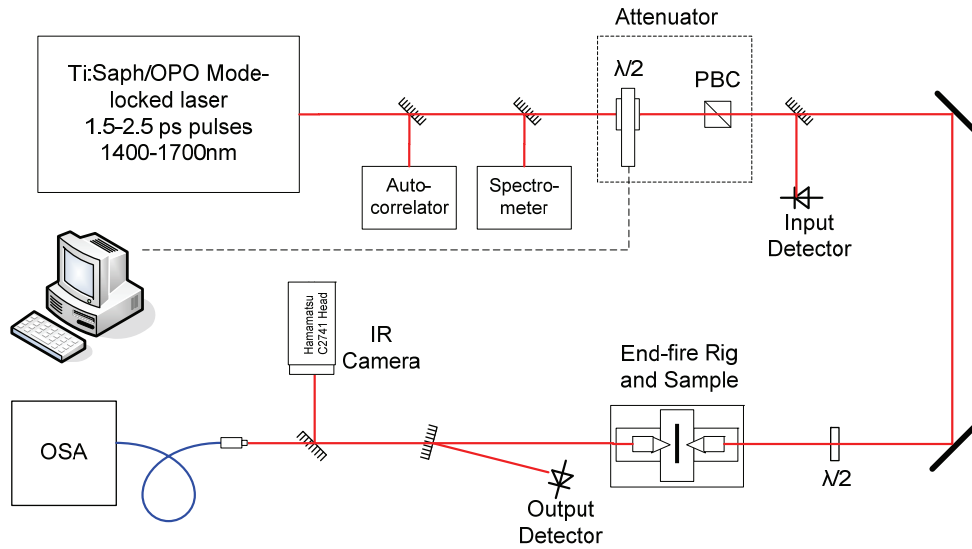


Figure 3.2: Experimental setup for measurement of nonlinear optical properties of superlattice waveguides using an OPO-based ultrafast laser system

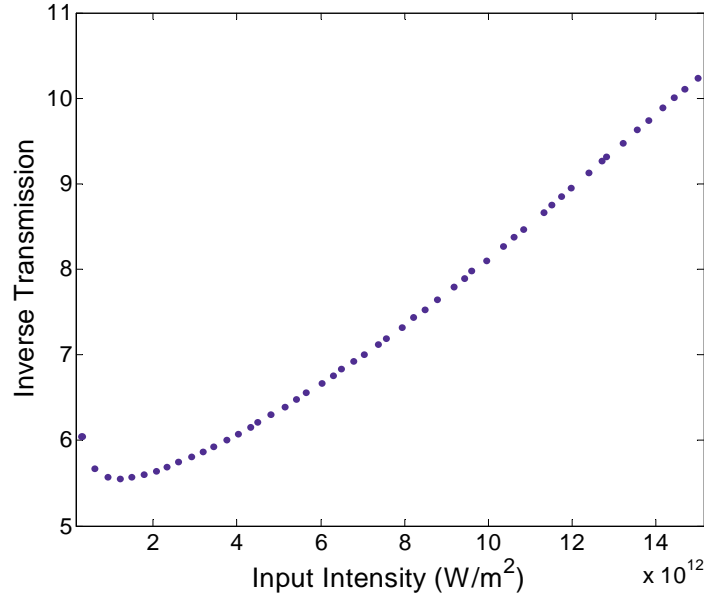


Figure 3.3: Measured inverse transmission of an as-grown superlattice waveguide at 1525 nm in the TE mode

a wavelength of 1525 nm in as-grown superlattice. At lower input intensities, the transmission behaviour is inconsistent with the general trend. This is likely due to noise in the output power detector or leakage of the orthogonal polarization through the attenuation setup. Thus, the measured transmission values at lower intensities were ignored. At higher powers, the curve slopes upwards in a linear fashion. The straight-line trend of this curve at high powers indicates that TPA is the dominant nonlinear loss mechanism for as-grown superlattice waveguides. This portion of the curve was fit to a straight line to obtain the slope of the inverse transmission.

3.2.4 Contribution of AlGaAs Buffer and Cladding Layers

The relationship between the multiphoton absorption coefficients and the bandgap of direct-gap semiconductors was studied by Wherrett [50]. Using a simplified band structure model, the TPA coefficients were found to obey the following equation [59]:

$$\alpha_2 = K \frac{\sqrt{E_p}}{n_0^2 E_g^3} F_2 \left(\frac{\hbar\omega}{E_g} \right) \quad (3.13)$$

where K is a material dependent constant, E_p is the Kane momentum, n_0 is the linear index of refraction, E_g is the bandgap energy, ω is the optical frequency, and F_2 is a function representing the band structure. The constants K and E_p are nearly material independent. The function F_2 is similar for most semiconductors and only gives the frequency dependence relative to the bandgap energy. Thus, the dominate factor in Equation (3.13) is E_g which is raised to the third power. Given known values of α_2 for one semiconductor, the values for another are approximated using the scaling rule that α_2 is proportional to E_g^{-3} .

The value of α_2 for bulk AlGaAs layer can be approximated using the scaling rules and measured coefficients for $\text{Al}_{0.18}\text{Ga}_{0.82}\text{As}$ reported by Aitchison [20]. Values for the direct bandgap of $\text{Al}_{0.18}\text{Ga}_{0.82}\text{As}$, $\text{Al}_{0.56}\text{Ga}_{0.44}\text{As}$ and $\text{Al}_{0.60}\text{Ga}_{0.40}\text{As}$ were calculated as 1.65 eV, 2.12 eV, and 2.17 eV using the empirical fit of Adachi [41]. The scaling rules give α_2 reduction factors of about 45% for the buffer and cladding layers. Values of α_2 for $\text{Al}_{0.56}\text{Ga}_{0.44}\text{As}$ using this method are shown in Figure 3.4. At a wavelength of about 1495 nm, the scaling rules yield values for α_2 of ~ 0.45 cm/W for the TE mode and ~ 0.1 cm/W for the TM mode.

Further consideration must be given to the position of the band edge relative to

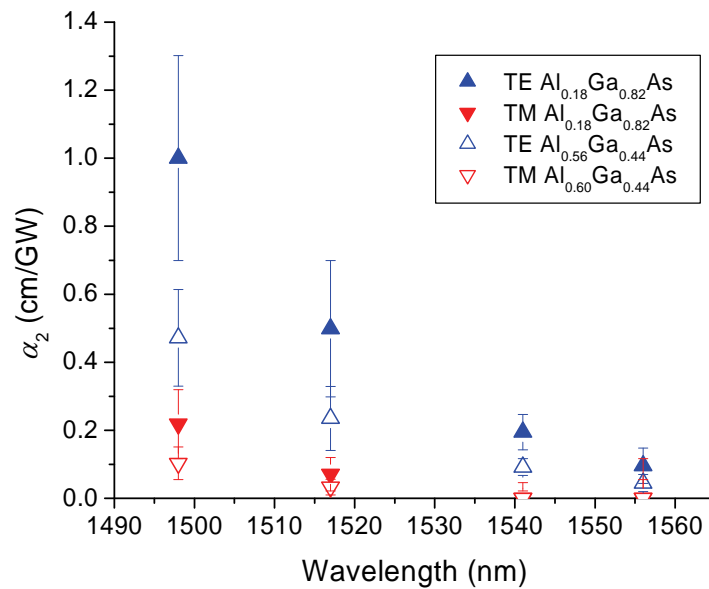


Figure 3.4: Measured TPA coefficients for bulk $\text{Al}_{0.18}\text{Ga}_{0.82}\text{As}$ [20], and scaled values for $\text{Al}_{0.56}\text{Ga}_{0.44}\text{As}$ and $\text{Al}_{0.60}\text{Ga}_{0.40}\text{As}$

the photon energies considered in this study. Wavelengths of 1500 nm and longer are detuned from the direct half-bandgap of $\text{Al}_{0.56}\text{Ga}_{0.44}\text{As}$ by ~ 150 nm. Such a large detuning indicates that TPA should be minimal, almost zero. It is instructive to bear in mind that TPA coefficients for $\text{Al}_{0.18}\text{Ga}_{0.82}\text{As}$ in the TE mode are reduced to nearly 10% of their value after only a detuning of ~ 60 nm from the half-bandgap. Based on distance from the TPA resonance from the wavelengths of interest, the TPA coefficients are assumed to be nearly zero for $\text{Al}_{0.56}\text{Ga}_{0.44}\text{As}$. Thus, along with the reduction predicted by the scaling laws, the contribution of the buffer and cladding layers is taken to be negligible.

3.2.5 Calculation of Third-order Effective Area

Given that the contribution of the cladding and buffer layers is insignificant, only the superlattice core layer needs to be considered. Using the mode profiles from Section 2.5.2 and Equation (3.11) taken over the superlattice layer, the core effective mode areas, $A_{\text{eff},\text{core}}^{(3)}$, for wavelengths between 1505 nm and 1625 nm were calculated and are shown in Figure 3.5. The TM mode has $A_{\text{eff},\text{core}}^{(3)}$ between two- and three-times larger than the TE

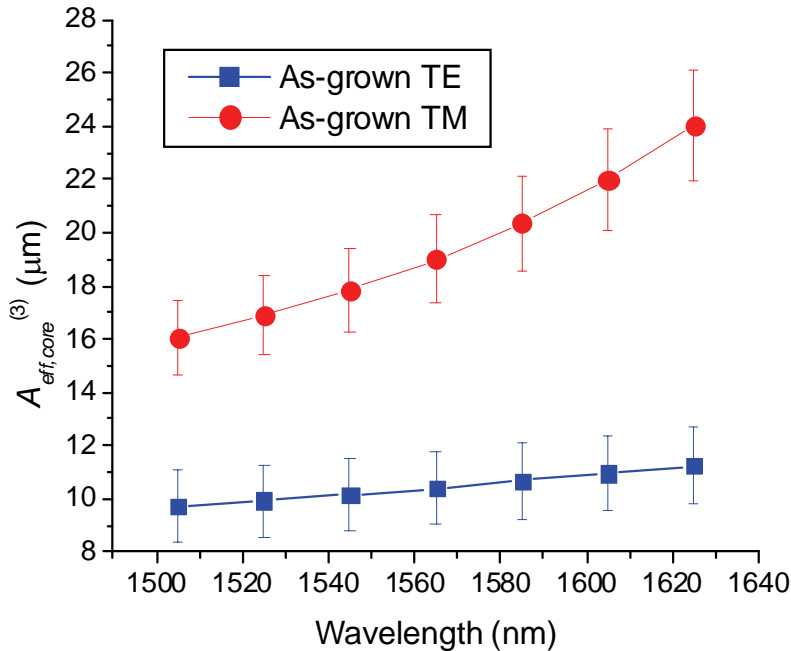


Figure 3.5: Core third-order effective mode area for as-grown superlattice rib waveguides

mode. Just as the reduced confinement of the TM mode indicated, this large difference in the $A_{eff,core}^{(3)}$ shows that the nonlinear effects will be greatly reduced in the TM mode relative to the TE mode.

The errors in the calculated values result from two sources of uncertainty: (1) the index of refraction for the superlattice, and (2) the etch depth of the rib waveguides. In the case of the superlattice index, an error of -0.001 yielded variations in $A_{eff,core}^{(3)}$ between 4% and 7% for the TM mode and < 1% for the TE mode. Uncertainty in the etch depth was estimated at 50 nm giving variations in $A_{eff,core}^{(3)}$ of up to 13% in the TE mode and 5% in the TM mode. Thus, the total error in $A_{eff,core}^{(3)}$ was calculated as ~20% in the TM mode and ~6% in the TE mode.

3.2.6 Results

The value of α_2 was calculated for the as-grown superlattice layer using measurements of the slope of the inverse transmission curves m , calculated $A_{eff,core}^{(3)}$ values, and Equation (3.4). Figure 3.6 shows α_2 for the TE and TM modes for wavelengths between 1505 nm and 1625 nm. The values are on the same order as that measured in bulk AlGaAs waveguides [20]. However, TPA is consistently stronger in the superlattice for both modes with values of α_2 being up to four-times greater. This enhancement is similar to that seen in GaAs/AlGaAs MQW waveguides [58]. A large anisotropy is present with the TE mode having α_2 values up to four-times greater than in the TM mode at photon energies near the half-bandgap. This polarization dependence in α_2 is similar to that found in bulk AlGaAs [20].

The shapes of the curves indicate several characteristics of the waveguide structure. First, the TPA coefficient rapidly increases for the TE mode as the half-bandgap is approached. However, the TM mode remains relatively flat. This shows that there is a difference in the resonance points for TE and TM polarized light. The shape of both curves is inconsistent with the known dispersion of TPA in most simple materials such as bulk AlGaAs. According to theory, the curves should monotonically decrease with increasing wavelength. However, as is seen here, the curves appear to have small

peaks between 1565 nm and 1605 nm for the TE mode, and between 1545 nm and 1565 nm for the TM mode. In Section 2.3, photoluminescence measurements indicated the presence of asymmetric GaAs quantum wells at the top of the superlattice layer with wavelengths of 780 nm in the TE mode and 767 nm in the TM mode. The half-bandgaps of these resonances lie at 1560 nm and 1534 nm, which nearly coincide with the apparent peaks of the TPA curves. Thus, there is strong evidence that these quantum wells are affecting the nonlinear properties of these waveguides.

Error in the measured values results from uncertainty in several factors. Core effective area values had errors of up to 13%, as was discussed in the previous section. Uncertainty in the values of the linear loss coefficients of up to 16% resulted in errors of less than 1%. Variation in the pulse width reading from the autocorrelator introduced errors of about 6%. The reflectivity of the facets are based on the effective index of the waveguides, which had small errors of <1% and thus can be ignored. Thus, the total error in each of the measured α_2 values ranged between 7% and 12%.

For intermixed superlattice waveguides, no changes in the transmission characteristics of TPA were observed. This was expected since the intermixed superlattice showed PL signatures that would place the TPA resonance at least 150 nm

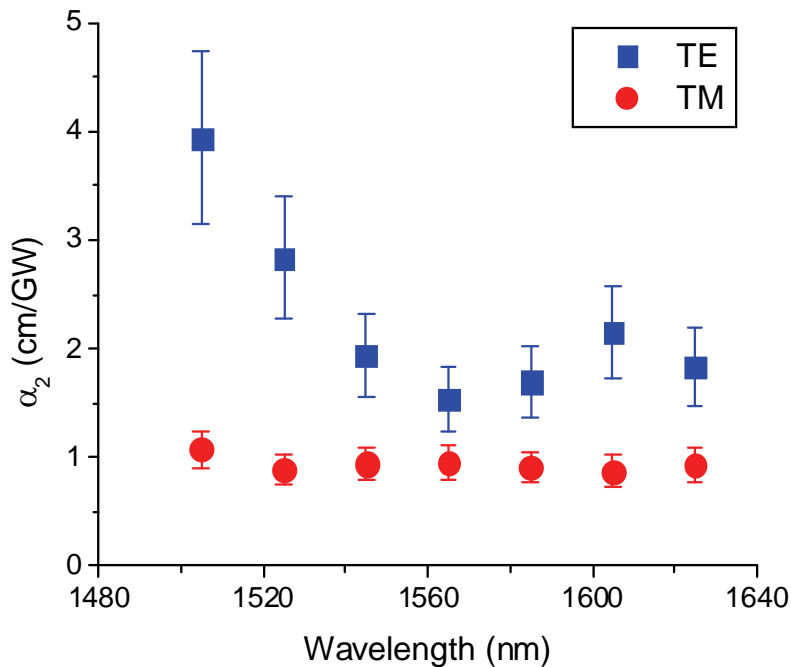


Figure 3.6: Dispersion of the TPA coefficients for as-grown superlattice below the half-bandgap

away from the wavelengths used in the experiments. Using the same arguments as were used for the TPA contribution of the buffer and cladding layers, it is assumed that the TPA coefficients for intermixed superlattice are nearly zero.

3.3 Three-photon Absorption in Intermixed Superlattice

3.3.1 Theory

Three-photon absorption is a process in which an electron transitions to the conduction band from the valence band by simultaneously absorbing three photons. As depicted in Figure 3.7, this involves two virtual transitions in which photon energies of at least one-third the bandgap are absorbed. Thus, the 3PA resonance peak occurs at wavelengths three-times longer than the single-photon absorption peak. As with TPA, indirect transitions are relatively inefficient for the same bandgap energy as direct transitions since phonon assistance is required.

3PA is associated with the fifth-order nonlinearity. It causes a change in the loss

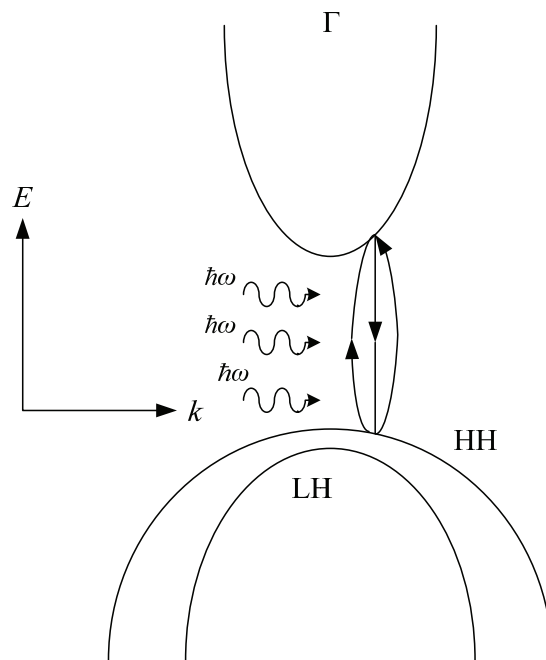


Figure 3.7: Three-photon absorption process between valence and conduction band. Reproduced from [50].

coefficient that is proportional to the square of the optical intensity as expressed in

$$\Delta\alpha = \alpha_3 I^2 \quad (3.14)$$

where α_3 is the 3PA coefficient. If TPA is negligible and 3PA is the dominant nonlinear absorption process, the propagation of a beam of light at large intensities can be described as [60]

$$\frac{dI(z)}{dz} = -\alpha_0 I(z) - \alpha_3 I^3(z). \quad (3.15)$$

Solving this equation over a propagation distance of L yields the inverse transmission squared [20]

$$\frac{1}{T^2} = \frac{1}{(1-R)^4 \eta^2 e^{-2\alpha_0 L}} + \alpha_3 \frac{(1-e^{-2\alpha_0 L})}{\alpha_0 (1-R)^2 e^{-2\alpha_0 L}} I_{in}^2. \quad (3.16)$$

As with TPA, the slope of this curve, m , is proportional to the 3PA coefficient. Thus, α_3 can be calculated as

$$\alpha_3 = m \frac{\alpha_0 (1-R)^2 e^{-2\alpha_0 L}}{1 - e^{-2\alpha_0 L}} \quad (3.17)$$

This illustrates the inverse transmission squared method for measuring 3PA.

The effective optical intensity can be calculated in the same manner as was done with TPA using the formalism of Grant [45]. For each material i in the waveguide, the fifth-order effective intensity, $I_{eff}^{(5)}$, can be calculated from the input power and the fifth-order effective area

$$A_{eff,i}^{(5)} = \left[\frac{\left[\int_{-\infty-\infty}^{\infty} \int_{-\infty-\infty}^{\infty} I(x,y) dx dy \right]^3}{\int_{(i)} I^3(x,y) dx dy} \right]^{1/2}. \quad (3.18)$$

The effective 3PA for the waveguide as a whole is the sum of the individual 3PA contributions from each material.

As with TPA, 3PA in direct-gap semiconductors was found to scale with the bandgap energy [50]. The 3PA coefficient can be calculated as

$$\alpha_3 = \frac{3^{10} \sqrt{2}}{8} \pi^2 \left(\frac{e^2}{\hbar c} \right)^3 \frac{\hbar^2 P^3}{n_0^2 E_g^7} \left[\frac{(3\hbar\omega/E_g - 1)^{1/2}}{(3\hbar\omega/E_g)^9} \right] \quad (3.19)$$

where P is the nearly material independent Kane parameter. The last term describes the dispersion of α_3 relative the one-third the bandgap. The value of α_3 scales according to E_g^{-7} , thus large bandgap differences between materials results in a large difference in the 3PA strength.

3.3.2 Previous Studies of 3PA in Semiconductors

There are only a few studies of three-photon absorption in semiconductors. Sheik-bahaei *et al.* studied 3PA in doped InSb, a narrow gap semiconductor [61]. Using a CO₂ picosecond laser system, the value of α_3 was determined to be 0.2 cm³/GW² at photon energies around 0.07 eV. 3PA was also studied in photodiodes made of the wide gap semiconductor GaN by Streltsov *et al.* [9]. Using 60 fs pulses from a Ti:sapphire laser at 820 nm, α_3 was measured to be 1.05×10^{-10} cm³/GW².

Bulk Al_{0.18}Ga_{0.82}As-core waveguides were studied for 3PA by Kang *et al.* using the inverse transmission squared method [60]. 3PA coefficients were on the order of 0.1 cm³/GW² and increased with increasing wavelength over a spectral range from 1500 nm to 1660 nm. Since the one-third bandgap for Al_{0.18}Ga_{0.82}As lies at around 2250 nm, this

behaviour is expected since the 3PA peak is being approached. In another study by Islam *et al.* [57], bulk $\text{Al}_{0.20}\text{Ga}_{0.80}\text{As}$ had α_3 values of $0.004 \text{ cm}^3/\text{GW}^2$ for wavelengths between 1660 nm and 1700 nm.

3.3.3 Calculation of Fifth-order Effective Area and Contribution of Bulk Layers

Calculation of fifth-order effective area for the intermixed superlattice core layer, $A_{\text{eff},\text{core}}^{(5)}$, was carried out using the mode profiles for intermixed waveguides from Section 2.5.2 and Equation (3.18). Figure 3.8 shows the results of this calculation for wavelengths between 1400 nm and 1600 nm. The trend is similar to that seen in the third-order effective areas for as-grown waveguides. In both polarizations, $A_{\text{eff},\text{core}}^{(5)}$ increases with increasing wavelength due to decreasing confinement. However, there is much less difference between the polarizations owing to the reduced anisotropy of the linear index of intermixed superlattice.

An error of 0.001 in the intermixed superlattice index of refraction results in an uncertainty in $A_{\text{eff},\text{core}}^{(5)}$ of up to 2% for the TE mode and 3% in the TM mode. An error of 50 nm in the etch depth of the waveguides causes an error of up to 11% for the TE mode and 5.5% in the TM mode. Thus, the total uncertainty in the value of $A_{\text{eff},\text{core}}^{(5)}$ is 13% and 8.5% for the TE and TM modes respectively.

As with TPA, the contribution of the AlGaAs buffer and cladding layers must be considered when calculating the effective area and the 3PA coefficient. The effective area of the buffer and cladding layers, $A_{\text{eff},\text{clad}}^{(5)}$, was calculated to be nearly an order of magnitude larger than $A_{\text{eff},\text{core}}^{(5)}$. This would give a contribution to $\Delta\alpha$ that is at least an order of magnitude smaller than the contribution of the core layer. Furthermore, using the scaling law of Equation (3.19), the value of α_3 for $\text{Al}_{0.56}\text{Ga}_{0.82}\text{As}$ is nearly 30% lower than in $\text{Al}_{0.50}\text{Ga}_{0.50}\text{As}$, which intermixed superlattice appears to approximate. Thus, the buffer and cladding layers should contribute to 3PA by over an order of magnitude less than the

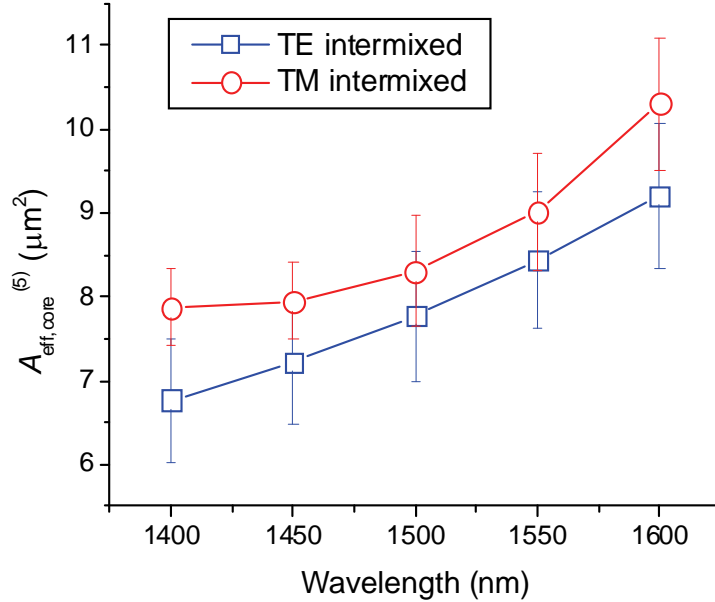


Figure 3.8: Fifth-order core nonlinear effective areas for intermixed superlattice rib waveguides

core layer. In light of this, the contribution of the buffer and cladding layers is ignored, to a first approximation.

3.3.4 Results

To measure the 3PA coefficients of intermixed superlattice, the same system as used in TPA measurements was used except that the laser was configured to emit 150 fs pulses. This increased the peak pulse power by a factor of ten to ~ 8000 W which was required to induce a sufficient amount of 3PA to observe in the transmission data. The tenfold decrease in the pulse width resulted in pulse spectral widths of ten-times larger than those used in TPA measurements. Thus, the value of α_3 at specific wavelengths is more difficult to pin down since any measurement will include the effect of all other wavelengths within the spectrum of the pulses. In order to maintain separation between measurements taken at different wavelengths, points were taken every 50 nm.

The inverse transmission squared curve for 1550 nm TM polarized light is shown in Figure 3.9. At lower powers, the transmission through the waveguides increases, which was not expected. This phenomenon may be explained by a large number of defect states located at energies within the bandgap of the intermixed superlattice. These states

become increasingly filled as the power is increased and the transmission through the waveguide increases due to a decrease in available states. At some power level, all of the defect states are filled and the transmission peaks. After this point, decreases in output power will be due to linear scattering and nonlinear absorption. In the case of the shown curve, a straight line results at high powers indicating the action of 3PA.

The value of α_3 was calculated for intermixed superlattice waveguides using measurements of the slope of the inverse transmission squared curves m , calculated $A_{eff}^{(5)}$ values, and Equation (3.17). Figure 3.10 shows the measured values for the TE and TM modes with wavelengths between 1500 and 1600 nm. In both cases, α_3 is on the order of $0.01 \text{ cm}^3/\text{GW}^2$, which on the same order of magnitude as that observed in bulk AlGaAs waveguides [20]. There is a polarization dependence with the TE mode having 3PA coefficients that are between three- and six-times larger than the TM mode.

Errors in the 3PA values measured result from many of the same sources as the TPA values in as-grown superlattice. Uncertainty in $A_{eff}^{(5)}$ values introduces an error of up to $\sim 12\%$ in the TE mode and 8% in the TM mode. Errors in the measure pulse length

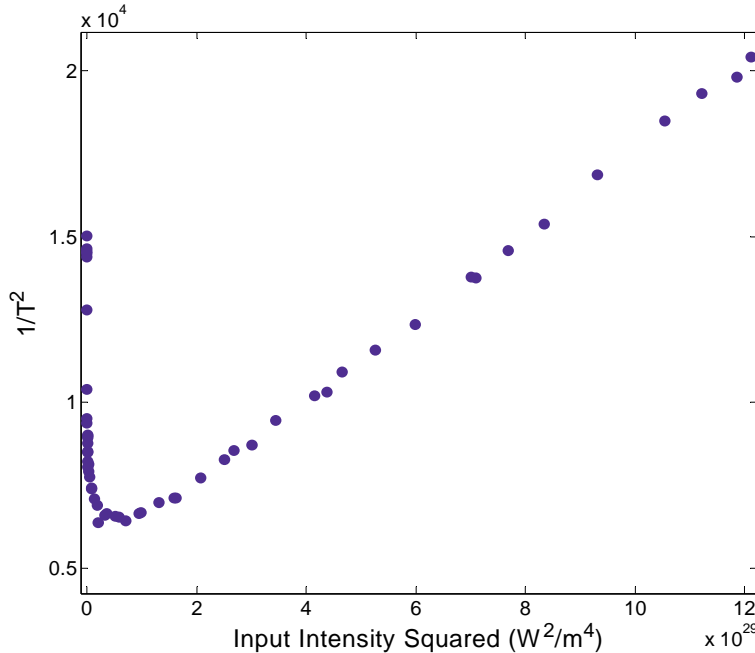


Figure 3.9: Measured inverse transmission squared curve for intermixed superlattice with TM polarized light at 1550 nm

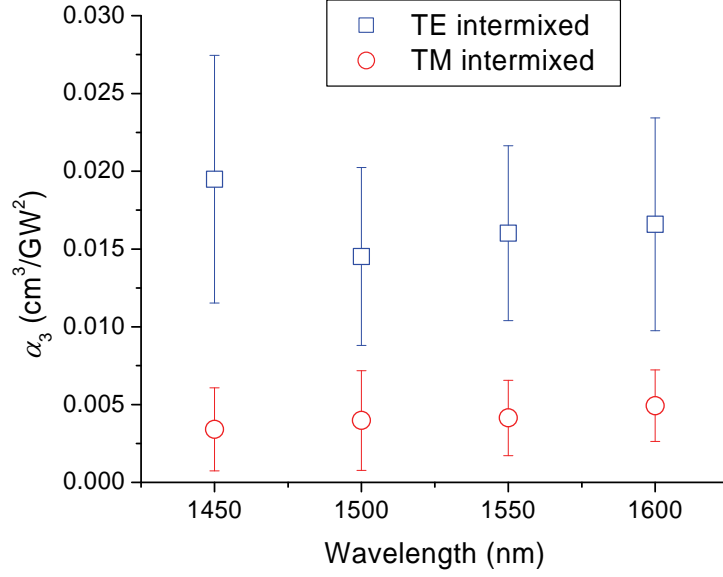


Figure 3.10: Measured 3PA values for intermixed superlattice

were estimated at 6%. The uncertainty in the measured α_0 values resulted in a variation of α_3 up to 23% in the TE mode and 57% in the TM mode. Thus, the total error in α_3 is 51% for the TE mode and 81% for the TM mode in the worst cases.

3.3.5 Comparison of 3PA to Other Sources of Optical Loss

In order to compare 3PA to other loss mechanisms in intermixed and as-grown superlattice, it is necessary to evaluate their effects on the transmission of light through a waveguide. For linear loss in the absence of nonlinear absorption, the transmission is

$$T = e^{-\alpha_0 L} \quad (3.20)$$

where L is the propagation length. For TPA in the absence of linear loss, solving Equation (3.2) gives

$$T = \frac{1}{\alpha_2 L I_{in} + 1} \quad (3.21)$$

where I_{in} is the input intensity. In the case of 3PA, Equation (3.15) can be solved with α_0 set to zero to yield

$$T = \frac{1}{\sqrt{1 + \frac{\alpha_3 I_{in}^2 L}{2}}}. \quad (3.22)$$

Each of these loss mechanisms was evaluated by calculating the length at which they lead to a loss of 3 dB at a wavelength of 1550 nm for the TE polarization. A peak input power of 100 W was chosen and the respective effective mode areas were used to calculate effective I_{in} for TPA and 3PA. Using these parameters 3 dB length for 3PA in intermixed waveguides is 2.8 m. For TPA in as-grown waveguides at 1545 nm, the 3 dB length was calculated as 3.7 mm in the TE mode, which is over three orders of magnitude smaller than 3PA in intermixed waveguides. By comparison, linear loss in intermixed waveguides requires only 1.9 mm to reach 3 dB regardless of the input power level. Thus, 3PA in intermixed superlattice is weak enough such as not to limit optical power that would be required for the Kerr effect in nonlinear elements of a PIC.

3.4 Re-emission from Nonlinear Absorption

Nonlinear absorption causes electron-hole pairs to be generated in the superlattice. Many of these carriers eventually recombine radiatively and emit light at energies around the bandgap of the superlattice. This phenomenon provided an opportunity to verify the details of the bandgap in as-grown and intermixed material by measuring the spectrum of the re-emitted light when excited by the ultra-fast laser.

The tip of a fiber optic cable was placed over the excited waveguide to collect the re-emitted light. An optical spectrometer was connected to other end of the cable to measure the spectrum. The laser system was configured to give pulse widths of ~ 150 fs and the wavelength was set to 1550 nm. This was to ensure that the intermixed sample had a sufficient amount of nonlinearly generated carriers to recombine such as to give enough light to measure reliably.

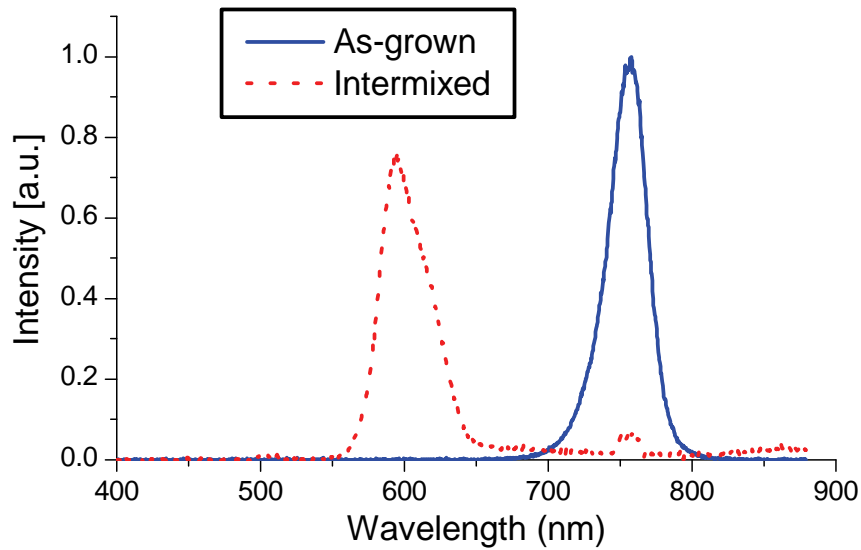


Figure 3.11: Re-emission spectra from recombination of carrier generated by nonlinear absorption.

Figure 3.11 shows the re-emission spectra for as-grown and intermixed waveguides. For as-grown superlattice, the peak occurs at a wavelength of about 757 nm. In intermixed superlattice, the peak occurs at around 596 nm. In both cases, the measured spectra closely match the photoluminescence peaks detailed in Section 2.3. Also, in the intermixed superlattice, a small peak occurs at around 750 nm. This coincides with the PL peaks of as-grown superlattice and the unintended GaAs quantum wells found at the top and bottom of the superlattice. In either case, this indicates that there may be a small amount of the superlattice toward the bottom of the core layer that was not completely intermixed.

3.5 Conclusions

In this chapter, nonlinear absorption in as-grown and intermixed superlattice waveguides has been studied. As-grown waveguides were studied for TPA at wavelengths near 1550 nm which lie just below the half-bandgap of as-grown superlattice where band tail states can cause large amounts of TPA. The effect of the bulk AlGaAs buffer and cladding layers was not considered since their TPA coefficients were estimated to be nearly zero. The strength of TPA in as-grown superlattice is nearly four-

times larger than in bulk $\text{Al}_{0.18}\text{Ga}_{0.82}\text{As}$, which is similar to the enhancement observed in GaAs/AlGaAs MQW structures. A large polarization dependence exists with the TE mode having α_2 values that are near four-times larger than in the TM mode, which is similar to the polarization dependence observed in bulk AlGaAs. Intermixed waveguides were not studied for TPA since the spectral range studied is sufficiently distant from the half-bandgap of intermixed superlattice and since transmission trends characteristic of TPA were not observed in preliminary measurements of intermixed waveguides.

Three-photon absorption was measured in intermixed superlattice waveguides using the inverse transmission squared method and 150 fs optical pulses. The value of α_3 was found to be on the same order of magnitude as bulk AlGaAs. A large polarization dependence was observed with the TE mode having α_3 value between three- and six-times larger than the TM mode. The limiting effects of 3PA in intermixed waveguides were found to be about three orders of magnitude smaller than both linear loss in intermixed waveguides and TPA in as-grown waveguides.

Re-emitted light from nonlinear absorption was measured for as-grown and intermixed waveguides. In both cases, the spectral peaks of the re-emission coincided with PL peaks measured earlier.

Chapter 4

Nonlinear Refraction by Self- and Cross-Phase Modulation

4.1 Introduction

To design practical all-optical switching devices based on the Kerr effect, it is necessary to know the value of the nonlinear refraction coefficients of the material being used. Near the half-bandgap resonance, it is also important to know how these coefficients change with wavelength and with polarization since nonlinear refraction can change drastically with either. However, measurement of these coefficients is problematic since direct measurements of changes in the index of refraction are difficult to achieve, especially in waveguide structures. Instead, indirect measurements of self-phase modulation for a single beam and cross-phase modulation between two orthogonally polarized beams must be used. Modeling the behaviour of SPM and XPM is problematic since several other phenomena such as dispersion, group velocity mismatch, and nonlinear absorption all have direct effects on the nonlinear behaviour. However, with reliable measurement techniques and comprehensive modeling, accurate nonlinear refraction coefficients for SPM and XPM can be determined.

This chapter deals with nonlinear refraction in GaAs/AlAs superlattice waveguides at wavelengths below the half-bandgap where non-resonant nonlinearities are dominant. Observations of SPM in as-grown and intermixed waveguides through measurements of spectral broadening are examined. Contributions of the AlGaAs buffer

and cladding layers of the waveguide structure are discussed and accounted for in the resulting nonlinear coefficients for the superlattice core layer. Measurements of XPM between orthogonal polarizations using a pump-probe technique and measurements of the resulting spectral broadening are looked at. For both SPM and XPM, numerical computation techniques are developed to accurately model the effects of nonlinear refraction and to extract the nonlinear coefficients.

4.2 Self-Phase Modulation in As-Grown and Intermixed Superlattice

4.2.1 Background Theory on Self-Phase Modulation and Spectral Broadening

Instantaneous changes in the refractive index due to an intense electric field result from the non-resonant optical Kerr effect. In this case, the change in the index of refraction is caused by interactions with the bound electrons without transitions to the conduction band from the valence band. From Equation (1.2), the instantaneous index change due to the third-order nonlinearity can be expressed as

$$\Delta n = n_2 I . \quad (4.1)$$

As with nonlinear absorption, the non-uniform intensity distribution of the guided mode in a waveguide must be accounted for when calculating the optical intensity. Using the same formalism as with TPA, the index change can be modeled in more detail for a waveguide structure as [45]

$$\Delta n_{eff} = \frac{n_{2,(1)} \iint_{(1)} I^2(x, y) dx dy + n_{2,(2)} \iint_{(2)} I^2(x, y) dx dy + \dots}{\iint_{-\infty-\infty}^{\infty \infty} I(x, y) dx dy} \quad (4.2)$$

where $n_{2,(i)}$ are the nonlinear refractive indexes of each material in the structure. This equation yields the same third-order effective areas as before, including the effective area of the waveguide as a whole. Thus, Equation (4.2) can be simplified as

$$\Delta n_{eff} = n_{2,eff} \frac{P}{A_{eff}^{(3)}} = n_{2,(1)} \frac{P}{A_{eff,(1)}^{(3)}} + n_{2,(2)} \frac{P}{A_{eff,(2)}^{(3)}} + \dots \quad (4.3)$$

where $n_{2,eff}$ is the effective nonlinear refraction coefficient for the waveguide.

Using this definition, the effect of the nonlinear refractive index on an optical pulse can be modeled. Maxwell's equations can be solved with the nonlinear portion of the polarization in Equation (1.1) treated as a perturbation and under the assumption of a slowly varying envelope to give a simple propagation equation expressed as [3]

$$j \frac{\partial U(z,t)}{\partial t} = -\gamma P_0 \exp(-\alpha_0 z) |U|^2 U \quad (4.4)$$

where $U(z, t)$ is the normalized pulse envelope, P_0 is the initial peak power, and γ is the nonlinear propagation coefficient which is defined as

$$\gamma = \frac{2\pi n_{2,eff}}{\lambda A_{eff}^{(3)}}. \quad (4.5)$$

This equation is readily solved as

$$U(z,t) = U(0,t) \exp[j\phi_{NL}(z,t)] \quad (4.6)$$

where $\phi_{NL}(z,t)$ is the nonlinear phase shift which is expressed as

$$\phi_{NL}(z,t) = |U(0,t)|^2 \gamma P_0 z_{eff} \quad (4.7)$$

and z_{eff} is defined as

$$z_{eff} = \frac{[1 - \exp(-\alpha_0 z)]}{\alpha_0} \quad (4.8)$$

which accounts for the linear loss. The phase shift is dependent on the power of the pulse itself. Thus, this phenomenon is known as self-phase modulation. The maximum nonlinear phase shift occurs at the pulse center where the field is largest and can be expressed as

$$\phi_{max} = \gamma P_0 z_{eff} . \quad (4.9)$$

As a result of the time dependence in the nonlinear phase shift, the instantaneous optical frequency shifts according to

$$\delta\omega(t) = -\frac{\partial \phi_{NL}(z,t)}{\partial t} = -\frac{\partial}{\partial t} \left(U(0,t)^2 \right) \gamma P_0 z_{eff} . \quad (4.10)$$

Thus, the pulse spectrum changes and generally becomes wider for a positive γ . This effect is known as SPM-induced spectral broadening. The direction of the frequency shift depends on which edge of the pulse is being acted on. As shown in Figure 4.1, on the rising edge of the pulse, the frequency change is negative causing a red shift. On the falling edge, a blue shift occurs.

The shape of the broadened spectrum is predictable given the initial pulse shape. For a Gaussian pulse, the spectral pattern indicates the approximate amount of phase shift as is shown in Figure 4.2 [3]. The pattern where the phase shift is 1.5π is commonly used as a reference point. Here, two peaks are separated by a maximal amount of dip between them. Thus, using Equation (4.9), the value of the nonlinear refraction coefficient can be solved for as

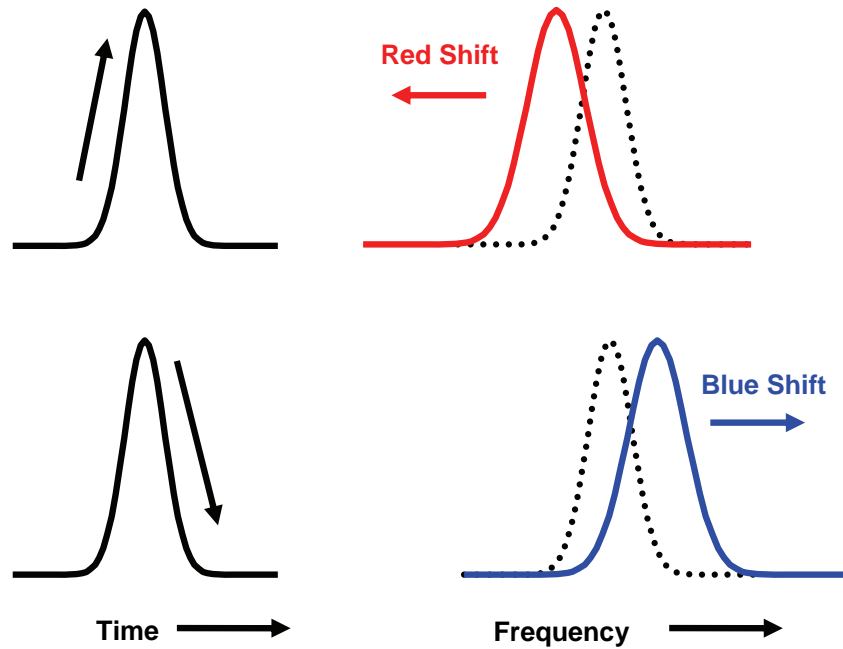


Figure 4.1: SPM-induced frequency shifts by the rising (top) and falling (bottom) edges of an optical pulse

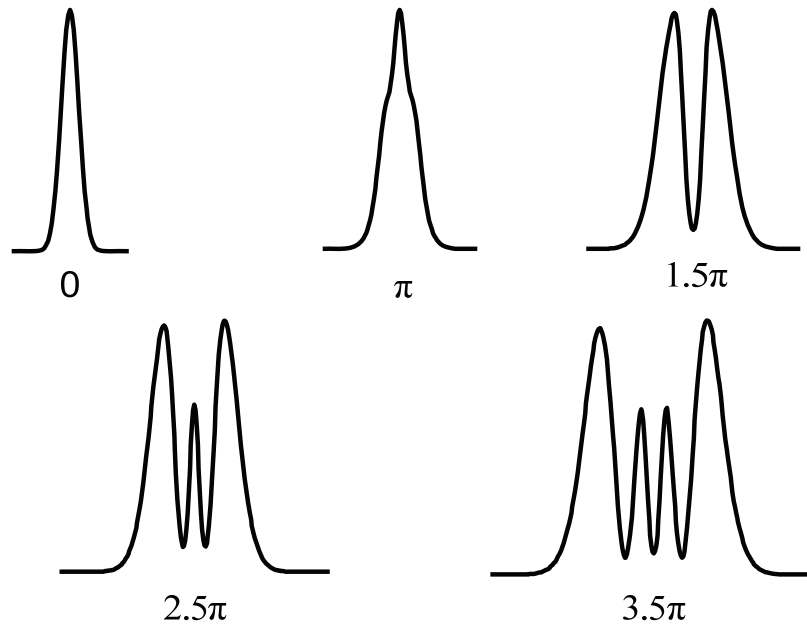


Figure 4.2: Spectral broadening patterns and associated phase shifts for a Gaussian pulse. Replicated from Ref. [3]

$$n_2 = \frac{3}{4} \frac{A_{eff}^{(3)} \lambda}{P_{0,DP} z_{eff}} \quad (4.11)$$

where $P_{0,DP}$ is the peak power at which the dual-peak pattern forms.

Dispersion and nonlinear absorption in a material influence the amount of spectral broadening. Pulse broadening by GVD has the immediate consequence of reducing the peak power of a pulse as it propagates through a medium. As a result, less power is available to induce the Kerr effect and the amount of spectral broadening is reduced. Furthermore, spectral broadening will cause the pulse to broaden more quickly resulting in even less peak power [3]. Nonlinear absorption causes a reduction in the overall power available for the Kerr effect. Also, since the pulse intensity is different at various points along the pulse envelope, nonlinear absorption results in changes of the pulse shape which influences the pattern of spectral broadening.

In order to accurately model the propagation of a pulse through a nonlinear medium, it is necessary to account for all the phenomena that can affect spectral broadening. Since Equation (4.4) only accounts for linear losses, the value of n_2 calculated by Equation (4.11) will be inaccurate when other effects are significant. A more comprehensive model leads to the Generalized Nonlinear Schrödinger Equation (GNLSE) which is expressed as [62]

$$\begin{aligned} j \frac{\partial A}{\partial z} + j \frac{\alpha_0}{2} A + j \frac{\alpha_2}{2} \frac{|A|^2}{A_{eff}^{(3)}} A + j \frac{\alpha_3}{2} \frac{|A|^4}{(A_{eff}^{(5)})^2} A - \frac{\beta_2}{2} \frac{\partial^2 A}{\partial t^2} - j \frac{\beta_3}{6} \frac{\partial^3 A}{\partial t^3} \\ + \frac{2\pi n_2}{\lambda A_{eff}^{(3)}} \left[|A|^2 A + \frac{2j}{\omega} \frac{\partial}{\partial t} (|A|^2 A) \right] = 0. \end{aligned} \quad (4.12)$$

The terms involving α_0 , α_2 , and α_3 account for linear and nonlinear absorption. GVD and third-order dispersion are described by the terms with β_2 and β_3 . Third-order nonlinearities related to the Kerr effect are described by the last two terms. The first of these terms describes SPM. The second accounts for an effect known as self-steepening which becomes important at pulse lengths less than 1 ps. Unlike the simple propagation

model of Equation (4.4), the GNLSE does not have a simple analytical solution. Thus, it is necessary to solve the GNLSE numerically.

4.2.2 Previous Studies of SPM in Semiconductors

The Kerr effect was studied in bulk crystalline silicon by Dinu *et al.* by using the Z-scan technique and femtosecond pulses [54]. The value of n_2 was measured to be $0.45 \times 10^{-13} \text{ cm}^2/\text{W}$ at 1540 nm and $0.26 \times 10^{-13} \text{ cm}^2/\text{W}$ at 1270 nm, which is about two orders of magnitude larger than n_2 in silica. Despite the use of wavelengths above the half-bandgap of silicon, free carriers generated by nonlinear absorption and thermal effects were deemed to have a negligible effect on nonlinear refraction. Further studies of silicon were carried out by Boyraz *et al.* on SPM-induced spectral broadening in silicon-on-insulator (SOI) waveguides [63]. Measured output spectra for a 4 ps pulse with a center wavelength of around 1559 nm showed a spectral broadening factor of $2\times$ for a peak pulse power of 110W. Using a numerical solution of a simplified GNLSE based on the split-step Fourier method [3], broadening factors as high as $5\times$ were predicted for input powers $10\times$ larger than those used in experiments.

Theoretical studies on nonlinear refraction in zinc-blende semiconductors were undertaken by Hutchings and Wherrett [64]. Anisotropy in the nonlinear properties of GaAs and InSb for photon energies below the bandgap was found to be the result of interactions with higher conduction-band sets. This anisotropy was confirmed in experiments on the polarization dependence of nonlinear refraction in bulk AlGaAs waveguides carried out by Hutchings *et al.* [65]. Waveguides with a 1.0 μm -thick $\text{Al}_{0.18}\text{Ga}_{0.82}\text{As}$ core layer, 4.0 μm -thick $\text{Al}_{0.40}\text{Ga}_{0.60}\text{As}$ lower cladding, and a 1.5 μm -thick $\text{Al}_{0.30}\text{Ga}_{0.70}\text{As}$ upper cladding were tested with 10-ps pulses at a wavelength of 1546 nm. It was determined using the dual-peak spectral pattern as a reference that n_2 for the TE mode was $\sim 1.3 \times 10^{-13} \text{ cm}^2/\text{W}$. To produce the same degree of spectral broadening in the TM mode, about 27% more transmitted power was required.

The dispersion of the nonlinear refraction coefficients in bulk AlGaAs was studied at wavelengths just below the half-bandgap by Aitchison *et al.* [20]. The waveguide structure consisted of a 1.5 μm -thick $\text{Al}_{0.18}\text{Ga}_{0.82}\text{As}$ core layer which was clad

on either side by $\text{Al}_{0.24}\text{Ga}_{0.76}\text{As}$. Nonlinear refraction coefficients were determined from observations of SPM-induced spectral broadening. At 1550 nm, n_2 was $\sim 1.50 \times 10^{-13} \text{ cm}^2/\text{W}$ in the TE mode and $\sim 1.43 \times 10^{-13} \text{ cm}^2/\text{W}$ in the TM mode. The polarization dependence was consistently between 5% and 10% across the studied spectral range.

Studies on the spectral evolution of high power femtosecond pulses in bulk AlGaAs waveguides were carried out by Modotto *et al.* [62]. A 0.6 μm -thick core layer of $\text{Al}_{0.20}\text{Ga}_{0.80}\text{As}$ was sandwiched between $\text{Al}_{0.40}\text{Ga}_{0.60}\text{As}$ cladding layers to create the waveguiding structure. For wavelengths of around 1520 nm, the spectrum was found to broaden and shift toward shorter wavelengths with increasing power. Computer modeling of the GNLSE by the split-step Fourier method [3] found that the blue shift was caused by initial asymmetry in the input pulse shapes.

Experiments on nonlinear refraction in GaAs/AlGaAs MQW waveguides were carried out by Yang *et al.* [58]. Measured n_2 values for the TE mode were $1.5 \times 10^{-13} \text{ cm}^2/\text{W}$ to $3.5 \times 10^{-13} \text{ cm}^2/\text{W}$ for wavelengths between 1480 nm and 1660 nm. In the TM mode, n_2 was $\sim 1.0 \times 10^{-13} \text{ cm}^2/\text{W}$ for wavelengths longer than 1550 nm. Immediately below 1550 nm, the value of n_2 increased rapidly to $\sim 4.0 \times 10^{-13} \text{ cm}^2/\text{W}$ at a wavelength of about 1500 nm. This peak in the nonlinear behaviour was attributed to exciton resonances in the quantum wells for wavelengths between 1490 nm and 1530 nm.

The effect of QWI on the nonlinear coefficients of GaAs/AlGaAs MQW waveguide was examined by Hamilton *et al.* [66]. The MQW layer of the waveguides tested were made up of 78 periods of 2.8 nm-wide GaAs wells separated by 10.0 nm-wide $\text{Al}_{0.40}\text{Ga}_{0.60}\text{As}$ barriers. Patterned silica caps were used to create disordered regions by IFVD while gallium oxide covering other areas of the wafer suppressed the disordering process. Waveguides in non-disordered regions were measured to have n_2 values of $2.6 \times 10^{-13} \text{ cm}^2/\text{W}$ for the TE mode and $3.3 \times 10^{-13} \text{ cm}^2/\text{W}$ for the TM mode at a wavelength of 1550 nm. Disordered regions showed PL shifts of ~ 40 nm towards shorter wavelengths and measured nonlinear refraction coefficients were more than 60% reduced when compared to non-disordered regions.

4.2.3 Nonlinear Refraction in the Buffer and Cladding Layers

In order to isolate the nonlinear refraction coefficient of the superlattice from the rest of the waveguide structure, it is necessary to find the contribution of the buffer and cladding layers to the overall nonlinear behaviour of the waveguides. The compositions used in these layers, $\text{Al}_{0.56}\text{Ga}_{0.44}\text{As}$ and $\text{Al}_{0.60}\text{Ga}_{0.40}\text{As}$, have not been studied specifically in the past. By using available theoretical approaches and the scaling laws they yield, approximate n_2 values for the bulk layers can be calculated. However, this approach is complicated by the fact that AlGaAs compositions with Al mole ratios greater than 0.45 have indirect bandgaps. Since the scaling laws are based on the bandgap energy, it is necessary to evaluate the effect of the indirect bandgap of AlGaAs on nonlinear refraction.

Theoretical treatment of nonlinear refraction in direct gap semiconductors was carried out by Sheik-Bahae *et al.* [12, 59]. Using a two-band model, the value of n_2 was derived from the theoretical expression for TPA in Equation (3.13) and the Kramers-Krönig transformation:

$$n_2 = K' \frac{\sqrt{E_p}}{n_0 E_g^4} G_2 \left(\frac{\hbar\omega}{E_g} \right) \quad (4.13)$$

where K' is a material-independent constant, n_0 is the index of refraction, E_p is a nearly material-independent constant related to the Kane momentum, E_g is the direct bandgap energy, and G_2 is a function describing the dispersion relative to the bandgap energy. This expression shows that n_2 is proportional to E_g^{-4} . Thus, nonlinear refraction quickly becomes weaker with increasing bandgap energy. The dispersion trend of function G_2 was found to be [12]

$$G_2(x) = \frac{-2 + 6x - 3x^2 - x^3 - \frac{3}{4}x^4 - \frac{3}{4}x^5 + 2(1-2x)^{3/2} \Theta(1-2x)}{64x^6} \quad (4.14)$$

where $\Theta(u)$ is the unit step function.

Using the scaling laws set out in Equation (4.13), n_2 values for $\text{Al}_{0.56}\text{Ga}_{0.44}\text{As}$ and $\text{Al}_{0.60}\text{Ga}_{0.40}\text{As}$ were calculated using n_2 values measured for $\text{Al}_{0.18}\text{Ga}_{0.82}\text{As}$ [20]. The resulting values are shown in Figure 4.3 for the TE and TM modes between 1505 nm and 1625 nm. The points shown were scaled from linearly interpolated values of measured data to obtain points needed for calculating the n_2 of superlattice in Section 4.2.7. Scaled values were between 18% and 25% of the values for $\text{Al}_{0.18}\text{Ga}_{0.82}\text{As}$. In both polarizations, $\text{Al}_{0.60}\text{Ga}_{0.40}\text{As}$ has n_2 values that are only 9% smaller than the $\text{Al}_{0.56}\text{Ga}_{0.44}\text{As}$ n_2 values. These values show that the n_2 of the buffer and cladding layers can contribute significantly to the overall nonlinear refraction of the waveguide.

The effect of the indirect bandgap on nonlinear refraction was studied by Dinu [51]. By accounting for phonon interactions in TPA, the following expression for n_2 was derived using the Kramers- Krönig transformation:

$$n_2(\omega) = C_2 \frac{c\hbar}{\pi E_{ig}} G_2^{ind} \left(\frac{2\hbar\omega}{E_{ig}} \right) \quad (4.15)$$

where C_2 is a material dependent constant, c is the speed of light, E_{ig} is the indirect

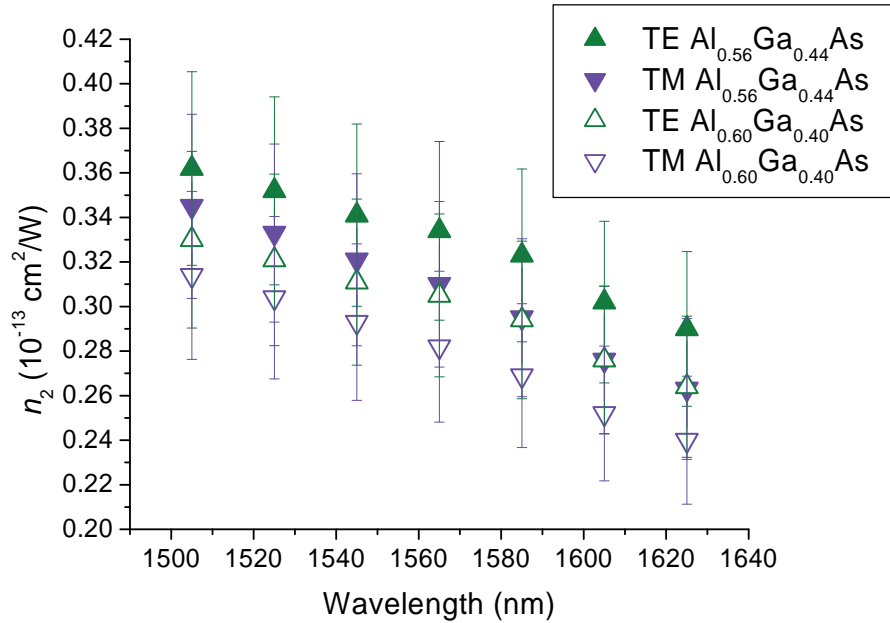


Figure 4.3: Spectral dependence of n_2 for $\text{Al}_{0.56}\text{Ga}_{0.44}\text{As}$ and $\text{Al}_{0.60}\text{Ga}_{0.40}\text{As}$ scaled from measured values of $\text{Al}_{0.18}\text{Ga}_{0.82}\text{As}$

bandgap energy, and G_2^{ind} represents frequency dependence. From the material parameters, C_2 can be calculated as

$$C_2 = \frac{Z_A^2 E_{ph} (2N_{K_x} + 1 \pm 1)}{8\rho c_s^2 E_{ig}^3} \sqrt{\frac{m_c^3}{m_v} \left(\frac{128e^4}{\pi^3 \hbar^3 (\epsilon_0 n_0 c)^2} \right)} \times \left\{ \int_0^1 dx \sqrt{(1-x)x} \left[\sqrt{1-x} + \sqrt{x \left(\frac{m_v}{m_c} \right)} \right]^4 \right\} \quad (4.16)$$

where Z_A is the acoustic deformation potential, E_{ph} is the phonon energy, N_{K_x} is the phonon occupation number, ρ is the density, c_s is the speed of sound, E_{ig} is the indirect bandgap energy, m_c is the carrier effective mass for the conduction band, and m_v is the carrier effective mass for the valence band. The plus/minus sign accounts for the emission/absorption of a phonon. The frequency dependence relative to the half-bandgap energy is

$$G_2^{ind} \left(\frac{2\hbar\omega}{E_{ig}} \right) = \int_0^\infty \frac{x^4}{(x+1)^8 \left(x+1 - \frac{2\hbar\omega}{E_{ig}} \right)} dx. \quad (4.17)$$

By substituting Equation (4.16) into Equation (4.15), the following expression results:

$$n_2(\omega) = C_2' \frac{c\hbar}{\pi E_{ig}^4} G_2^{ind} \left(\frac{2\hbar\omega}{E_{ig}} \right) \quad (4.18)$$

where the E_{ig} has been pulled out of C_2 to give the constant C_2' . The indirect bandgap yields the same dependence on the bandgap as does the direct bandgap with n_2 being proportional to E_{ig}^{-4} . However, the value of n_2 depends greatly on the phonon-related parameters of the semiconductor such as Z_A and E_{ph} . Furthermore, the value of

N_{K_x} strongly depends on temperature. Thus, the scaling laws for indirect transitions are somewhat different than for direct transitions.

The contribution of the indirect bandgap to the optical Kerr effect in $\text{Al}_{0.56}\text{Ga}_{0.44}\text{As}$ was calculated using Dinu's formulae to evaluate its significance. Table 4.1 lists the parameters at room temperature for $\text{Al}_{0.56}\text{Ga}_{0.44}\text{As}$ and $\text{Al}_{0.60}\text{Ga}_{0.40}\text{As}$ that were used in the calculations. For wavelengths around 1550 nm, the value of n_2 calculated for the indirect bandgap was on the order of $0.001 \times 10^{-13} \text{ cm}^2/\text{W}$, which is over two-orders of magnitude smaller than the values calculated for the direct bandgap. Compared to the effect of the direct bandgap, the indirect bandgap contributes little to the

Table 4.1: Parameters for calculation of nonlinear refraction constant for indirect bandgap of AlGaAs buffer and cladding layers

	$\text{Al}_{0.56}\text{Ga}_{0.44}\text{As}$	$\text{Al}_{0.60}\text{Ga}_{0.40}\text{As}$	Notes
Z_A	6.028 eV	5.580 eV	Source: [41]
E_{ph}	28 eV	28 eV	Used longitudinal acoustic phonon energies for GaAs, Source [67]
E_{ig}	2.014 eV	2.026 eV	Source: [41]
ρ	4.429 g/cm ³	4.365 g/cm ³	Source: [29]
N_{K_x}	0.4979	0.4979	Calculated using Equation (8) in Ref. [51]
c_s	$5.93 \times 10^5 \text{ cm/s}$	$5.97 \times 10^5 \text{ cm/s}$	Used [111] LA sound velocity in Table 4.8 of Ref. [29]
m_c	$0.41m_0$	$0.41m_0$	Used GaAs transverse and longitudinal value for X-band minima in Table 9.4 of Ref. [29] and density-of-states average according to Ref. [51]
m_v	$0.58m_0$	$0.59m_0$	Linearly interpolated from HH data in Table 9.9 of Ref. [29]
n_0	3.089	3.070	Wavelength is 1550 nm, Source: [44]

overall nonlinear behaviour. Thus, phonon-assisted nonlinear refraction of the buffer and cladding layers can be ignored.

In order to include the contribution of the buffer and cladding layers to the total Kerr effect in the waveguides, the third-order effective area for these layers must be calculated. Since the difference in the n_2 values between the buffer and cladding layers is small, both layers can be considered as a single material having a uniform nonlinearity. Thus, a single effective area that includes both the buffer and cladding layer can be calculated. These values are shown in Figure 4.4. While the $A_{eff,clad}^{(3)}$ values are larger than the core effective areas, they are not large enough that the contribution of the bulk layers can be ignored. It is also necessary to calculate the effective area of the waveguide where the nonlinearity is assumed to be uniform across the whole structure. The value of $A_{eff,wg}^{(3)}$, shown in Figure 4.5, were used when calculating the $n_{2,eff}$ of the waveguide. Error in the shown values results from a ± 50 nm uncertainty in the etch depth and a ± 0.001 uncertainty in the linear refractive index of superlattice.

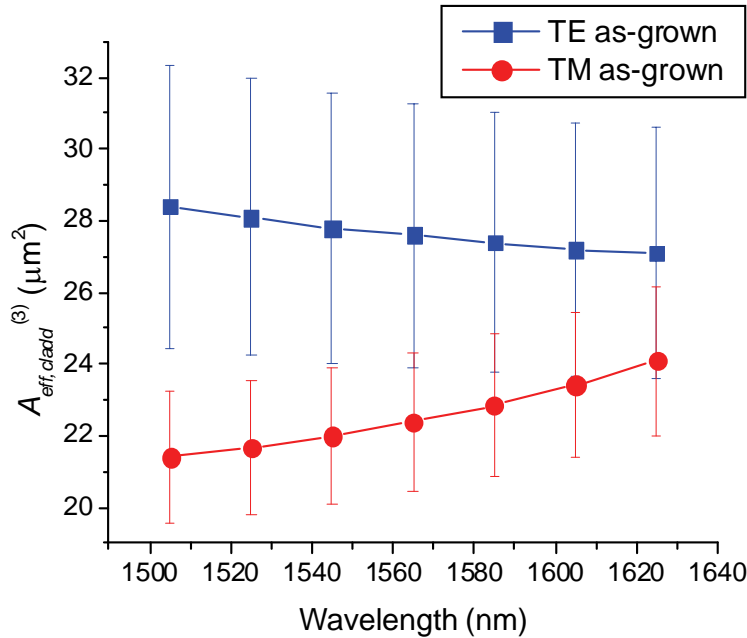


Figure 4.4: Cladding third-order effective area for as-grown superlattice waveguides

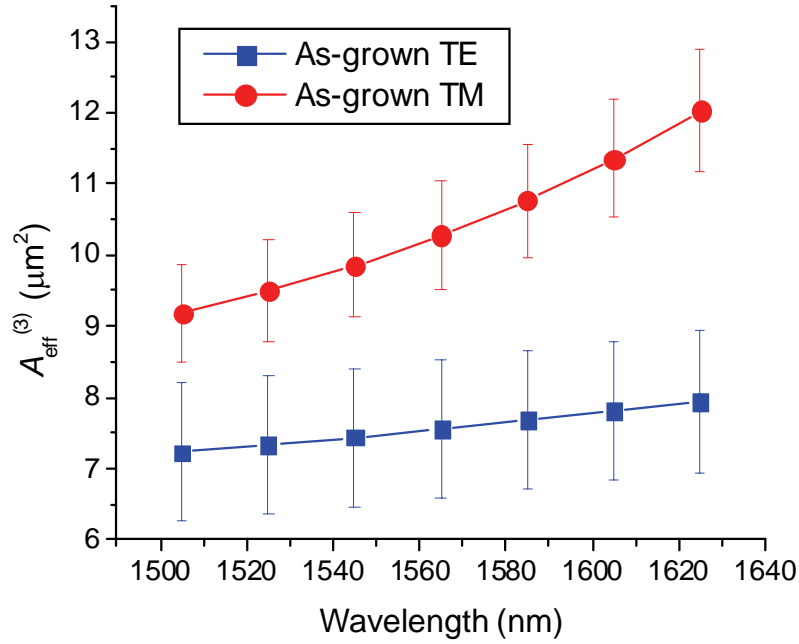


Figure 4.5: Waveguide third-order effective area for as-grown superlattice waveguides.

4.2.4 Theoretical Predictions for Superlattice

As was discussed in Chapter 1, the third-order nonlinear behaviour of a material is related to third-order susceptibility tensor. For the single frequency case in zinc-blende semiconductors such as AlGaAs, the four independent, non-zero tensor elements are reduced to three. In the case of a superlattice, these tensor elements break down into eight [28]:

$$\begin{aligned}
 \chi_{xxxx}^{(3)} &\rightarrow \chi_{xxxx}^{(3)}, \chi_{zzzz}^{(3)} \\
 \chi_{xyxy}^{(3)} &\rightarrow \chi_{xyxy}^{(3)}, \chi_{xzxz}^{(3)}, \chi_{zxzx}^{(3)} \\
 \chi_{xxyy}^{(3)} &\rightarrow \chi_{xxyy}^{(3)}, \chi_{xxzz}^{(3)}, \chi_{zzxx}^{(3)}.
 \end{aligned} \tag{4.19}$$

Of these, four are related to SPM ($\chi_{xxxx}^{(3)}, \chi_{zzzz}^{(3)}, \chi_{xyxy}^{(3)}, \chi_{xxyy}^{(3)}$) while the rest are related to four-wave mixing and XPM. Nonlinear refraction coefficients can be calculated from the real part of the tensor element according to [28]

$$n_2(\omega) = \frac{3}{4\varepsilon_0 c n_0^2} \text{Re}[\chi_{eff}^{(3)}(-\omega, \omega, \omega)] \quad (4.20)$$

where ε_0 is the electric permittivity of free space, c is the speed of light, and n_0 is the linear index of refraction. The effective third-order nonlinear susceptibility, $\chi_{eff}^{(3)}$, is $\chi_{zzzz}^{(3)}$ for the TM polarization and $(\chi_{xxxx}^{(3)} + 2\chi_{xyxy}^{(3)} + \chi_{xyyx}^{(3)})/2$ for the TE polarization. As a result of the break down of the tensor elements and the composition of the effective coefficients, SPM in as-grown superlattice was expected to be highly anisotropic [28].

Theoretical predictions of the nonlinear susceptibility coefficients in 14:14 GaAs/AlAs superlattice were developed by Hutchings [28]. Using a 14 band $\mathbf{k}\cdot\mathbf{p}$ model to calculate the electronic band structure of superlattice [68], Hutchings calculated the eight independent non-zero tensor elements with the $\mathbf{A}\cdot\mathbf{p}$ perturbation method [69]. This method proved to be more powerful than other simpler techniques such as the effective mass approximation since it can account for band nonparabolicity, anisotropy, and

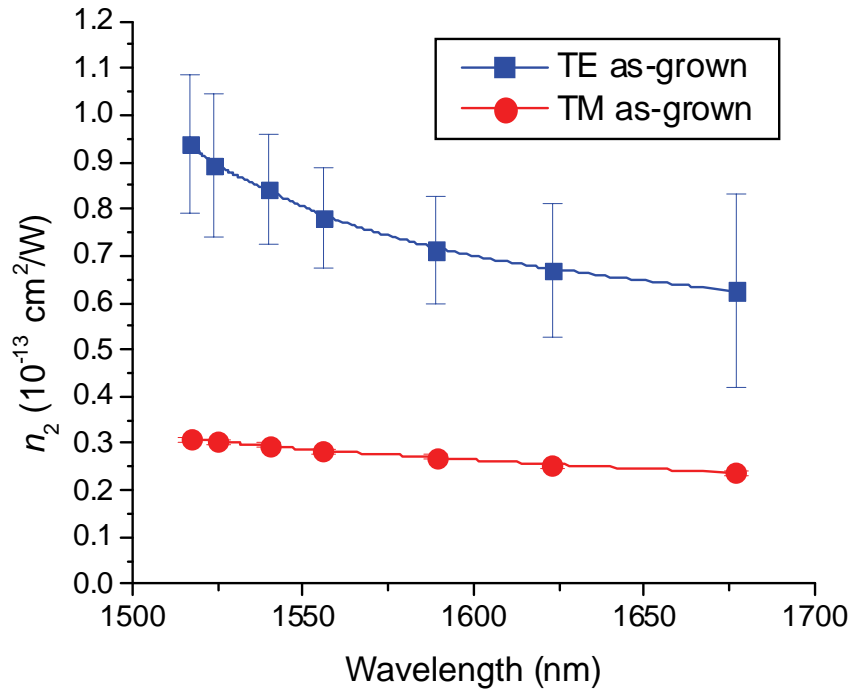


Figure 4.6: Theoretical n_2 values for as-grown superlattice calculated from Ref. [28]

noncentrosymmetry which directly affect the nonlinear coefficients.

For SPM, the value of n_2 was calculated using Equation (4.20) with the predicted effective susceptibility coefficients for the TE and TM polarizations and are shown in Figure 4.6. In both cases, the nonlinear coefficients are on the same order of magnitude as bulk AlGaAs. However, the TM polarization has a significantly suppressed nonlinearity, which is between 30% and 40% that of the TE polarization. Hence, a large polarization dependence that decreases with increasing wavelength was predicted. This is the result of the lifting of the heavy-hole band energy over the light-hole band, and the breaking of the degeneracy in the nonlinear susceptibility due to asymmetry in the structure. However, n_2 was predicted to be smaller in superlattice by about 20-30% compared to bulk Al_{0.18}Ga_{0.82}As. Uncertainty in the shown values results from numerical error reported by the quadrature routine of the algorithm [28].

Nonlinear susceptibility coefficients were also predicted for intermixed superlattice with a diffusion length of 20 monolayers [28]. In this case, the superlattice reverts back into an average alloy of AlGaAs and the tensor elements become degenerate. This is illustrated in Figure 4.7 which shows the calculated n_2 values for the TE and TM

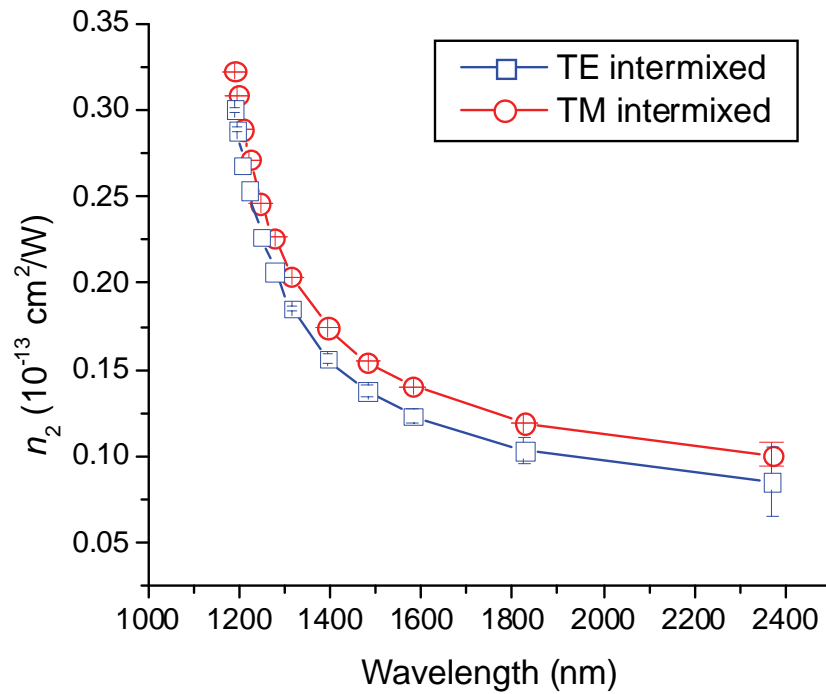


Figure 4.7: Theoretical n_2 values for intermixed superlattice calculated from Ref. [28]

modes which are related to the $\chi_{xxxx}^{(3)}$ and $\chi_{zzzz}^{(3)}$ tensor components respectively. Clearly, the difference between the two polarizations has become substantially reduced with the values being nearly the same. Furthermore, the resonance point has been shifted to a shorter wavelength. For wavelengths near 1550 nm, n_2 is reduced to about one-sixth the value for the TE mode in as-grown superlattice. This shows that intermixing has effectively reduced the nonlinearity to the point where intermixed superlattice can be considered as being linear.

4.2.5 Experimental Methods

Measurements of nonlinear refraction may be done by a number of methods that utilize at least one of the observable consequences of the optical Kerr effect. For instance, the Z-scan technique is based on the self-focusing effect and has been used to characterize nonlinear refraction in a number of materials [70]. However, this technique is only appropriate for large bulk materials. Since it is impractical to grow large epitaxial layers of bulk AlGaAs and superlattice, measurements of the Kerr effect in these materials requires a different approach. Another method is to measure the spectral broadening induced by SPM [3]. Since the spectrum changes in a predictable manner, the value of n_2 can be extracted by matching data to modeled spectral changes calculated by a computer.

Measurements of SPM-induced spectral broadening in superlattice waveguides was carried out using the experimental setup described in Section 3.2.3. The laser power was stepped from low power to high power and the resulting output spectrum from the excited waveguide was measured by the optical spectrum analyzer at each step. For as-grown superlattice waveguides, the laser was configured to give 1.5 ps to 2.5 ps pulses. Spectral widths of the pulses were between 2.0 nm to 4.0 nm, which gave good spectral resolution.

4.2.6 Computer Simulation by the Split-step Fourier Method

In order to accurately model the effects of nonlinear refraction, it is necessary to account for all of the parameters that affect spectral broadening. This includes the material parameters such as GVD, linear loss, TPA, and 3PA. Pulse characteristics such as temporal shape and chirp will also affect the spectral broadening pattern. The GNLSE accounts for all of relevant material parameters and pulse parameters. However, this equation does not readily yield an analytical solution and a numerical solution is required.

The split-step Fourier method is a simple and fast technique for solving the propagation equation [3]. In this method, the GNLSE of Equation (4.12) is divided into a linear term and a nonlinear term according to

$$j \frac{\partial A}{\partial z} = (\hat{D} + \hat{N})A \quad (4.21)$$

where \hat{D} is a differential operator accounting for dispersion and loss which is defined as

$$\hat{D} = \frac{\beta_2}{2} \frac{\partial^2}{\partial t^2} - j \frac{\beta_3}{6} \frac{\partial^3}{\partial t^3} - j \frac{\alpha_0}{2} \quad (4.22)$$

and \hat{N} accounts for nonlinear effects and linear loss according to

$$\hat{N} = -j \frac{\alpha_2}{2} \frac{|A|^2}{A_{eff}^{(3)}} - j \frac{\alpha_3}{2} \frac{|A|^4}{A_{eff}^{(5)}} - \frac{2\pi n_2}{\lambda A_{eff}^{(3)}} \left(|A|^2 + \frac{2j}{\omega A} \frac{\partial}{\partial t} (|A|^2 A) \right). \quad (4.23)$$

Over a small propagation distance, Δz , the dispersion and nonlinearity can be thought of as acting independently of each other. Thus, the solution to the Equation (4.21) for propagation over an interval Δz can be approximated as

$$A(z + \Delta z, t) = \exp(\Delta z \hat{D}) \exp(\Delta z \hat{N}) A(z, t). \quad (4.24)$$

Calculation of the dispersion term can be carried out in the frequency domain using the Fourier transform according to

$$\exp(\Delta z \hat{D})B(z, t) = \{F^{-1} \exp(\Delta z \hat{D}(j\omega))F\}B(z, t) \quad (4.25)$$

where F is the Fourier transform operator and B is the intermediary pulse envelope being acted on. This method simplifies the calculation by replacing the time differential operators with $j\omega$ thus yielding a scalar equation that is fast and simple to evaluate. By choosing an appropriately sized Δz , the propagation of a pulse through a nonlinear material can be simulated using a beam propagation method (BPM) on a computer within a reasonable amount of time.

The optical pulse envelope A can be approximated as a super-Gaussian function of the form [3]

$$A(0, t) = \exp\left[-\frac{1 + jC}{2} \left(\frac{t}{t_0}\right)^{2m}\right] \quad (4.26)$$

where t_0 is the pulse half-width at the $1/e$ -intensity point, C is the chirp parameter, and m is the super-Gaussian parameter. The FWHM of the pulse is related to t_0 by [3]

$$t_{FWHM} = 2\sqrt{\ln(2)}t_0. \quad (4.27)$$

For $C < 0$, the pulse has a linear down-chirp, and for $C > 0$, the pulse has a linear up-chirp. The m parameter controls the shape of the pulse. For $m > 1$, the pulse edges become steeper and the pulse peak flattens out. Both chirp and m result in a non-transform-limited pulse. This may be used to explain initial spectral widths of pulses used in experiments. Furthermore, these parameters affect the amount and pattern of spectral broadening output from the computer simulation. By manipulating the parameters of the pulse and the material, the simulation results can be made to closely match the data measured in experiments.

A BPM simulator was developed was developed in MATLAB to numerically solve the GNLSE based on the split-step Fourier method based on code originally developed by Modotto in Ref. [62] (see Appendix B). Fast-Fourier transforms (FFT) were used to transform the data back and forth from the frequency domain. With appropriate parameters, simulations were completed within a reasonable time of about one minute on a 2.4 GHz Intel Pentium 4 processor for a single propagation through a length of 1.2 cm. The simulator was run multiple times with increasing input pulse power in order to replicate the spectral evolution data measured in laboratory experiments. With 20-30 power levels, complete simulations took between 20-30 minutes to run.

4.2.7 Results for As-grown Superlattice

SPM-induced spectral broadening was measured for both the TE and TM modes in as-grown superlattice waveguides. Figure 4.8 depicts the measured spectrum of output pulses with increasing input power at a wavelength of 1545 nm for the TE and TM polarizations. The spectral pattern indicates phase shifts of up to 2π in the TE mode at high powers. A dual-peak pattern is found in the middle of the plot. The dotted lines indicate the points where the dip in the middle of the spectrum has reached a minimum. For each wavelength examined in these experiments, this point was used as a reference for determining the value of n_2 for that wavelength. The polarization dependence of spectral broadening is evident from the observed patterns. For the TE mode, the dual-peak point occurs at a peak power of ~ 58 W. This same point occurs in the TM mode at a power of ~ 240 W, which is nearly four-times greater. A small amount of asymmetry is present in the spectral patterns and is likely due to asymmetry in the temporal profile of the input pulses.

Values for n_2 were initially calculated using Equation (4.20) and the power level at which the dual-peak spectral pattern occurs. These values are shown in Figure 4.9 for the TE and TM polarizations. The order of magnitude matches predictions, as does the polarization dependence. However, since the simple model does not account for dispersion, nonlinear absorption, and the nonlinear contribution of the bulk AlGaAs layers, n_2 for as-grown superlattice is significantly underestimated.

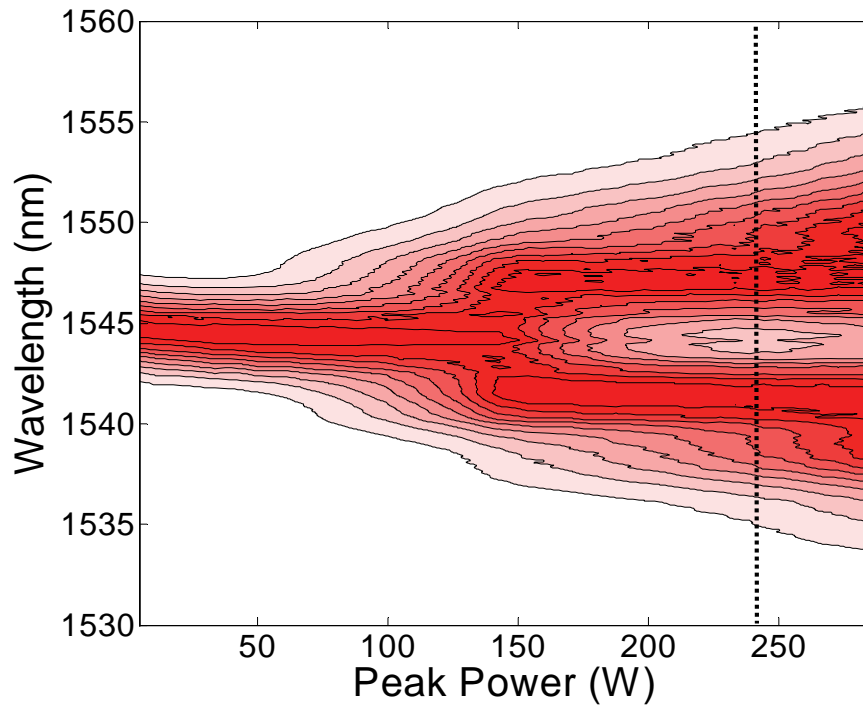
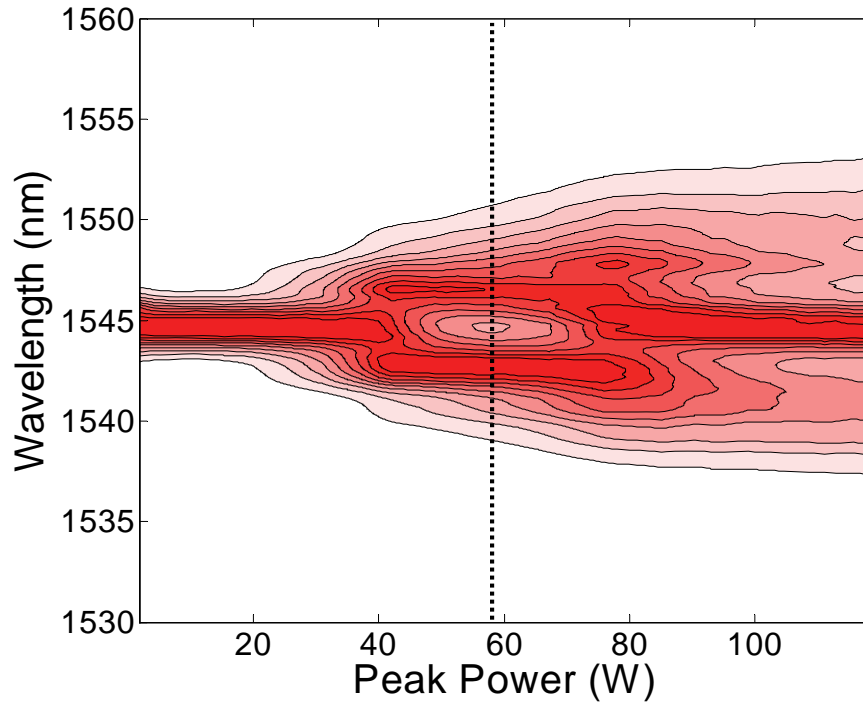


Figure 4.8: Spectral broadening pattern with increasing input power at 1545 nm in as-grown superlattice waveguides for the TE mode (top) and TM mode (bottom)

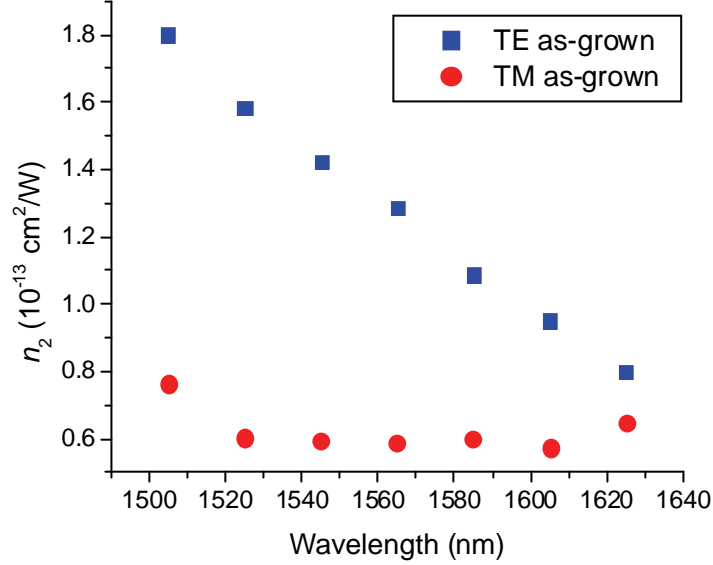


Figure 4.9: Nonlinear refractive coefficients for as-grown superlattice calculated from measured data using the simple modeling method. Values shown underestimate the value of n_2 since dispersion and nonlinear absorption are not accounted for. Thus, n_2 values from the more comprehensive model should be used instead.

Subsequent modeling of spectral broadening was carried out with the use of the GNLSE BPM simulator. Three-photon absorption was previously measured to be nearly nonexistent in as-grown superlattice waveguides, and thus α_3 was set to zero. Third-order dispersion, β_3 , was also set to zero and the self-steepening effect was not accounted for since these phenomena are insignificant for pulse widths greater than 1 ps [3]. Otherwise, all other coefficients in the GNLSE were sourced from values reported in Chapter 2 and Chapter 3.

Effective nonlinear refractive coefficients, $n_{2,eff}$, for as-grown superlattice waveguides were extracted from the experimental data by varying the value of n_2 in the simulator until the dual-peak pattern occurred for the same peak power. Figure 4.10 depicts the evolution of the output spectrum from the simulator for the TE mode at 1545 nm. The simulation results match well to the measured data. Patterns such as the dual-peak point and the single-peak break up point occur at approximately the same power. At each wavelength tested, pulse-widths used in the simulator were varied within the error range of the measured values along with the chirp and the super-Gaussian parameter m to match the initial spectrum of the input pulses. A negative chirp coefficient, C , of between

-1.2 and -1.0 accounted for the formation of spectral side lobes and for the narrow power range over which the spectrum breaks up from a single-peak to a dual-peak. The value of the super-Gaussian parameter m was set between 1.2 and 1.5 to account for the spectral patterns observed at higher input powers. Values of the nonlinear refraction coefficients for the superlattice core layer itself, $n_{2,SL}$, were calculated using the matched $n_{2,eff}$ obtained from the simulator and Equation (4.3) with the calculated values for the effective areas and nonlinear refraction coefficients of the bulk layers.

Nonlinear refraction coefficients for the superlattice core evaluated at wavelengths between 1505 nm and 1625 nm are shown in Figure 4.11. Values were on the order of 10^{-13} cm²/W, which is on the same order as values in bulk Al_{0.18}Ga_{0.82}As [20]. However, nonlinear refraction coefficients in the superlattice show an enhancement over bulk AlGaAs with values being 67% to 200% larger in the TE mode and 19% to 77% larger in the TM mode. This does not agree with theoretical predictions for superlattice in which n_2 was calculated to be less than in bulk AlGaAs [28]. The TE mode shows a rapidly increasing n_2 as the half-bandgap is approached, while the TM mode has

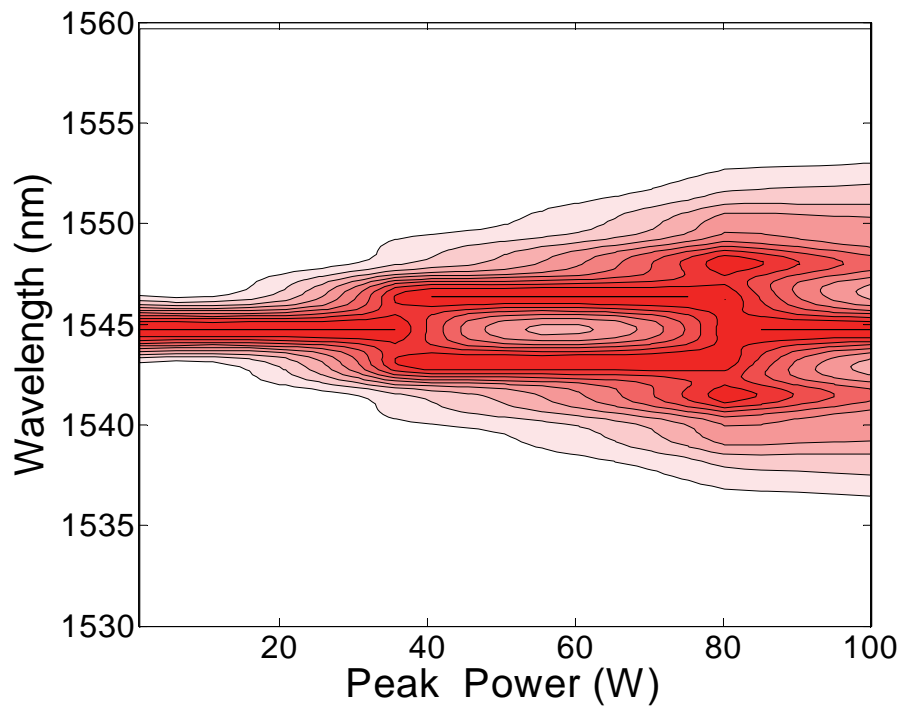


Figure 4.10: Simulated spectral broadening in an as-grown superlattice waveguide for the TE mode at 1545 nm

a relatively flat curve. This indicates that the TE and TM modes have different half-bandgap resonance points. As a result, a large polarization dependence in n_2 occurs near the half-bandgap where the TE mode exhibits n_2 values that are two-times larger than the TM mode. This observed polarization dependence does agree with predictions from Hutchings [28]. By comparison, bulk AlGaAs only shows a polarization dependence of 10% at most. The enhancement in the polarization dependence and the strength of the Kerr effect is similar to that seen in GaAs/AlGaAs MQW waveguides [49, 58]. At longer wavelengths, the polarization dependence in superlattice is reduced with TE and TM values becoming nearly the same beyond 1605 nm.

Uncertainty in the measured values results from many sources listed in Table 4.2. Error in the third-order core effective area was up to 14% in the TE mode and 9% in the TM mode. Linear loss coefficients had errors of up to 16% that contributed less than 1% error in the value of n_2 . Errors of 6% in the autocorrelation measurements of the pulse width added an error of the same amount to the nonlinear coefficients. The effective index of refraction introduced errors that were less than 1% and thus were ignored. Uncertainty in the scaled values of n_2 for the buffer and cladding layers was 12%. In

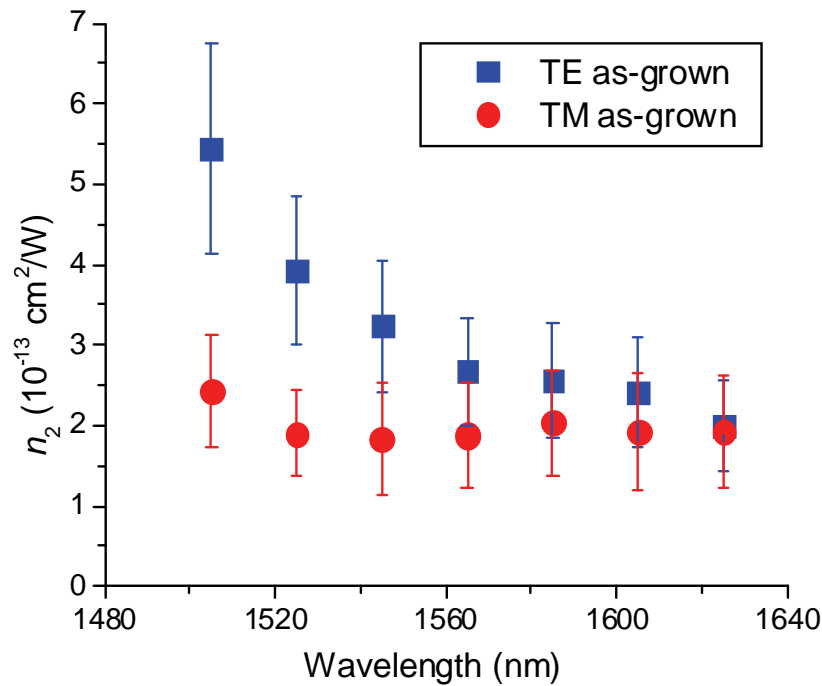


Figure 4.11: Measured nonlinear refraction coefficients for SPM in as-grown superlattice produced by numerical solutions to the GNLSE

Table 4.2: Sources of error in n_2 for as-grown superlattice

Error Source	TE	TM
$A_{eff}^{(3)}$	14%	9%
α_0	<1%	<1%
t_0	6%	6%
n_0	<1%	<1%
Buffer/cladding n_2	12%	12%
TOTAL	32%	27%

total, the error in the measured n_2 was at most 32% in the TE mode and 27% in the TM mode.

4.2.8 Results for Intermixed Superlattice

Preliminary experiments with intermixed superlattice waveguides were carried out with the laser system in picosecond mode. However, very little spectral broadening was observed at the waveguide output. This result was due to higher linear losses in the waveguides that limited the amount of power available to induce the Kerr effect. Furthermore, the short length of the sample reduced the interaction length over which SPM could take place.

In subsequent experiments, the laser was configured into femtosecond mode. This gave enough peak power to produce an observable amount of spectral broadening however at the expense of spectral resolution. The wavelength was swept from 1400 nm to 1600 nm at intervals of 50 nm. However, beyond 1450 nm, the collected data did not clearly show discernable spectral broadening patterns. It is possible that other effects such as high order dispersion and forms of nonlinear absorption other than 3PA and TPA were modifying the spectral evolution in ways that are difficult to predict.

The data at 1450 nm was decent for both polarizations and the simulator reasonably replicated the observed spectral broadening patterns. The intermixed core layer was assumed to have a similar nonlinearity to the buffer and cladding layers because of the similarity in the bandgap energy. This allowed the use of waveguide effective areas which were calculated as $7.84 \mu\text{m}^2$ for the TE mode and $8.11 \mu\text{m}^2$ for the

Table 4.3: Sources of error in n_2 for intermixed superlattice

Error Source	TE	TM
$A_{eff}^{(3)}$	12%	8%
α_0	32%	85%
t_0	6%	6%
Matched n_2	3%	5%
TOTAL	53%	104%

TM mode at 1450 nm. Measured values of 3PA were included in the simulations resulting in power limiting at large powers. From the matched spectral broadening simulations, the TE mode had an n_2 of 0.42 cm²/W and the TM mode had an n_2 of 0.205 cm²/W. This is nearly an order of magnitude smaller than the values for as-grown superlattice at longer wavelengths. Since the value of n_2 should become smaller at longer wavelengths, intermixing the superlattice reduced the nonlinearity of the material. Thus, relative to as-grown material, intermixed superlattice can be considered as being linear.

The error in the measured values at 1450 nm was large because of the high linear loss coefficients. For the TE mode, error due to the linear loss was estimated to be about 32%. For the TM mode, this error was much higher at about 85%. Errors in the effective areas were 8% in the TM mode and 12% in the TE mode. Uncertainty in the measured pulse width was 6%. Variation in the matched value of n_2 was 5% in the TM mode and 3% in the TE mode. Total errors were 104% for TM and 53% for TE, as shown in Table 4.3.

4.3 Cross-phase Modulation in As-grown Superlattice

4.3.1 Theory

Two orthogonally-polarized beams of light co-propagating through a nonlinear medium can interact by the Kerr effect. Effectively, each beam experiences a change in the refractive index induced by the other according to

$$\Delta n_{TE} = n_{X2, TM} I_{TM} \quad (4.28)$$

$$\Delta n_{TM} = n_{X2,TE} I_{TE} \quad (4.29)$$

where $n_{X2,TE}$ and $n_{X2,TM}$ are the cross-Kerr coefficients for the TE and TM polarizations respectively. As with other nonlinear effects in a waveguide, the total change in the refractive index due to XPM is the sum of the contributions from each material in the structure. Furthermore, the total phase change in the each polarization will be the sum of the phase changes originating from both SPM and XPM. For a pulse, the phase change varies with time and causes a shift in the optical frequency. Thus, XPM causes spectral broadening in the same way SPM does. The pattern of the spectral changes is susceptible to the same phenomena such as pulse shape, chirp, dispersion, and nonlinear absorption.

The phase changes and spectral broadening caused by XPM between two co-propagating polarizations will be strongly affected by birefringence in the medium or waveguide. Birefringence causes each polarization to propagate at a different speed. In the case of a pulse, each polarization will have a different group velocity. Thus, as the pulses move through the waveguide, one of the pulses will begin to lag the other as is shown in Figure 4.12. In this case, the peaks of the pulses are no longer coincidental. The leading pulse acts mostly on the head of the trailing pulse and the trailing pulse acts mostly on the tail of the leading pulse. Thus, the leading pulse will cause a blue shift in the trailing pulse and the trailing pulse will cause a red shift in the leading pulse. As a result, group velocity mismatch between the pulses causes the spectra of each to broaden

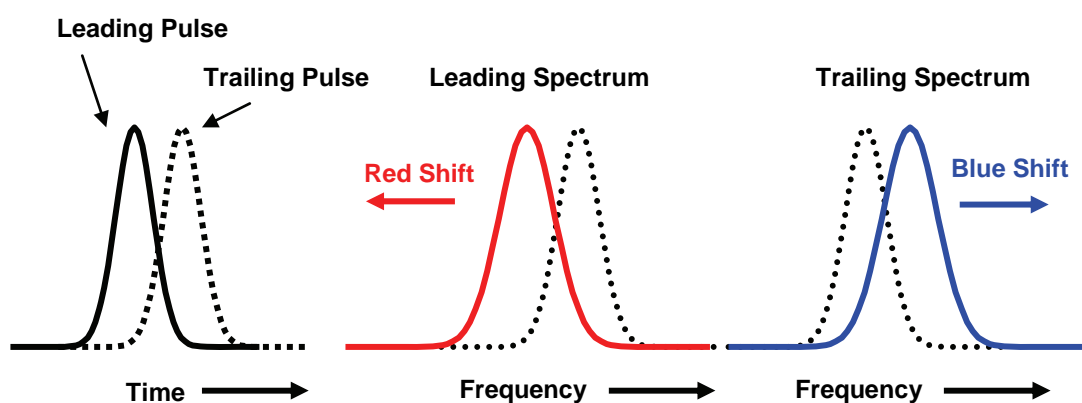


Figure 4.12: XPM-induced frequency shifts on co-propagating pulses shifted from each other in time by group velocity mismatch

asymmetrically. Initial pulse chirp can either enhance or suppress this asymmetry depending on whether it is negative or positive.

Accurate modeling of the interaction between two co-propagating pulses requires inclusion group velocity in addition to the parameters that affect SPM. The GNLSE of Equation (4.12) can be extended to give a pair of coupled equations expressed as [3, 53]

$$\begin{aligned} j \frac{\partial A_e}{\partial z} + j \frac{\alpha_{0,e}}{2} A_e + j \frac{\alpha_{2,e}}{2} \frac{|A_e|^2}{A_{eff,e}^{(3)}} A_e + j \frac{1}{v_{g,e}} \frac{\partial A_e}{\partial t} - \frac{\beta_{2,e}}{2} \frac{\partial^2 A_e}{\partial t^2} \\ + \frac{2\pi}{\lambda} \left(\frac{n_{2,e}}{A_{eff,e}^{(3)}} |A_e|^2 + \frac{n_{X2,m}}{A_{eff,m}^{(3)}} |A_m|^2 \right) A_e = 0 \end{aligned} \quad (4.30)$$

$$\begin{aligned} j \frac{\partial A_m}{\partial z} + j \frac{\alpha_{0,m}}{2} A_m + j \frac{\alpha_{2,m}}{2} \frac{|A_m|^2}{A_{eff,m}^{(3)}} A_m + j \frac{1}{v_{g,m}} \frac{\partial A_m}{\partial t} - \frac{\beta_{2,m}}{2} \frac{\partial^2 A_m}{\partial t^2} \\ + \frac{2\pi}{\lambda} \left(\frac{n_{2,m}}{A_{eff,m}^{(3)}} |A_m|^2 + \frac{n_{X2,e}}{A_{eff,e}^{(3)}} |A_e|^2 \right) A_m = 0 \end{aligned} \quad (4.31)$$

where the subscripts “*e*” and “*m*” refer to variables and coefficients related to the TE and TM mode respectively. Third-order dispersion, 3PA, and the self-steepening effect were not included in these equations for simplicity. Four-wave mixing terms have also been omitted under the assumption that the phase matching does not occur between the polarizations due to birefringence [3]. The group velocity is included in the terms involving $v_{g,e}$ and $v_{g,m}$. XPM is accounted for in the last terms of each equation. Note that these terms involve the intensity of the other field, and hence the reason for the appearance of the $A_{eff}^{(3)}$ value for the orthogonal polarization. In the past literature, the strength of XPM was expressed as in the ratio of XPM-to-SPM [3, 53]. Here, separate nonlinear coefficients for XPM and SPM have been used. Thus, that ratio is defined as $(\text{XPM/SPM})_e = n_{2,e}/n_{X2,e}$ for the TE polarization and $(\text{XPM/SPM})_m = n_{2,m}/n_{X2,m}$ for the TM polarization.

4.3.2 Previous Studies of XPM in Semiconductors

Very few studies have been carried out to characterize XPM between polarizations in semiconductor materials. However, the few that have been done are relevant to the material examined in this thesis. XPM was studied in bulk $\text{Al}_{0.18}\text{Ga}_{0.82}\text{As}$ waveguides by Aitchison *et al.* [20]. By numerically fitting spectral broadening measurements of the probe beam, the ratio SPM-to-XPM was determined to be about 0.94. This ratio remained nearly the same across the studied spectrum just below the half-bandgap. Also, no consistent polarization dependence of this ratio was observed. A study of the XPM-to-SPM ratio in GaAs/AlGaAs MQW waveguides was carried out by Villeneuve *et al.* [71]. Waveguides consisted of a MQW core layer with 3 nm-thick GaAs wells separated by 20 nm-thick AlGaAs barriers. At a wavelength of 1555 nm, a TM polarized pump was found to give a ratio of unity. However, a TE polarized pump gave a ratio of 0.5. This polarization dependence was attributed to exciton interactions that affect the TM mode and not the TE mode.

4.3.3 Theoretical Predictions for Superlattice

The break down of symmetry in superlattice leads to differences in the nonlinear susceptibility tensor elements related to XPM. Of the eight independent, non-zero tensor elements of the third-order nonlinear susceptibility, two are related to XPM: $\chi_{xzx}^{(3)}$ for the TE polarization, and $\chi_{zxx}^{(3)}$ for the TM polarization. Theoretical values for these tensor elements related to XPM in superlattice were calculated by Hutchings [28]. Using Equation (4.20) with an additional factor of 2 that results in the derivation of the propagation equations [3, 28], the value of n_{χ_2} was calculated for the TE and TM modes. As Figure 4.13 shows, there is a polarization dependence with the TE mode having n_{χ_2} values that are between 38% and 73% of the value for the TM mode. The predicted ratio of XPM/SPM was also calculated using theoretical n_2 values discussed in Section 4.2.4 and is shown in Figure 4.14. In the TE polarization, the ratio is about 0.79 ± 0.06 while in the TM polarization, XPM/SPM is about 1.35 ± 0.53 .

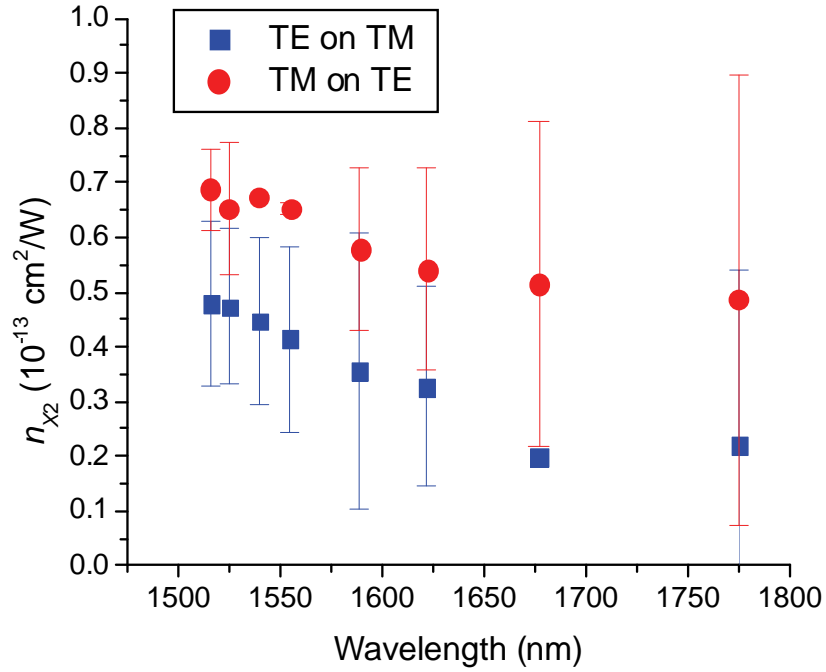


Figure 4.13: Theoretical n_{x2} values for as-grown superlattice calculated from Ref. [28]

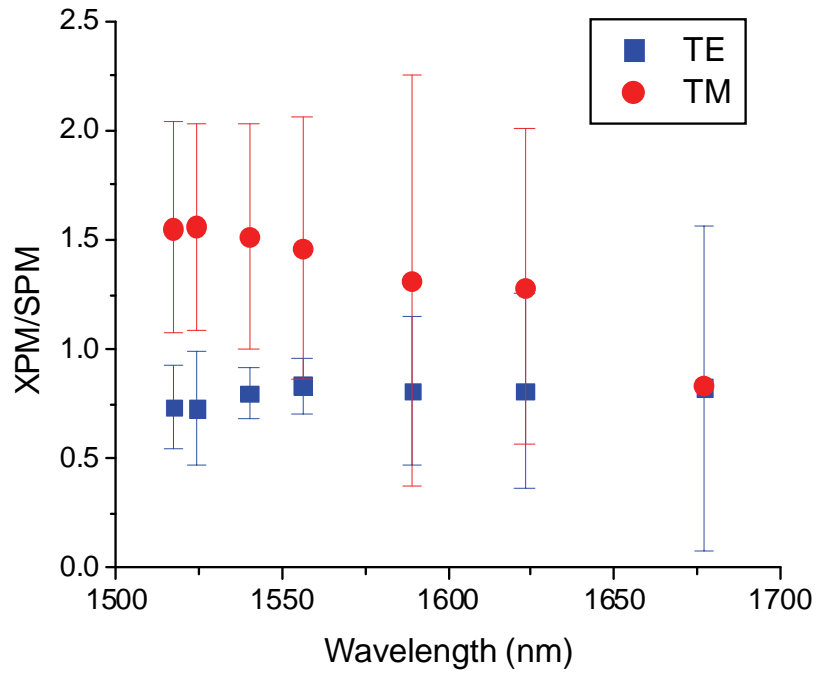


Figure 4.14: Theoretical XPM/SPM ratios for as-grown superlattice calculated from Ref. [28]

4.3.4 Experimental Methods

Measurement of XPM was carried out by using the same experimental setup as SPM experiments with the laser set in picosecond mode. The half-waveplate located just before the end-fire rig was set to give a mixed TE/TM polarization such that one of the composing polarizations was a strong pump signal and the other polarization was a weak probe signal. In all experiments, the probe signal power was set to be no more than 7% of the pump to limit the amount of SPM in the probe. A polarizing beam cube was added just after the output objective of the end-fire rig to isolate the probe polarization before detection at the output power meter and the OSA. The output spectrum of the probe was observed at increasing input pump power levels.

The GNLSE BPM code was modified to simulate the propagation of two beams with XPM. To maintain a consistent time reference point of zero, Equations (4.30) and (4.31) were modified as [3]

$$\begin{aligned} j \frac{\partial A_{pm}}{\partial z} + j \frac{\alpha_{0,pm}}{2} A_{pm} + j \frac{\alpha_{2,pm}}{2} \frac{|A_{pm}|^2}{A_{eff,pm}^{(3)}} A_{pm} - \frac{\beta_{2,pm}}{2} \frac{\partial^2 A_{pm}}{\partial t^2} \\ + \frac{2\pi}{\lambda} \left(\frac{n_{2,pm}}{A_{eff,pm}^{(3)}} |A_{pm}|^2 + \frac{n_{X2,pb}}{A_{eff,pb}^{(3)}} |A_{pb}|^2 \right) A_{pm} = 0 \end{aligned} \quad (4.32)$$

$$\begin{aligned} j \frac{\partial A_{pb}}{\partial z} + j \frac{\alpha_{0,pb}}{2} A_{pb} + j \frac{\alpha_{2,pb}}{2} \frac{|A_{pb}|^2}{A_{eff,pb}^{(3)}} A_{pb} + jd \frac{\partial A_{pb}}{\partial t} - \frac{\beta_{2,pb}}{2} \frac{\partial^2 A_{pb}}{\partial t^2} \\ + \frac{2\pi}{\lambda} \left(\frac{n_{2,pb}}{A_{eff,pb}^{(3)}} |A_{pb}|^2 + \frac{n_{X2,pm}}{A_{eff,pm}^{(3)}} |A_{pm}|^2 \right) A_{pb} = 0 \end{aligned} \quad (4.33)$$

where the subscripts “*pm*” and “*pb*” denote variables and coefficients related to the pump and probe polarizations respectively, and *d* is the group velocity mismatch parameter which is defined as

$$d = \frac{v_{g,pm} - v_{g,pb}}{v_{g,pm} v_{g,pb}}. \quad (4.34)$$

Thus, the pump was held at a time of zero while the probe was allowed to move past the probe in time. The MATLAB code of the modified BPM simulator is detailed in Appendix B.

4.3.5 Measured Results

Spectral broadening induced by XPM was measured for the TM pump \rightarrow TE probe interaction and the TE pump \rightarrow TM probe interaction. The measured spectral evolution of the probe with input pump power is shown in Figure 4.15 for the TM pump \rightarrow TE probe interaction at 1545 nm. A significant asymmetry in the spectrum is clear at large powers, which indicates the effect of a group velocity mismatch. Most of the power ended up shifting to shorter wavelengths and the entire spectrum was gradually blue shifting. This indicates that the TM pump was leading the TE probe, which was expected since the group velocity of the TM mode was calculated to be higher than the group velocity of the TE mode.

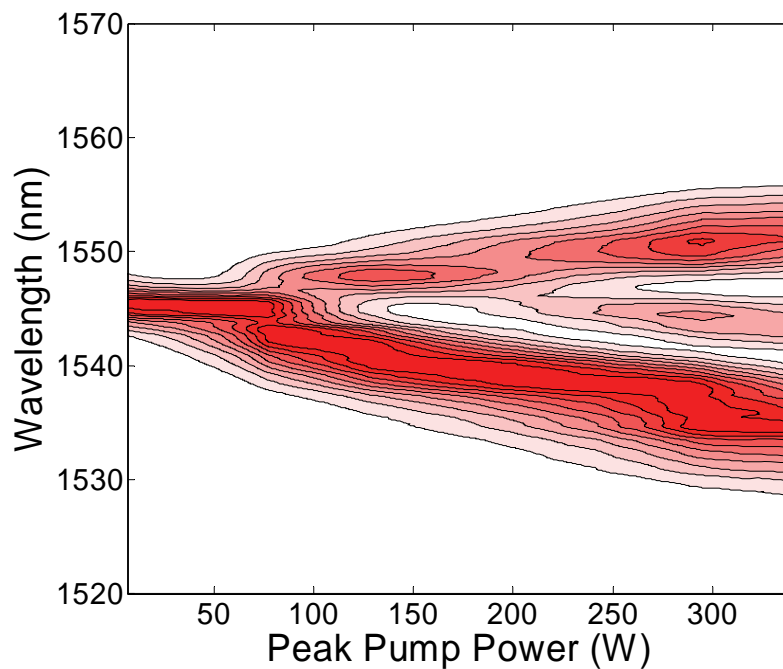


Figure 4.15: Measured XPM-induced spectral broadening on a TE probe by a TM pump at a wavelength of 1545 nm

The XPM-induced spectral broadening was modeled using the modified GNLSE BPM simulator. The group velocity mismatch parameter, d , was obtained from group velocity values calculated in Section 2.5.3. To obtain good matches to the observed asymmetry, d was varied within 10% of the calculated value. The chirp values used varied between -0.4 and 0.3, and the super-Gaussian parameter varied between 1.0 and 1.2. The beat length between the two polarizations was shown in Section 2.5.3 to be much less than the propagation length and thus four-wave mixing is negligible because of the large resulting phase mismatch [3]. Simulated spectral broadening of a 1545 nm TE probe is shown in Figure 4.16 and matches well with experimental data. Furthermore, the simulation confirms that group velocity mismatch is the dominant mechanism for causing asymmetric spectral broadening.

As with SPM, the simulator produces effective n_{χ_2} values for the waveguide as a whole. In order to extract the n_{χ_2} values for the superlattice core, it was necessary to account for the effect of the cladding layers. Since the XPM/SPM ratio for bulk AlGaAs was found to be unity [20], n_2 values for $\text{Al}_{0.56}\text{Ga}_{0.44}\text{As}$ calculated in Section 4.2.3 were

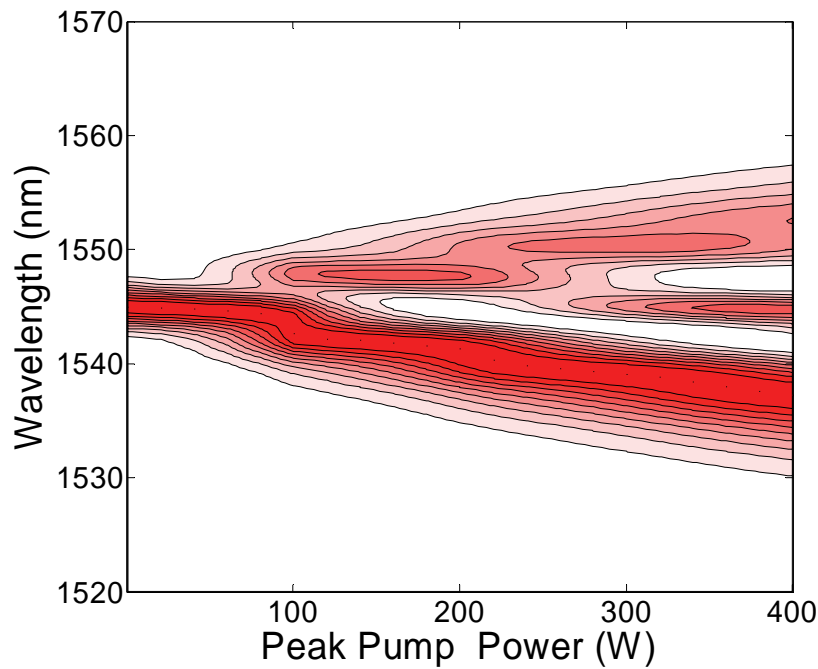


Figure 4.16: Simulated XPM-induced spectral broadening of TE probe acted on by TM pump for as-grown superlattice at 1545 nm

used as n_{X2} values for the buffer and cladding layers. Thus, by using Equation (4.3), the values for $n_{X2,SL}$ were calculated. As shown in Figure 4.17, the TE pump shows an increasing value of n_{X2} as the wavelength is decreased toward the half-bandgap while the value of n_{X2} for the TM pump remains somewhat flat. The two curves cross at around 1545 nm with XPM being larger for the TE pump at shorter wavelengths and larger for the TM pump at longer wavelengths. These results do not agree with the theoretical values for n_{X2} which were predicted to be consistently high in the TM pump case. However, note that the error bars do overlap on some of the points. The uncertainty in the values shown come from the same sources and has the same magnitudes as those used for SPM n_2 values, except that an additional error of up to 10% has been added due to an increased uncertainty in the match between simulation results and measured data.

The ratio of XPM to SPM was calculated using the measured n_{X2} values of Figure 4.17 and the measured values of n_2 from Section 4.2.7. As shown in Figure 4.18, the TM mode has a consistently higher ratio than the TE mode. This general trend matches the predicted ratios and previous studies on GaAs/AlGaAs MQW waveguides [71]. However, the ratios for both modes are lower than expected and both below unity. For

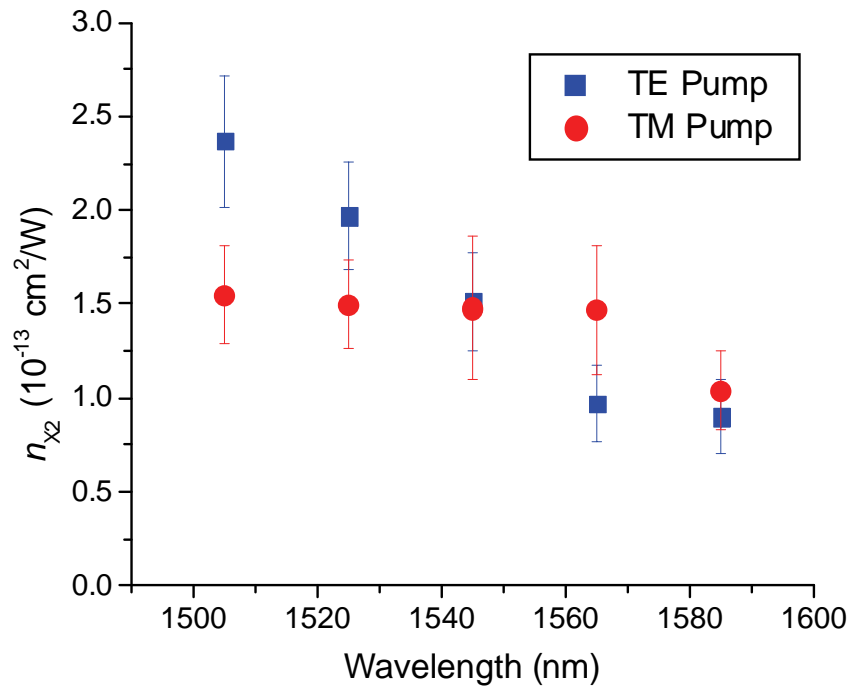


Figure 4.17: Measured nonlinear refraction coefficients for XPM in as-grown superlattice

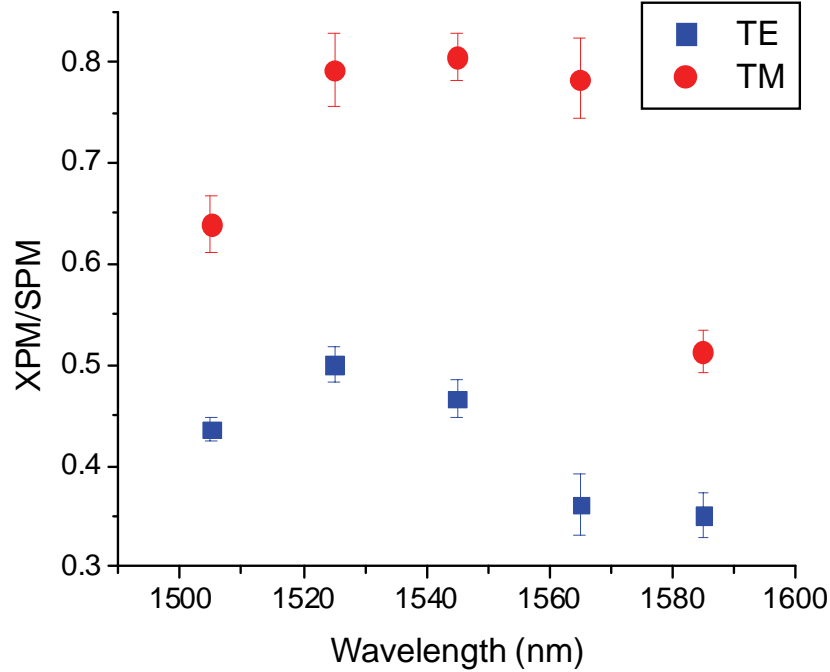


Figure 4.18: Measured XPM/SPM ratios for as-grown superlattice

the TE mode, XPM/SPM is about 0.42 ± 0.08 while the TM mode has a ratio of about 0.71 ± 0.19 . Compared to MQWs, the TE mode shows a similar ratio of near 0.50, but the TM mode falls far below the ratio of 1.0 previously observed. Error bars shown account for the error of up to 10% in value of n_{x2} when obtaining matches between simulations and experiments.

4.4 Conclusions

This chapter examined nonlinear refraction by SPM and XPM in as-grown and intermixed superlattice waveguides. Spectral broadening was found to be affected by pulse shape, pulse chirp, dispersion, and nonlinear absorption. Calculations of the nonlinear refraction coefficients for bulk AlGaAs using scaling laws revealed that the buffer and cladding layers contribute significantly to nonlinear refraction in the waveguide and must be accounted for when calculating n_2 for the superlattice core. The contribution of the indirect bandgap of the bulk AlGaAs layers to nonlinear refraction was calculated to be more than two-orders of magnitude smaller than the direct gap contribution and was thus ignored. Simple models of the propagation of a pulse in a

nonlinear medium were found to be inaccurate and thus a more comprehensive model involving the GNLSE was required. Solving the GNLSE was done by computer BPM simulations that employed the split-step Fourier method. Experimental data was matched to the computer simulations to yield more accurate n_2 values. In as-grown superlattice, n_2 was found to be polarization dependent with the TE mode having larger coefficients than the TM mode at wavelengths close to the half-bandgap, which agreed with the predicted anisotropy. Nonlinear refraction was also found to be enhanced over bulk AlGaAs, which is similar to previous results in MQW waveguides. The rapid increase of the TE mode coefficients as the half-bandgap was approached and the relative flatness of the TM mode curve indicate a difference in the resonance points for the TE and TM modes. The large values for n_2 indicate that superlattice has sufficient nonlinearity to realize practical devices. Measurements of intermixed superlattice revealed a reduction in n_2 of over one-order of magnitude relative to as-grown superlattice, thus showing that intermixing suppresses the nonlinear behaviour.

XPM in as-grown superlattice waveguides was examined theoretically and experimentally. Group velocity mismatch has a large impact on XPM-induced spectral broadening and thus it was necessary to modify the GNLSE and the BPM simulator to account for it. Experiments employed a pump-probe setup in which a strong pump on one polarization acted on a weak probe on the other polarization. Resulting n_{χ_2} values showed that XPM increases for the TE mode as the half-bandgap is approached while the TM mode remains somewhat featureless. XPM-to-SPM ratios were larger in the TM mode, which agrees with predictions. The ratio for the TE mode agreed with previous studies of MQW waveguides.

Chapter 5

Applications of Superlattice to Nonlinear Optical Signal Processing Devices

5.1 Introduction

One of the applications of nonlinear optics is in creating all-optical signal processing devices. The Kerr effect enables several phenomena such as self-phase modulation and cross-phase modulation that create phase changes in optical signals to allow optical switching. However, nonlinear absorption has a negative impact on these effects and must be accounted for when designing devices. Quantum well intermixing may add benefits to device design and its application to all-optical switching should be explored.

In this chapter, the application of superlattice waveguides to all-optical signal processing is examined. A figure of merit is calculated to evaluate the effect of TPA on the optical Kerr effect for some types of all-optical devices. The power requirements to cause switching in a nonlinear directional coupler (NLDC) are discussed for superlattice and other semiconductors. A design for a nonlinear Mach-Zehnder interferometer (NLMZI) is examined and the possible benefits of using superlattice for this device are discussed.

5.2 Figure of Merit

To design practical all-optical switching devices based on the Kerr effect, it is necessary to determine the amount of phase shift that can be achieved in a material. This will depend mostly on the strength of nonlinear refraction, the amount of power that can be delivered to the device, and the level of optical confinement in the waveguide. However, losses in a waveguide limit the effectiveness of the Kerr effect by reducing the power available to induce phase changes. Thus, it is necessary to account for linear and nonlinear loss when evaluating a nonlinear material.

In the case where linear losses and 3PA are low, TPA will be the dominate loss mechanism at the large power levels required to gain large phase shifts by nonlinear refraction. A simple figure of merit (FOM) was developed by Mizrahi *et al.* to weigh the effects of TPA on nonlinear refraction [10]:

$$T = \frac{2\alpha_2\lambda}{n_2}. \quad (5.1)$$

In general, lower values of T are desirable to give the greatest amount of phase shift without being limited by TPA. The larger the phase shift required, the lower T must be to realize a practical device.

The value of T was calculated for as-grown superlattice using Equation (5.1), the value of α_2 from Section 3.2.6, and the measured n_2 from Section 4.2.7. As shown in Figure 5.1, the FOM is different for each polarization with the TE mode tending to have a larger value of T than the TM mode. At wavelength of 1545 nm and 1565 nm, T is nearly the same for both polarizations, which indicates that these are the most optimal wavelengths to work at for a polarization independent device. Otherwise, the most optimal device operation can be realized by using the TM mode at shorter wavelengths. In this case, a device operating at these wavelengths would be very polarization dependent with the TE mode having an FOM that is 64% larger than the TM mode.

To evaluate superlattice as a nonlinear material relative to other materials, the FOM for other semiconductors was calculated using published values for n_2 and α_2 . The listings in Table 5.1 show data for wavelengths near 1550 nm. Bulk AlGaAs clearly has

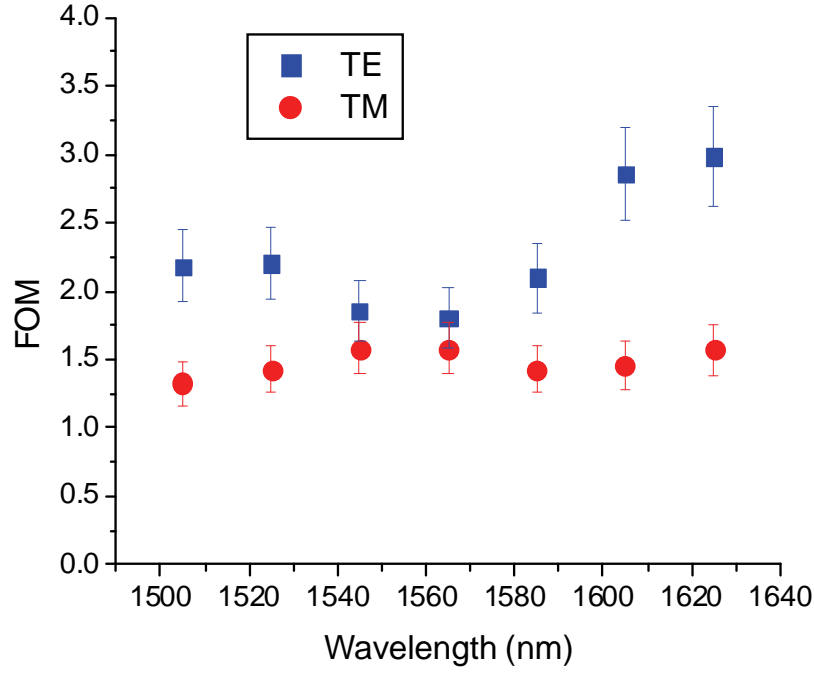


Figure 5.1: TPA Figure of merit for as-grown superlattice

Table 5.1: Figures of merit T in various semiconductors for TPA-dominated loss

		λ (nm)	n_2 ($\times 10^{-13} \text{ cm}^2/\text{W}$)	α_2 (cm/GW)	T	Source
GaAs/AlAs Superlattice	TE	1545	3.24	1.94	1.8	
	TM		1.84	0.94	1.6	
Bulk $\text{Al}_{0.18}\text{Ga}_{0.82}\text{As}$	TE	1556	1.50	0.1	0.2	[20]
	TM		1.43	~ 0	~ 0	
GaAs/AlGaAs MQW	TE	~ 1550	~ 2.8	5.5	6.1	[58]
	TM		~ 1.6	~ 1.6	3.1	
Bulk GaAs		1540	1.59	10.2	19.8	[54]
c-Si		1540	0.45	0.79	5.4	[54]

the best figure of merit with values that are much less than one. Superlattice is much higher with the value of T being about nine-times larger than AlGaAs in the TE mode. However, crystalline silicon, GaAs, and GaAs/AlGaAs MQWs all have worse figures of merit than either superlattice or bulk AlGaAs. For MQWs, this is due in part to the exciton resonances that raise the amount of TPA disproportionately to n_2 . In the case of

silicon and GaAs, wavelengths around 1550 nm fall above the half-bandgap where TPA is large. Thus, compared to other semiconductors, superlattice does well as a nonlinear material.

5.3 Nonlinear Directional Coupler

The directional coupler is a commonly used device in various applications. As shown in Figure 5.2, it consists of a pair of waveguides that are brought close together [72]. In this coupling region, the evanescent fields of the waveguide modes overlap. Thus over some distance, the light in one waveguide will couple to the other. In the case that light enters at the point IN, some percentage of the light will exit at the CROSS output while the rest of the light leaves at the BAR port. The ratio of CROSS-to-BAR power depends on the length of the coupling region and on the propagation constants of each waveguide. In a half-beat directional coupler, the length of the coupling region is such that all of the power entering the IN port couples to the other waveguide and leaves at the CROSS port.

The behaviour of a directional coupler changes as a function of intensity if the material used is sufficiently nonlinear. At large input powers, the Kerr effect causes a change in the effective refractive index of the waveguide in which the light is propagating. This leads to a change in the propagation constant and a change in the amount of light that couples to the other waveguide. At some power level, no power will couple and all of the light exits through the BAR port instead of the CROSS port. Thus, this device switches light to either the CROSS port or the BAR port depending on the input intensity. Such a device is known as a nonlinear directional coupler [73]. NLDCs

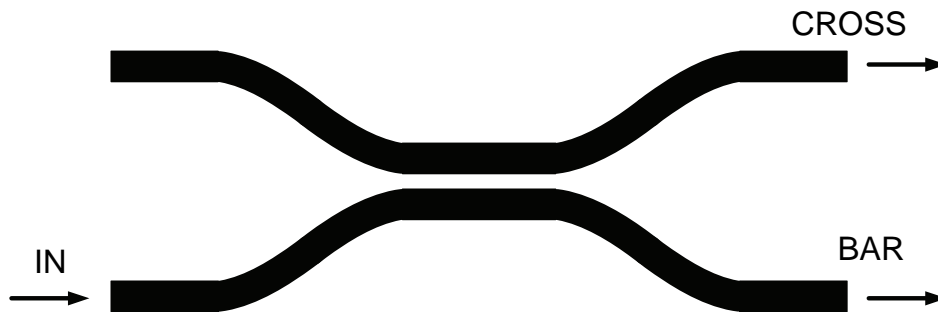


Figure 5.2: Schematic of a directional coupler

have already been implemented in bulk AlGaAs [74] and in GaAs/AlGaAs MQW waveguides [75].

Nonlinear absorption will significantly affect behaviour and performance of an NLDC. The effect of TPA was studied in detail by DeLong *et al.* [76]. The power at which the power split in a half-beat NLDC is 50:50 was defined as the critical power

$$P_C = \frac{2\pi A_{eff}^{(3)}}{k_0 n_2 L} \quad (5.2)$$

where k_0 is the free-space propagation constant and L is the coupler length. By using the figure of merit definition of Equation (5.1), Figure 5.3 shows the effect of TPA on the switching characteristics of a NLDC. The input power is shown relative to the critical power. In the case where TPA is not present ($T=0$), almost all of the power exits at the BAR port for a power level just above P_C . However, as the figure of merit increases, the amount of power required to cause switching increases. At $T=4$, the NLDC no longer operates effectively as a switch since the largest achievable switching fraction is <0.9 which requires more than three-times more power than P_C .

By using the figures of merit calculated in Section 5.2, the usefulness of superlattice as a material for creating NLDCs can be compared to other nonlinear materials for wavelengths near 1550 nm. Shown in Figure 5.4 are the necessary powers required to reach the maximum switching ratio as a function of the figure of merit. Bulk

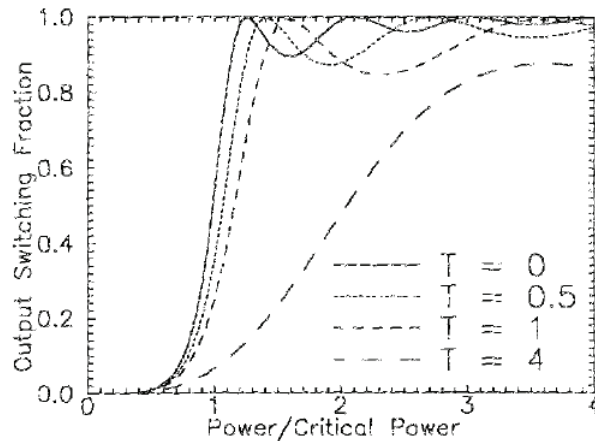


Figure 5.3: Output switching fraction versus input power for an NLDC with different T values [76]

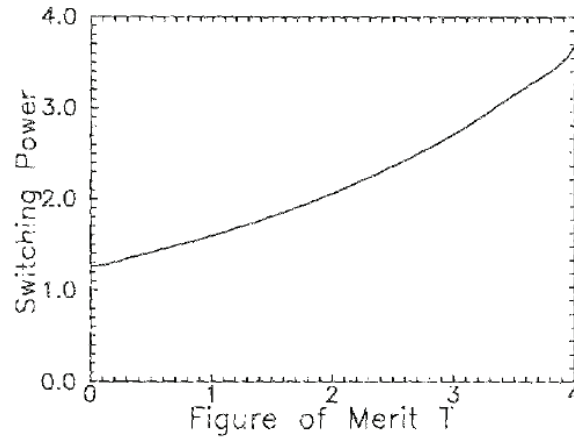


Figure 5.4: Required switching power versus figure of merit for a NLDC [76]

AlGaAs clearly has the best performance by requiring only $\sim 1.3P_C$ to cause switching. Superlattice requires $\sim 1.95P_C$ in the TE mode and $\sim 1.8P_C$ in the TM mode. Thus, between 40%-50% more power is required for superlattice compared to bulk AlGaAs. The next best performing material is GaAs/AlGaAs MQW which has a switching power $\sim 2.95P_C$ in the TM mode. In all other cases, the required switching power is more than double than that required for superlattice.

5.4 Nonlinear Mach-Zehnder Interferometer

Mach-Zehnder interferometers are another type of device that is commonly used in telecommunications systems. As shown in Figure 5.5, power input to the MZI is split into two arms, one of which has a phase shifting element. Depending upon the amount of phase shift accumulated in the phase shifter, the beams in the two arms recombine at the output either constructively or destructively. In electro-optic modulators, the phase shifter operates by the electro-optic effect controlled by electronics. For all-optical switching, the phase shifter relies on the optical Kerr effect to cause an intensity-dependent phase shift [77]. In either case, the phase shift must be an odd multiple of π in order to cause completely destructive interference at the output. This is much smaller than the 4π phase shift required for an NLDC. Thus, an NLMZI may be more practical as an all-optical switching device.

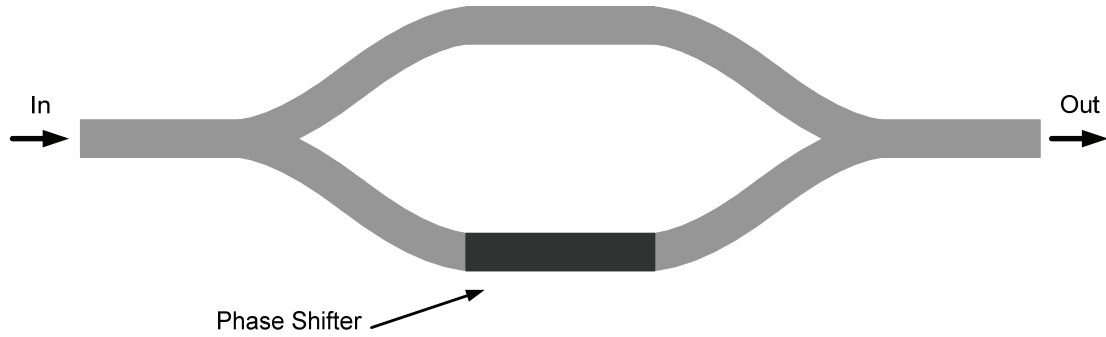


Figure 5.5: Schematic of a Mach-Zehnder interferometer

The design of a NLMZI is complicated by the use of materials with a uniform nonlinearity. However, a few methods to overcome this limitation have been proposed and implemented. Stegeman and Wright proposed the idea of increasing the optical intensity in one arm by reducing the waveguide cross section, which decreases the effective mode area [77]. Thus, the phase shifting arm experiences a larger nonlinear phase shift relative to the reference arm of the same length. In the case where the effective area of the phase shifting arms is half the effective area of the reference, the required phase shift is 2π since the reference arm gives a phase shift of π . However, this scheme is complicated by the difficulty in making single-mode waveguides that have double the effective area of the phase shifter waveguide [77]. In another design by Alhemyari *et al.*, the power was split asymmetrically between the two arms of the NLMZI [78]. Thus, one arm experiences a larger nonlinear phase shift than the other. A switching fraction of nearly 80% was achieved using 330 fs pulses with ~ 8.5 mW of average input power.

Quantum well intermixing opens the opportunity for creating a simplified NLMZI structure in MQW and superlattice waveguides. In one design by Kan'an *et al.*, one arm of the NLMZI is made of as-grown material while the other arm is made up of intermixed material [79]. Since the intermixed material has a reduced nonlinearity, the intermixed waveguide acts as the reference arm. This design was implemented by Kan'an *et al.* in a GaAs/AlGaAs MQW structure in which intermixed regions were created by silica-cap IFVD. A switching contrast ratio of 7:1 was achieved with 150 fs pulses. However, the PL shift of the intermixed material was measured to be only about 37 nm. In a previous study of intermixing MQWs, a shift of ~ 40 nm in the PL peak resulted only in 60%

reduction of the nonlinear refraction coefficient [66]. Thus, it is assumed that the nonlinearity of the intermixed regions was only reduced by this amount. Furthermore, the device was tested at wavelengths near the bandgap where TPA is expected to be high.

GaAs/AlAs superlattice offers several advantages over MQWs. The PL shift was shown to be about 150 nm after intermixing, which is over three-times larger than what has been achieved in MQW [66]. The nonlinear coefficients of intermixed superlattice were over an order of magnitude smaller than as-grown superlattice, which is nearly double the change in MQW. Thus, the phase shift in the as-grown arm does not need to overcome as much nonlinear phase in the reference arm. Intermixed waveguides could also be used as the input and output waveguides to avoid large amounts of nonlinear absorption and spectral broadening before the light encounters the nonlinear elements of the device. Also, the effect of TPA in as-grown superlattice was shown to be less as it has a lower figure of merit than MQW. Thus, superlattice may provide a performance enhancement and enable shorter NLMZIs when compared with other materials.

5.5 Conclusions

In this chapter, superlattice was evaluated as a material for creating all-optical signal processing devices. The figure of merit T was calculated to give a measure of the effect that TPA has on Kerr effect-induced phase shifts. Superlattice had values of T that were above 1 with the TE mode generally having larger values than the TM mode. The optimal operating wavelengths were between 1545 nm and 1565 nm for polarization independent operation while the lowest value of T was found in the TM mode at 1505 nm. With the exception of bulk AlGaAs, superlattice has a lower figure of merit than other semiconductors. NLDCs made of superlattice require up to 50% more power over AlGaAs in order to cause switching, but require less than half the power of other semiconductors. For a NLMZI, superlattice may enable shorter devices than MQW waveguides since intermixing superlattice causes a larger change in the nonlinear coefficients which makes it better as a material for the reference arm. Furthermore, intermixed waveguides could be used as linear input and output waveguides for nonlinear devices.

Chapter 6

Conclusions

6.1 Summary

This thesis has examined the linear and nonlinear properties of 14:14 GaAs/AlAs superlattice waveguides at wavelengths below the half-bandgap. It was necessary to examine the linear properties first followed by the nonlinear absorption coefficients in order to accurately model and calculate the nonlinear refraction coefficients. Both as-grown and intermixed superlattice were treated theoretically and experimentally in order to evaluate their use in monolithically integrated all-optical devices.

The linear properties of as-grown superlattice showed large polarization dependencies. Photoluminescence measurements revealed different optical emission peaks for the TE and TM polarizations, which indicates the lifting of the heavy-hole/light-hole valence band degeneracy. This impacted many of the other optical properties including the linear index of refraction which was larger in the TE mode. As a result, confinement of light to the superlattice core was 20-30% smaller in the TM mode due to the reduced index contrast with the cladding layers. Birefringence in the waveguide also led to a group velocity mismatch between the TE and TM mode and differences in the group velocity dispersion. Intermixed superlattice showed a PL shift of ~150 nm at room temperature and almost no difference between the TE and TM polarizations. Furthermore, the PL peak nearly coincides with the direct bandgap of $\text{Al}_{0.50}\text{Ga}_{0.50}\text{As}$. For this reason, it is believed that intermixed superlattice has reverted into an average alloy of AlGaAs. Linear loss measurements of as-grown superlattice showed

low loss coefficients of $\sim 0.3 \text{ cm}^{-1}$ for the TE mode and $\sim 0.7 \text{ cm}^{-1}$ for the TM mode. Losses in intermixed waveguides were much higher at around 7.5 cm^{-1} in both polarizations which is likely the result of a large defect density and surface roughness. Small PL peaks found on either side of the as-grown superlattice core layer indicate the presence of unintended GaAs quantum wells whose energy levels were found to agree with theoretical calculations.

Nonlinear absorption was measured in as-grown and intermixed waveguides just below the bandgap. For as-grown superlattice, TPA was found to be the dominant nonlinear loss mechanism. The contribution of the buffer and cladding layers was deemed to be negligible based on previous measurements of bulk AlGaAs and the scaling laws for TPA in semiconductors. TPA coefficients in the TE mode were between 1.5 cm/W and 4.0 cm/W , which were nearly four-times larger than in the TM mode and nearly an order of magnitude larger than in bulk AlGaAs. The rapid increase in α_2 for the TE mode at shorter wavelengths and the relative flatness in the TM mode indicate a difference in the TPA resonance points for each polarization. Small peaks in the TPA curves coincide with the half-bandgap energies of the unintended GaAs quantum wells. Intermixed superlattice did not show signs of TPA as expected from the shift in the bandgap, but did show a measurable amount of 3PA when femtosecond pulses with large peak powers were used. 3PA coefficients were on the order of $0.01 \text{ cm}^3/\text{GW}^2$ and showed a polarization dependence. The contribution of the bulk layers to 3PA in intermixed waveguides was deemed to be negligible since the fifth-order effective mode area for the cladding layers was found to be an order of magnitude larger than the effective area of the core layer. When comparing the nonlinear absorption mechanisms, 3PA in intermixed superlattice was found to cause the least amount of loss which validates intermixed superlattice as a relatively linear material.

Nonlinear refraction by self-phase modulation and cross-phase modulation was examined in as-grown and intermixed superlattice waveguides by observing spectral broadening. Calculation of the nonlinear coefficients for the bulk AlGaAs layers by using the direct bandgap scaling laws showed that the buffer and cladding layers contribute significantly to the total nonlinear refraction coefficient of the waveguide structure. The contribution from the indirect bandgap transition for these layers was found to be

negligible. The simple propagation model for a nonlinear medium was found to be insufficient, and thus a more comprehensive model that included dispersion, nonlinear absorption, and pulse shape was used instead. This required a numerical solution that used the split-step Fourier algorithm to simulate a pulse propagating in a nonlinear medium. Using this method, nonlinear refraction coefficients found for the as-grown superlattice core layer were between $1.5 \text{ cm}^2/\text{W}$ and $5.5 \text{ cm}^2/\text{W}$. These values are larger than in bulk AlGaAs and shows similar enhancements as those seen in MQW waveguides. The TE mode had coefficients that were nearly two-times larger than the TM mode at wavelengths near the half-bandgap, which is again the result of the bandgap difference between the polarizations. Measurements of SPM in intermixed superlattice showed a reduction of over an order of magnitude in the value of the nonlinear coefficients. XPM between the TE and TM modes were measured in as-grown superlattice using a pump-probe setup. Group velocity mismatch caused the spectral broadening patterns to become asymmetric. By accounting for this mismatch in the simulator, the XPM nonlinear coefficients were found to steadily increase in the TE mode toward the half-bandgap while the curve for TM mode was flat and relatively featureless. The ratio of XPM-to-SPM was ~ 0.71 for the TE mode and ~ 0.42 for the TE mode.

The application of superlattice to all-optical signal processing devices was explored. The figure of merit calculated showed that superlattice does not perform as well as bulk AlGaAs but is much better than other materials such as silicon and GaAs/AlGaAs MQWs. The power required for switching in a NLDC was larger in superlattice by up to 50% over bulk AlGaAs, but less than half than what is required in other semiconductors. QWI was shown to enable the design of a simplified NLMZI and superlattice was found to have possible benefits over MQWs for fabricating NLMZIs since the nonlinear coefficients exhibit larger reductions in intermixed superlattice. Despite the reduced performance in the nonlinear properties of as-grown superlattice compared to bulk AlGaAs, the ability to intermix superlattice and enable monolithic integration makes up for the lost performance. Thus, overall, superlattice has been shown to be a good platform for creating complex photonic integrated circuits for all-optical signal processing.

6.2 Future Work

The work presented in this thesis gives enough data such that complex nonlinear optical devices can be created. However, not all of the nonlinear properties have been completely characterized and the full potential of superlattice has not been practically demonstrated. Furthermore, changes to the superlattice structure and the intermixing process can be made to improve its properties. Lastly, fabrication of working all-optical switches would demonstrate the viability of superlattice as a platform for nonlinear optics and monolithic integration. Thus, there are several tasks that should be carried out in future studies in order to realize the full potential of superlattice.

As was discussed in Section 4.2.4, superlattice has eight independent non-zero third-order nonlinear susceptibility tensor elements. This thesis dealt with properties that only include six of those elements. Furthermore, three of those elements ($\chi_{xxxx}^{(3)}$, $\chi_{xyxy}^{(3)}$, $\chi_{xxyy}^{(3)}$) are aggregated and inseparable in the measurements taken for the TE mode. A complete characterization of the third-order nonlinear properties of superlattice must include these tensor elements. Measurements of four-wave mixing would be sufficient to characterize the remaining two tensor elements. Isolation of the $\chi_{xxxx}^{(3)}$, $\chi_{xyxy}^{(3)}$, and $\chi_{xxyy}^{(3)}$ elements will require measurement of SPM along different crystallographic directions.

Another issue that must be examined in further detail is the impact of the GaAs quantum wells found at the top and bottom of the superlattice core layer. These wells appear to have significantly altered the linear and nonlinear properties of the waveguides and may even be blamed for some of the non-ideal behaviour observed. This warrants a redesign of the waveguide structure to avoid the formation of these wells. One possible fix is to use AIAs as the topmost and bottommost layers of the superlattice. However, consultation with experienced operators of epitaxy machines resulted in the conclusion that this may complicate the growth process for the superlattice. Further study is required.

Improvements to the intermixing process should be made to give better quality waveguides with less linear loss. The waveguides studied in this thesis are far too lossy for practical application. Other intermixing methods, such as ion-implantation, could be explored. In fact, ion-implantation is preferred for some structures such as QPM since the

achievable resolution is higher. However, attempts to improve silica cap IFVD should be pursued since many structure do not require high resolution and would benefit cost-wise from this less expensive intermixing method.

Fabrication of all-optical switching devices, such as NLDCs and NLMZIs, would help greatly to demonstrate superlattice as a nonlinear material. Active devices, such as lasers and photodetectors, should also be designed and fabricated in superlattice to demonstrate its ability to act as both a passive and active material. Furthermore, such devices should include a mix of as-grown and intermixed material to show the potential of superlattice as a platform for photonic integrated circuits.

Appendix A

Quantum Well Energy Calculations

Overview of Calculation

The GaAs quantum wells found at the top and bottom of the superlattice shown in Figure 2.3 were not intended as part of the waveguide structure. They take the form of asymmetric single quantum wells (ASQW) with a single well material (GaAs) and two different barrier materials (AlAs and $\text{Al}_{0.56}\text{Ga}_{0.44}\text{As}$). Thus, the barrier heights are different on either side of the well. This complicates the calculation of the quantum well energies. However, a solution to this problem was developed by Street using a numerical algorithm based on the shooting method [39]. This solution is summarized here and further details can be found in Ref. [39].

The time-independent 1-D Schrödinger equation for an arbitrary potential profile under the effective mass approximation is expressed as

$$\frac{\hbar}{2} \frac{d}{dz} \left[\frac{1}{m^*(z)} \frac{du(z)}{dz} \right] + v(z)u(z) = Eu(z) \quad (\text{A.1})$$

where $u(z)$ is the envelope function of the bound carrier (either electrons or holes), $m^*(z)$ is the depth-dependent effective mass, $v(z)$ is the potential profile, and E is the eigenenergy. At each heterointerface, the following boundary conditions must be satisfied:

$$u_L(z_i) = u_R(z_i) \quad (\text{A.2})$$

$$\frac{1}{m_L^*} u_L'(z_i) = \frac{1}{m_R^*} u_R'(z_i) \quad (\text{A.3})$$

where the subscripts “*L*” and “*R*” denote the left- and right-side of the interface and z_i is the position of the interface. Exponentially-decaying potential profiles are assumed at the interfaces such that

$$u(z) = \begin{cases} u_{BL}(z) = Ae^{\alpha z} & z \leq 0 \\ u_W(z) & 0 \leq z \leq W \\ u_{BR}(z) = Be^{-\beta z} & z \geq W \end{cases} \quad (\text{A.4})$$

where the subscripts “*BL*” and “*BR*” denote the left and right barriers, W is the width of the well, and A and B are arbitrary constants. To solve Equation (A.1), the shooting algorithm is used which is summarized as follows:

1. A trial eigenenergy is chosen near the actual eigenenergy.
2. An arbitrary value of A is chosen, and the envelope function $u_W(0)$ and its derivative are calculated from the boundary conditions for the left barrier.
3. Equation (A.1) is integrated across the well using a fourth-order Runge-Kutta algorithm.
4. The mismatch in the boundary conditions is calculated for the right barrier. A new trial eigenenergy is chosen such that the mismatch is reduced in the next iteration.
5. If the mismatch falls below some acceptable value, the trial eigenenergy is taken to be approximately equal to the actual eigenenergy.

The algorithm may be further extended to account for any arbitrary potential profile in the well region instead of a flat potential profile. This was done by dividing the potential

profile into small, discrete segments to give a piecewise constant potential profile. The shooting method is applied within each segment across the well.

The computer program used to calculate the quantum well energies implemented the piecewise scheme. This extension of the algorithm was not necessary since the quantum wells dealt with in this study have flat potential profiles in the well region. However, since this code was already developed, known to work, and produces accurate results for most potential profiles, it was used for the calculations in this study.

Results

While AlAs and $\text{Al}_{0.56}\text{Ga}_{0.44}\text{As}$ have indirect bandgaps, “bound” electrons in a quantum well have wavevectors around $k=0$, thus it is appropriate to use the direct bandgap energies when determining the band offsets and barrier heights [80]. Figure A.1 shows the potential profile and parameters with the resulting bound energy levels. The parameters used to calculate the potential profile are summarized in Table A.1. The eigenenergies of two different potential profiles were calculated with the second potential profile having a well width reduced by 10%. This error in the well width is reasonable given the tolerances of the epitaxy process. This was done to match the second set of PL peaks reported in Section 2.3. The results of the calculations for two different well widths are listed in Table A.2. The heavy-hole (*hh*) transitions can only occur for the TE polarization and are thus associated with the TE PL peak. Light-hole (*lh*) transitions occur in either polarization.

Table A.1: Parameters for GaAs quantum well calculations. Note that x represents the Al content ratio.

	Symbol	Value	Source
Bandgap (for direct gap)	E_g	$1.424 + 1.247x$	[41]
Band offset split	$\Delta E_C:\Delta E_V$	65:35	[29]
Effective electron mass	m_C	$0.067 + 0.083x$	[41]
Effective heavy-hole mass	$m_{V,hh}$	$0.62 + 0.14x$	[41]
Effective light-hole mass	$m_{V,lh}$	$0.087 + 0.063x$	[41]

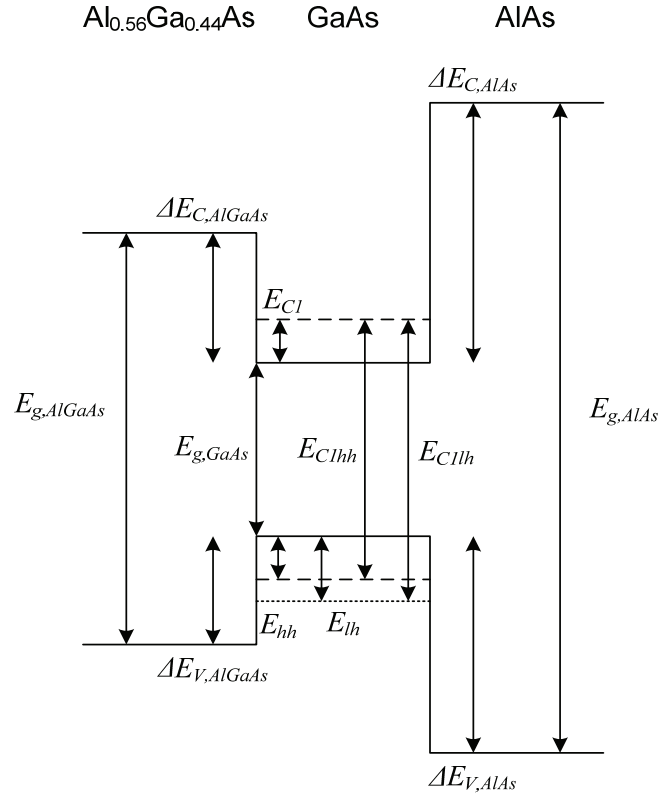


Figure A.1: GaAs quantum well potential profile with relevant energy quantities

Table A.2: Calculated quantities for GaAs ASQWs

	Symbol	Well A	Well B
Well width	W	40 nm	36 nm
Conduction Level 1 Offset	E_{C1}	127 meV	144 meV
Heavy-hole offset	E_{hh}	24.7 meV	29.2 meV
Light-hole offset	E_{lh}	90.2 meV	101 meV
<i>C1hh</i> transition energy	E_{C1hh}	1.576 eV	1.597 eV
<i>C1lh</i> transition energy	E_{C1lh}	1.641 eV	1.669 eV
<i>C1hh</i> emission wavelength	λ_{C1hh}	787 nm	776 nm
<i>C1lh</i> emission wavelength	λ_{C1lh}	756 nm	743 nm

Source Code

The original source code implementing the algorithm known as “The Definitive Schödinger Solver” (TDSS) described here was developed by Michael Street of the University of Glasgow in 1997 [39]. The version of the source code used here was “diffV9”. Small modifications were made including the band offset split (the original split was set to 60:40) and the output data. All source code was written in Pascal.

diffv9 sean.pas

```
PROGRAM DIFFV9;
{DIFFV1 : Calculates the PL peak wavelength (e1 -> hhl transition) as a
function of the diffusion coefficient D for a GaAs square well. e1 and hhl
are calculated for a partially intermixed error function potential profile
using the Schrodinger Solver procedure of TDSSV1}

{DIFFV2 : Calculates the diffusion coefficient D given a measured value for
the PL peak wavelength using a bisection method. It is assumed that
DeltaLambda(D)=Lambdacalc(D)-Lambdameas is a monotonically decreasing
function of D}

{DIFFV3 : Identical to DIFFV2 except that secant methods are now employed
for the numerical solution of the eigenvalue equations. The Schrodinger
Solver procedure is based on that of TDSSV4}

{DIFFV4 : Identical to DIFFV3 except that the goal function
DeltaLambda is calculated as a function of D}

{DIFFV5 : Calculates the diffused Al fraction profile as a function of
the square root of the diffusion coefficient time product SQRT(D*t)
for an ASQW}

{DIFFV6 : ACQW version of DIFFV5}

{DIFFV7 : Calculates the e1 -> hhl PL peak wavelength shift as a function of
the diffusion length SQRT(D*t) for an ASQW}

{DIFFV8 : ACQW version of DIFFV7}

{DIFFV9 : Calculates the e1 -> hhl PL peak wavelength shift, the e2lh1
oscillator strength expressed as a fraction of the starting material
e2lh1 oscillator strength, and the bound electron energy levels as
functions of the diffusion length SQRT(D*t) for an ASQW}

{TDSS (The Definitive Schrodinger Solver) : Solves Shrodinger's equation for
a GaAs/AlGaAs quantum well with an arbitrary potential profile.
Schrodinger's equation is formulated into 2 coupled first order ODE's
involving the wavefunction and its derivative. A continuous potential
profile in the well is defined by a global function and is subsequently
divided into strips and approximated by a piecewise constant profile. A
shooting method is then used for the solution of the eigenvalue equation
which is associated with the boundary conditions at the 2 barrier positions.

At each strip interface position, current continuity is enforced by
calculating 2 values (T1 and T2 say) for the wavefunction gradient:
```

one calculated by integration of Schrodinger's equation across the strip to the left of the interface (T1), and one amended value (T2) which may be calculated from the current continuity condition $T2=T1*mR/mL$ where mL and mR denote the effective masses of the particle in question in the strips to the left and right of the interface respectively.

All the bound energy levels may be found for the particle of interest (electron, light or heavy hole) using extended arithmetic throughout in conjunction with the Fourth Order Runge-Kutta algorithm for the integration of Schrodinger's equation. All electron energies are in meV above the CB edge of GaAs and correspondingly all hole energies are in meV below the VB edge of GaAs. Adachi's parameters for the GaAs/AlGaAs material system are employed throughout with a 60:40 CB:VB energy gap split ratio.}

USES Crt;

CONST

m0 : EXTENDED = 9.109534e-31;
hbarS : EXTENDED = 1.11215725e-68;
q : EXTENDED = 1.6021892e-19;
Eg : EXTENDED = 1424; {Eg for GaAs at 300K in meV}

DeltaZ : EXTENDED = 1e-10;
NW2 = 100;
NW1 = 40;
NB = 40;
N = NW1+NW2+NB;

AlB0 : EXTENDED = 1.0;
AlW1 : EXTENDED = 0.0;
AlW2 : EXTENDED = 0.56;

DeltaDL : EXTENDED = 1e-11;
DeltaDLs = 150;

MaxLevels = 10;

DeltaEs = 100;
EigenError : EXTENDED = 1e-13;

TYPE

LevelArray = ARRAY[1..MaxLevels] OF EXTENDED;
UArray = ARRAY[0..N] OF EXTENDED;
LevelUArray = ARRAY[1..MaxLevels,0..N] OF EXTENDED;

VAR

W1,W2,W,WB,DL,
lh1,Alphalh1,Betalh1,Alh1,Blh1,hh1,Alphahh1,Betahh1,Ahh1,Bhh1,
Lambda0,Lambda1,Lambda,DeltaLambda,OSCe2lh10,OSCe2lh1,AlBL,AlBR : EXTENDED;
Lambdahh1,Lambdahh2,Lambdalh1,Lambdalh2 : EXTENDED;
{DL is the diffusion length in m}

Ulh1,Uhh1,Ue2 : UArray;
es : LevelArray;
Ues : LevelUArray;
Alphaes,Betaes,Aes,Bes : LevelArray;
DLi,Zi : INTEGER;
DataOut : TEXT;
eLevels,eLevel : INTEGER;

FUNCTION erf(X : EXTENDED) : EXTENDED;

{This function returns the value of the error function at X. This polynomial approximation is accurate to within 1.5E-7 and it was taken from the 'Handbook of Mathematical Functions', by Milton Abramowitz.}

```

CONST
  p = 0.3275911;    a1 = 0.254829592;
  a2 = -0.284496736; a3 = 1.421413741;
  a4 = -1.453152027; a5 = 1.061405429;

VAR
  Y : EXTENDED;

FUNCTION F(X : EXTENDED) : EXTENDED;

  BEGIN
    IF ABS(X)>60 THEN
      F:=1 {... For large X, erf(X) = 1 }
    ELSE
      BEGIN
        Y:=1/(1+p*X);
        F:=1-(a1*Y+a2*SQR(Y)+a3*Y*SQR(Y)+a4*SQR(SQR(Y))
              +a5*Y*SQR(SQR(Y)))*exp(-SQR(X));
      END;
    END;

  BEGIN {erf}
    IF X < 0 THEN
      erf := -F(-X)
    ELSE
      erf := F(X)
    END; {erf}

FUNCTION AlF(Z,DL : EXTENDED) : EXTENDED;
{This function returns the Al concentration in the QW, at the position
Z. D and t are the diffusion coefficient of Al and diffusion (annealing)
time respectively}

VAR
  L : EXTENDED;

BEGIN {AlF}

  IF ((DL)<1e-100) THEN
    BEGIN
      IF (Z<=WB/2) THEN
        AlF:=AlB0
      ELSE
        IF (Z<=(W1+WB/2)) THEN
          AlF:=AlW1
        ELSE
          IF (Z<=(W1+W2+WB/2)) THEN
            AlF:=AlW2
          ELSE
            AlF:=AlB0;
        END
      END

    ELSE
      BEGIN
        L:=2*DL;
        AlF:=AlB0-0.5*(AlB0-AlW1)*erf((Z-(WB/2))/L)
              +0.5*(AlW2-AlW1)*erf((Z-((WB/2)+W1))/L)
              +0.5*(AlB0-AlW2)*erf((Z-((WB/2)+W1+W2))/L);
      END;
    END; {AlF}

```

```

FUNCTION AlminF(DL : EXTENDED) : EXTENDED;

VAR
  I : INTEGER;
  Z,min : EXTENDED;

BEGIN {AlminF}
  min:=1;
  Z:=0.5*DeltaZ;
  FOR I:=1 TO N DO
  BEGIN
    IF AlF(Z,DL)<min THEN min:=AlF(Z,DL);
    Z:=Z+DeltaZ;
  END;
  AlminF:=min;
END; {AlminF}

FUNCTION AlmaxF(DL : EXTENDED) : EXTENDED;

BEGIN {AlmaxF}
  IF (ALBL<ALBR) THEN
    AlmaxF:=ALBL
  ELSE
    AlmaxF:=ALBR;
END; {AlmaxF}

FUNCTION VF(Part: INTEGER;X : EXTENDED) : EXTENDED;
{Calculates e and h barrier heights in meV}
{NOTE: CHANGED THE SPLIT RATIO TO 65:35 - SJW}
BEGIN {VF}
  IF Part=1 THEN
    VF:=810.55*X {748.2*X} {e barrier height in meV above CB edge of GaAs}
  ELSE
    VF:=436.45*X; {498.8*X;} {h barrier height in meV below VB edge of GaAs}
END; {VF}

PROCEDURE EvalMismatch
(Part : INTEGER;
Energy : EXTENDED;

VAR Mismatch : EXTENDED;
VAR U : UArray;
VAR Alpha,Beta : EXTENDED);

VAR
mBL,mBR,VBL,VBR,Z1,Z2,A11,A12,V1,V2,F1,F2,m1,m2,T1,T2,C : EXTENDED;
I : INTEGER;

FUNCTION mF(Part : INTEGER;X : EXTENDED) : EXTENDED;

BEGIN {mF}
  IF Part=1 THEN
    mF:=m0*(0.067+0.083*X)      {e}
  ELSE
    IF Part=2 THEN
      mF:=m0*(0.087+0.063*X)    {lh}
    ELSE
      mF:=m0*(0.62+0.14*X);     {hh}
  END; {mF}

```

```

FUNCTION WaveVector(mB,VB,Energy : EXTENDED) : EXTENDED;

BEGIN {WaveVector}
  WaveVector:=SQRT(2*mB*(VB-Energy)*q/(1000*hbarS));
END; {WaveVector}

PROCEDURE RungeKutta
(F : EXTENDED;
 UIm1,TIm1 : EXTENDED;
 VAR UI,TI : EXTENDED);

VAR KU1,KU2,KU3,KU4,KT1,KT2,KT3,KT4 : EXTENDED;

BEGIN {RungeKutta}

  KU1:=DeltaZ*TIm1;
  KT1:=DeltaZ*F*UIm1;

  KU2:=DeltaZ*(TIm1+KT1/2);
  KT2:=DeltaZ*F*(UIm1+KU1/2);

  KU3:=DeltaZ*(TIm1+KT2/2);
  KT3:=DeltaZ*F*(UIm1+KU2/2);

  KU4:=DeltaZ*(TIm1+KT3);
  KT4:=DeltaZ*F*(UIm1+KU3);

  UI:=UIm1+(1/6)*(KU1+KU4+2*(KU2+KU3));
  TI:=TIm1+(1/6)*(KT1+KT4+2*(KT2+KT3));

END; {RungeKutta}

BEGIN {EvalMismatch}
mBL:=mF(Part,AlBL);mBR:=mF(Part,AlBR);
VBL:=VF(Part,AlBL);VBR:=VF(Part,AlBR);

Alpha:=WaveVector(mBL,VBL,Energy);
Beta:=WaveVector(mBR,VBR,Energy);

I:=0;
Z2:=0.5*DeltaZ;
Al2:=AlF(Z2,DL);
V2:=VF(Part,Al2);
m2:=mF(Part,Al2);
F2:=2*m2*(V2-Energy)*q/(1000*hbarS);
U[I]:=1;
C:=Alpha*U[I]/mBL;
T1:=0;
T2:=m2*C;
FOR I:=1 TO N DO
BEGIN
  m1:=m2;
  F1:=F2;
  Z2:=Z2+DeltaZ;
  Al2:=AlF(Z2,DL);
  V2:=VF(Part,Al2);
  m2:=mF(Part,Al2);
  F2:=2*m2*(V2-Energy)*q/(1000*hbarS);

  RungeKutta(F1,U[I-1],T2,U[I],T1);
  {Calculates quantities U[I] and T1 at I in terms of quantities U[I-1]}

```

```

    and T2 at (I-1) and F1 at (I-0.5)}

    C:=T1/m1;
    T2:=m2*C;
    END;

    Mismatch:=C+Beta*U[N]/mBR;

    END; {EvalMismatch}

PROCEDURE EvalEigenU
(Part : INTEGER;
 E1,E2 : EXTENDED;

 VAR Eigen : EXTENDED;
 VAR U : UArray;
 VAR Alpha,Beta,A,B : EXTENDED);

VAR
Mismatch,Mismatch1,Mismatch2,G,E3 : EXTENDED;

BEGIN {EvalEigenU}
EvalMismatch(Part,E1,Mismatch1,U,Alpha,Beta);
REPEAT
    EvalMismatch(Part,E2,Mismatch2,U,Alpha,Beta);
    G:=(Mismatch2-Mismatch1)/(E2-E1);
    E3:=E2-(Mismatch2/G);
    E1:=E2;
    Mismatch1:=Mismatch2;
    E2:=E3;
UNTIL (ABS(E1-E2)<EigenError);
Eigen:=E2;
EvalMismatch(Part,Eigen,Mismatch,U,Alpha,Beta);
A:=U[0];
B:=exp(Beta*W)*U[N];
END; {EvalEigenU}

FUNCTION Overlap
(U1 : UArray;
 Alpha1,Beta1,A1,B1 : EXTENDED;
 U2 : UArray;
 Alpha2,Beta2,A2,B2 : EXTENDED) : EXTENDED;

{This function uses Simpson's Rule to evaluate the overlap integral
between 2 wavefunctions U1 and U2 assuming that the wavefunctions
decay to negligible values at distances equal to the well width
from the well interface positions}

VAR
I : INTEGER;
Z,UL1,UR1,UL2,UR2,Oddsum,Evensum : EXTENDED;

BEGIN {Overlap}
Oddsum:=0;
Evensum:=0;
I:=-N;
REPEAT
    Z:=I*DeltaZ;
    UL1:=A1*exp(Alpha1*Z);
    UL2:=A2*exp(Alpha2*Z);
    Evensum:=Evensum+UL1*UL2;
    I:=I+1;

```

```

Z:=I*DeltaZ;
UL1:=A1*exp(Alpha1*Z);
UL2:=A2*exp(Alpha2*Z);
Oddsum:=Oddsum+UL1*UL2;
I:=I+1;
UNTIL (I=0);

REPEAT
  Evensum:=Evensum+U1[I]*U2[I];
  I:=I+1;
  Oddsum:=Oddsum+U1[I]*U2[I];
  I:=I+1;
UNTIL (I=N);

Evensum:=Evensum+U1[I]*U2[I]; {Account for U1[I]*U2[I] at I=N}

REPEAT
  I:=I+1;
  Z:=I*DeltaZ;
  UR1:=B1*exp(-1*Beta1*Z);
  UR2:=B2*exp(-1*Beta2*Z);
  Oddsum:=Oddsum+UR1*UR2;

  I:=I+1;
  Z:=I*DeltaZ;
  UR1:=B1*exp(-1*Beta1*Z);
  UR2:=B2*exp(-1*Beta2*Z);
  Evensum:=Evensum+UR1*UR2;
UNTIL (I=2*N);

I:=-N;
Z:=I*DeltaZ;
UL1:=A1*exp(Alpha1*Z);
UL2:=A2*exp(Alpha2*Z);
I:=2*N;
Z:=I*DeltaZ;
UR1:=B1*exp(-1*Beta1*Z);
UR2:=B2*exp(-1*Beta2*Z);

Overlap:=(DeltaZ/3)*(2*Evensum-UL1*UL2-UR1*UR2+4*Oddsum);

END; {Overlap}

PROCEDURE Normalize
(VAR U : UArray;
VAR Alpha,Beta,A,B : EXTENDED);

VAR
  I : INTEGER;
  NFactor : EXTENDED;

BEGIN {Normalize}

  NFactor:=SQRT(Overlap(U,Alpha,Beta,A,B,U,Alpha,Beta,A,B));

  A:=A/NFactor;
  B:=B/NFactor;
  FOR I:=0 TO N DO U[I]:=U[I]/NFactor;

END; {Normalize}

PROCEDURE SchrodingerSolver1
(DL : EXTENDED;
Part : INTEGER;

VAR Eigen : EXTENDED;
VAR U : UArray;

```

```

VAR Alpha,Beta,A,B : EXTENDED);

{Calculates the first bound e-value and the corresponding normalised
e-function for particle Part}

VAR
  E1,E2,DeltaE,
  Mismatch1,Mismatch2 : EXTENDED;
  Almin,Almax,Vmin,Vmax : EXTENDED;

BEGIN {SchrodingerSolver1}

  Almin:=AlminF(DL);
  Almax:=AlmaxF(DL);

  Vmin:=VF(Part,Almin);
  Vmax:=VF(Part,Almax);

  DeltaE:=(Vmax-Vmin)/DeltaEs;

  E2:=Vmin;                                     {E in meV}
  EvalMismatch(Part,E2,Mismatch2,U,Alpha,Beta);
  REPEAT
    E1:=E2;
    Mismatch1:=Mismatch2;
    E2:=E1+DeltaE;
    EvalMismatch(Part,E2,Mismatch2,U,Alpha,Beta);
  UNTIL ((Mismatch1*Mismatch2)<0);

  EvalEigenU(Part,E1,E2,Eigen,U,Alpha,Beta,A,B);
  Normalize(U,Alpha,Beta,A,B);

END; {SchrodingerSolver1}

PROCEDURE SchrodingerSolverAll
(DL : EXTENDED;
Part : INTEGER;

VAR LevelsSolved : INTEGER;
VAR Eigens : LevelArray;
VAR Us : LevelUArray;
VAR Alphas,Betas,As,Bs : LevelArray);

{Calculates all of the bound e-values and the corresponding normalised
e-functions for particle Part}

VAR
  E1,E2,DeltaE,
  Mismatch1,Mismatch2 : EXTENDED;
  Almin,Almax,Vmin,Vmax : EXTENDED;
  Eigen : EXTENDED;
  U : UArray;
  Alpha,Beta,A,B : EXTENDED;
  Ei : INTEGER;

PROCEDURE EigenInInterval;

VAR
  I : INTEGER;

BEGIN {EigenInInterval}
  EvalEigenU(Part,E1,E2,Eigen,U,Alpha,Beta,A,B);
  Normalize(U,Alpha,Beta,A,B);
  LevelsSolved:=LevelsSolved+1;
  Eigens[LevelsSolved]:=Eigen;

```

```

FOR I:=0 TO N DO Us[LevelsSolved,I]:=U[I];
Alphas[LevelsSolved]:=Alpha;
Betas[LevelsSolved]:=Beta;
As[LevelsSolved]:=A;
Bs[LevelsSolved]:=B;
END; {EigenInInterval}

BEGIN {SchrodingerSolverAll}

  Almin:=AlminF(DL);
  Almax:=AlmaxF(DL);

  Vmin:=VF(Part,Almin);
  Vmax:=VF(Part,Almax);

  DeltaE:=(Vmax-Vmin)/DeltaEs;

  E2:=Vmin;                                     {E in meV}
  EvalMismatch(Part,E2,Mismatch2,U,Alpha,Beta);

  LevelsSolved:=0;
  FOR Ei:=1 TO (DeltaEs-1) DO
  BEGIN
    E1:=E2;
    Mismatch1:=Mismatch2;
    E2:=E2+DeltaE;
    EvalMismatch(Part,E2,Mismatch2,U,Alpha,Beta);
    IF ((Mismatch1*Mismatch2)<0) THEN EigenInInterval;
  END;
  Ei:=DeltaEs;
  E1:=E2;
  Mismatch1:=Mismatch2;
  E2:=Vmax;
  EvalMismatch(Part,E2,Mismatch2,U,Alpha,Beta);
  IF ((Mismatch1*Mismatch2)<0) THEN EigenInInterval;
END; {SchrodingerSolverAll}

PROCEDURE OutputData;

BEGIN {OutputData}
  WRITE(DL,#9,DeltaLambda:6:2,#9,OSCe2lh1:10:6);
  FOR eLevel:=1 TO (eLevels-1) DO WRITE(#9,es[eLevel]:8:2);
  WRITELN(#9,es[eLevels]:8:2);

  WRITE(DataOut,DL,#9,DeltaLambda:6:2,#9,OSCe2lh1:10:6);
  FOR eLevel:=1 TO (eLevels-1) DO WRITE(DataOut,#9,es[eLevel]:8:2);
  WRITELN(DataOut,#9,es[eLevels]:8:2);
END; {OutputData}

BEGIN {Main Program}
  ASSIGN(DataOut,'out.txt');REWRITE(DataOut);

  ClrScr;

  W1:=NW1*DeltaZ;
  W2:=NW2*DeltaZ;
  WB:=NB*DeltaZ;
  W:=N*DeltaZ;

  {*****}

  {Evaluate starting material parameters}
  DL:=0;

```

```

ALBL:=ALF(0,DL);
ALBR:=ALF(W,DL);
SchrodingerSolverAll(DL,1,eLevels,es,Ues,Alphaes,Betaes,Aes,Bes);
SchrodingerSolver1(DL,2,lh1,Ulh1,Alpha1h1,Beta1h1,Alh1,Blh1);
SchrodingerSolver1(DL,3,hh1,Uhh1,Alpha1hh1,Beta1hh1,Ahh1,Bhh1);
{NOTE: CHANGED OUTPUT DATA - SJW}
Lambdahh1:=1.24e6/(es[1]+hh1+Eg);
Lambdahh2:=1.24e6/(es[2]+hh1+Eg);
Lambdalh1:=1.24e6/(es[1]+lh1+Eg);
Lambdalh2:=1.24e6/(es[2]+lh1+Eg);
WriteLn('HH Transition 1:',Lambdahh1,' nm, (e1 offset: ',es[1],' mEv, hh1 offset:
',hh1,' mEv)');
WriteLn('HH Transition 2:',Lambdahh2,' nm, (e2 offset: ',es[2],' mEv, hh1 offset:
',hh1,' mEv)');
WriteLn('LH Transition 1:',Lambdalh1,' nm, (e1 offset: ',es[1],' mEv, lh1 offset:
',lh1,' mEv)');
WriteLn('LH Transition 2:',Lambdalh2,' nm, (e2 offset: ',es[2],' mEv, lh1 offset:
',lh1,' mEv)');

END.{Main Program}

```

Appendix B

MATLAB Code for the Split-step Fourier Method

Overview

The source code for the split-step Fourier method used in this thesis to study SPM was originally developed by Danielle Modotto of the Università di Brescia. That code is listed under the file `bpm_chi3.m`. The split-step Fourier method implemented is a variation of that described here in which the linear step is split into two “half” steps [3]. Several modifications were made to this code to improve performance and to make it more flexible. Three-photon absorption was added for simulation of intermixed superlattice. The calculation engine was separated into a file named `bpmgnlse.m`. The main program code in `bpm_batch.m` was developed to execute a batch of BPM simulation runs with varying parameters. In most simulation, batch runs varied the power level, thus giving the spectral evolution with input power. To simulate XPM, the code was modified to include a second propagation equation with group velocity mismatch. The XPM code is listed in the files `bpmxpm.m` and `bpmxpm_batch.m`. Chirped super-Gaussian pulses were generated by a file named `gaussian.m`. All code is written in MATLAB.

Source Code

bpm_chi3.m

```
%
% 1-D BPM code (time domain)
% for chi3 (Kerr) nonlinear materials.
% Dispersion (beta2,beta3), Kerr nonlinearity, TPA,
% self-steepening, Raman effect.
%
% July 2005
%

t0=clock;
j=sqrt(-1); % imaginary unit

%
% input data
%

lambda=1.550e-6; % wavelength
k0=2*pi/lambda; % free-space wave number
c=3e8 ; % velocity of light
nu=c/lambda ; % frequency

% dispersion coefficients
beta2=-1.28e-24; % GVD (m^-1 s^2)
beta3=7.5779e-39; % third-order dispersion (m^-1 s^3)

% nonlinearity
n2=1.6e-13*1e-4; % Kerr coefficient (m^2/Watt)
Aeff=1.65e-12; % waveguide effective area (m^2)
gamma=(2*pi/lambda)*(n2/Aeff); % nonlinear parameter
steep_on=1; % 1 if self-steepening is present, 0 otherwise
raman_on=1; % 1 if Raman effect is present, 0 otherwise
Tr=3.289e-15; % slope of the Raman gain (s)

% losses
alpha=0 ; % (m^-1 )linear propagation loss
alpha2=0 ; % (m /Watt) 2-photon absorption coefficient

% numerical simulation data
pointt=1024; % number of points along t (time)
iterations=10000; % number of iterations along z (the number of points along z is
iterations+1)
numplots=100; % the number of plots along z is numplots+1
njump=iterations/numplots;
%
tmax=2e-12; % temporal window from -tmax to tmax
zmax=0.0040 ; % propagation from 0 to zmax
%
deltat=2*tmax/pointt; % step along t
deltaz=zmax/(iterations); % step along z

% input field
T0=32.89e-15 ;
%T0=162e-15/1.665 ; % T0=FWHM/1.665 (for a Gaussian pulse)
%amp=2*sqrt(abs(beta2)/(gamma*T0^2)) % soliton amplitude (only if beta2<0)
amp=10.97; % amplitude (sqrt(Watt))
C=0; % chirp
t=-tmax:deltat:tmax-deltat;

% Gaussian (chirped) pulse
%q=amp*exp(-(1+j*C)*(t/(sqrt(2)*T0)).^2);
%
q=amp*sech(t/T0); % temporal soliton
```

```

%
% asymmetric input pulse
%tshift=1*1.4*T0;
%factor=1*0.4;
%q=amp*(exp(-(1+j*C)*((t-0)/(sqrt(2)*T0)).^2)+...
%      1*factor*exp(-(1+j*C)*((t-tshift)/(sqrt(2)*T0)).^2) );

%-----
%-----
% vectors
indfreq=-pointt/2:1:pointt/2-1; % frequencies of the numerical algorithm
omega=(pi./tmax).*indfreq;
prop=(beta2/2)*(omega.^2)-(beta3/6)*(omega.^3); % dispersion in the frequency domain
%
distance=[];
real_q=[]; % real part of the electric field
imag_q=[]; % imaginary part of the electric field
Q=[]; % power
Qnorm=[]; % normalized power
Qfft=[]; % power spectrum
Qfftnorm=[]; % normalized power spectrum
real_q=[real_q real(q')];
imag_q=[imag_q imag(q')];
Q=[Q abs(q').^2];
Qnorm=[Qnorm (abs(q').^2)/max(abs(q').^2)];
Qfft=[Qfft abs(deltat*fftshift(fft(q'))).^2 ];
Qfftnorm=[Qfftnorm abs(fftshift(fft(q'))).^2/...
          max(abs(fftshift(fft(q'))).^2) ];
energy=[]; % energy
deltat*sum((abs(q).^2) );

energy=[energy deltat*sum((abs(q).^2))] ;
distance=[distance 0];
%
% MAIN PROGRAM
%
for loop_step=1:1:iterations
%
% FFT and (HALF) linear step
qs=deltat*fftshift(fft(q)); % FFT
fact=j.*prop.*0.5*deltaz;
qs=exp(fact).*qs; % propagation in the frequency domain
qs_old=qs;
q=(1/deltat)*ifft(ifftshift(qs));
% self-steepening (in the frequency domain)
if steep_on==1
    steepening=deltat*fftshift(fft((abs(q).^2).*q));
    qs=qs-(n2/(Aeff*c))*(j*2*omega).*steepening*deltaz;
end
% Raman
if raman_on==1
    term_fft=deltat*fftshift(fft(abs(q).^2));
    convolution=(1/(deltat*pointt))*conv(qs_old,j*omega.*term_fft);
    convolution=convolution(pointt/2+1:1:pointt/2+pointt);
    qs=qs-j*gamma*Tr*convolution*deltaz;
end
% IFFT (back in the time domain)
q=(1/deltat)*ifft(ifftshift(qs));
% nonlinear step (Kerr effect)
q=q.*exp(j*(gamma*(abs(q).^2)).*deltaz );
% linear and nonlinear losses
q=q.*exp(-(0.5*alpha +0.5*(alpha2/Aeff)*abs(q).^2 ).*deltaz);

% FFT and (HALF) linear step
qs=deltat*fftshift(fft(q)); % FFT
% qs_old=qs;
fact=j.*prop.*0.5*deltaz;
qs=exp(fact).*qs; % propagation in the frequency domain
% IFFT (back in the time domain)
q=(1/deltat)*ifft(ifftshift(qs));
%

```

```

    if rem(loop_step,njump)==0 % if loop_step is multiple of njump, it saves the results
        loop_step
        calculated_energy=deltat*sum((abs(q).^2))
        energy=[energy deltat*sum((abs(q).^2))] ;
        real_q=[real_q real(q')];
        imag_q=[imag_q imag(q')];
        Q=[Q abs(q').^2];
        Qnorm=[Qnorm (abs(q').^2)/max(abs(q').^2)];
        Qfft=[Qfft abs(qs').^2];
        Qfftnorm=[Qfftnorm abs(qs').^2/max(abs(qs').^2)];
        zeta=loop_step*deltaz ;
        distance=[distance zeta];
    end
end;
t_elapsed=etime(clock,t0)
%
%-----
%-----

% it saves the results to files

[lt,lz]=size(Q);
step_t=1;
real_q=real_q(1:step_t:lt,:) ;
imag_q=imag_q(1:step_t:lt,:) ;
Q=Q(1:step_t:lt,:) ;
Qnorm=Qnorm(1:step_t:lt,:) ;
Qfft=Qfft(1:step_t:lt,:) ;
Qfftnorm=Qfftnorm(1:step_t:lt,:) ;
t=t(1:step_t:lt) ;
indfreq=indfreq(1:step_t:lt);
deltat=deltat*step_t;

save real_q.dat real_q -ascii % real part of the electric field
save imag_q.dat imag_q -ascii % imaginary part of the electric field
save Q.dat Q -ascii % power
save Qnorm.dat Qnorm -ascii % normalized power
save Qfft.dat Qfft -ascii % power spectrum
save Qfftnorm.dat Qfftnorm -ascii % normalized power spectrum
save energy.dat energy -ascii
save z.dat distance -ascii % z
save t.dat t -ascii % time
save freq.dat indfreq -ascii % frequencies of the numerical algorithm
save deltat.dat deltat -ascii % time step
save lambda.dat lambda -ascii % central wavelength

```

gaussian.m

```

function q = gaussian(FWHM, amp, t, C, tshift, factor, m)

%
% Asymmetric Super-Gaussian pulse generator with chirp
%
% August 24, 2005
% Sean Wagner
% Department of Electrical and Computer Engineering
% University of Toronto
%
% Based on Matlab code originally written by D. Modotto.
%
% $Id: gaussian.m,v 1.2 2005/10/26 21:53:56 Sean Exp $
%
% PARAMETERS
% FWHM - full width at half maximum (s)
% amp - peak amplitude (sqrt(Watt))
% t - vector of time values (s)
% C - chirp parameter [OPTIONAL]

```

```

% tshift          - asymmetric pulse temporal shift [OPTIONAL]
% factor          - asymmetric pulse amplitude factor [OPTIONAL]
%
if nargin<7
    m=1;
end;

if nargin<6
    factor=0;
    tshift=0;
end;
if nargin<4
    C=0;
end;

T0=FWHM/1.665;

q=amp*(exp(-(1+j*C)/2.*((t/T0).^2).^m)+...
    1*factor*exp(-(1+j*C)/2.*(((t-tshift)/T0).^2).^m) );

```

bpmgnlse.m

```

function [qout, z, t_elapsed] = bpmgnlse(params, qin)
%
% 1-D BPM code (time domain)
% for chi3 (Kerr) nonlinear materials.
% Dispersion (beta2,beta3), Kerr nonlinearity, TPA,
% self-steepening, Raman effect.
%
% August 23, 2005
% Sean Wagner
% Department of Electrical and Computer Engineering
% University of Toronto
%
% Based on code bpm_chi3.m originally written by D. Modotto
%
% $Id: bpmgnlse.m,v 1.2 2005/09/29 19:05:53 Sean Exp $
%
% USAGE:
%
% Submit a structure (param) with the following fields and proper
% units:
%
% params.runnum      - Run number
% params.lambda      - Center wavelength (m)
% params.beta2       - GVD (m^-1 s^2)
% params.beta3       - Third-order dispersion (m^-1 s^3)
% params.n2          - Kerr coefficient (m^2/Watt)
% params.Aeff        - Waveguide effective area (m^2)
% params.steep_on    - 1 to include self-steepening effect
% params.raman_on    - 1 to include Raman effect
% params.Tr          - slope of Raman gain (s)
% params.alpha       - Linear loss coefficient (m^-1)
% params.alpha2      - 2-photon absorption coefficient (m Watt^-1)
% params.iterations  - number of iterations along z
% params.numplots    - number of points along z to return
% params.reportpnts  - number of points along z to report on screen
% params.deltat      - temporal step interval (s)
% params.deltaz      - spatial step interval (m)
%
% RETURNS
% q                  - complex field envelope over t and z
% freq               - vector of independent frequencies
% z                  - vector of z coordinates (m)
% telapsed           - calculation time (s)
%
%

```

```

% Constants
%
j=sqrt(-1); % imaginary unit
c=299792458; % velocity of light (m s^-1)

%
% Constant parameters for calculations
%
runnum=params.runnum;
deltat=params.deltat;
deltaz=params.deltaz;
n2=params.n2;
beta2=params.beta2;
beta3=params.beta3;
Aeff=params.Aeff;
Aeff5=params.Aeff5;
lambda=params.lambda;
alpha=params.alpha;
alpha2=params.alpha2;
alpha3=params.alpha3;
Tr=params.Tr;
raman_on=params.raman_on;
steep_on=params.steep_on;
iterations=params.iterations;
numplots=params.numplots;
reportpnts=params.reportpnts;

%-----
%-----
tic;
gamma=(2*pi/lambda)*(n2/Aeff); % nonlinear parameter
njump=iterations/numplots;
nreport=iterations/reportpnts;
pointt=length(qin);
% vectors
indfreq=-pointt/2:1:pointt/2-1; % frequencies of the numerical algorithm
omega=(pi./(pointt*deltat)).*indfreq;
prop=(beta2/2)*(omega.^2)-(beta3/6)*(omega.^3); % dispersion in the frequency domain
qout=[];
qout=[qout qin'];
z=[];
z=[z 0];
q=qin;

%
% MAIN PROGRAM
%
for loop_step=1:1:params.iterations
%
% FFT and (HALF) linear step
qs=deltat*fftshift(fft(q)); % FFT
fact=j.*prop.*0.5*deltaz;
qs=exp(fact).*qs; % propagation in the frequency domain
qs_old=qs;
q=(1/deltat)*ifft(ifftshift(qs));
% self-steepening (in the frequency domain)
if steep_on==1
steepening=deltat*fftshift(fft((abs(q).^2).*q));
qs=qs-(n2/(Aeff*c))*(j*2*omega).*steepening*deltaz;
end
% Raman
if raman_on==1
term_fft=deltat*fftshift(fft(abs(q).^2));
convolution=(1/(deltat*pointt))*conv(qs_old,j*omega.*term_fft);
convolution=convolution(pointt/2+1:1:pointt/2+pointt);
qs=qs-j*gamma*Tr*convolution*deltaz;
end
% IFFT (back in the time domain)
q=(1/deltat)*ifft(ifftshift(qs));
% nonlinear step (Kerr effect)

```

```

q=q.*exp(j*(gamma*(abs(q).^2)).*deltaz );
% linear and nonlinear losses
q=q.*exp(-(0.5*alpha +0.5*(alpha2/Aeff)*abs(q).^2 +0.5*(alpha3/Aeff5^2)*abs(q).^4
).*deltaz);
% FFT and (HALF) linear step
qs=deltat*fftshift(fft(q)); % FFT
fact=j.*prop.*0.5*deltaz;
qs=exp(fact).*qs; % propagation in the frequency domain
% IFFT (back in the time domain)
q=(1/deltat)*ifft(ifftshift(qs));
% Record along z
if rem(loop_step,nreport)==0
    runnum
    loop_step
    qsqr = abs(q).^2;
    calculated_energy=deltat*sum(qsqr)
end
if rem(loop_step,njump)==0 % if loop_step multiple of njump, saves results
    qsqr = abs(q).^2;
    qout=[qout q'];
    zeta=loop_step*deltaz ;
    z=[z zeta];
end
end;
t_elapsed = toc

```

bpm_batch.m

```

%
% BPM Batch
% Runs a series of 1-D BPM simulations using bpmgnlse.m
%
% September 2, 2005
% Sean Wagner
% Department of Electrical and Computer Engineering
% University of Toronto
%
% Based on code bpm_chi3.m originally written by D. Modotto
%
% $Id: bpm_batch.m,v 1.2 2005/09/29 19:05:34 Sean Exp $
%
% USAGE:
%
% Submit a structure (param) with the following fields and proper
% units:
%
% params.runnum          - Run number
% params.lambda          - Center wavelength (m)
% params.beta2           - GVD (m-1 s2)
% params.beta3           - Third-order dispersion (m-1 s3)
% params.n2              - Kerr coefficient (m2/Watt)
% params.Aeff            - Waveguide effective area (m2)
% params.steep_on        - 1 to include self-steepening effect
% params.raman_on        - 1 to include Raman effect
% params.Tr              - slope of Raman gain (s)
% params.alpha           - Linear loss coefficient (m-1)
% params.alpha2          - 2-photon absorption coefficient (m Watt-1)
% params.iterations      - number of iterations along z
% params.numplots        - number of points along z to return
% params.reportpnts      - number of points along z to report on screen
% params.deltat          - temporal step interval (s)
% params.deltaz          - spatial step interval (m)
%
%
clear all

%
% Constants

```

```

%
j=sqrt(-1); % imaginary unit
c=299792458; % velocity of light (m s^-1)

%
% Description
%
description = 'Superlattice intermixed TE, 1450nm (2006-0504-data07)';
filepath    = './results/2006/07 2006/2407';
dataset     = 'dataset04';
scantype    = 'pwr';

%
% Setup results directory

system(['mkdir "', filepath, '"'])

%
% Batch run parameters
%
numruns     = 41; % Number of runs to do

%
% Temporal and spatial paramters
%
lambda      = 1445e-9; % center wavelength (m)
pointt     = 2^12; % number of points along t (time)
zeropadfact = 2^2; % zero padding factor
tmax       = 2e-12; % temporal window from -tmax to tmax (s)
zmax       = 0.005; % propagation from 0 to zmax (m)
iterations = 200; % number of z points to take

deltat=2*tmax/pointt; % step along t
deltaz=zmax/(iterations); % step along z

%
% Simulation and material parameters
%
n2 = linspace(0.3e-17, 0.5e-17, numruns);

params=[];
for i=1:numruns
    params(i).runnum = i;
    params(i).lambda = lambda; % Center wavelength (m)
    params(i).beta2 = 0.981e-24; % GVD (m^-1 s^2)
    params(i).beta3 = 0; % Third-order dispersion (m^-1 s^3)
    params(i).n2 = 0.42e-17; % Kerr coefficient (m^2/Watt)
    params(i).Aeff = 7.84e-12; % effective area (m^2)
    params(i).Aeff5 = 6.5e-12; % fifth-order effective area (m^2)
    params(i).steep_on = 1; % 1 to include self-steepening effect
    params(i).raman_on = 0; % 1 to include Raman effect
    params(i).Tr = 0; % slope of Raman gain (s)
    params(i).alpha = 7.2e2; % Linear loss coefficient (m^-1)
    params(i).alpha2 = 0; % 2-photon absorption (m Watt^-1)
    params(i).alpha3 = 1.58e-26; % 3-photon absorption (m^3 Watt^-2)
    params(i).iterations = iterations; % number of iterations along z
    params(i).numplots = 1; % number of points along z to return
    params(i).reportpnts = 100; % Number of points to report on-screen
    params(i).deltat = deltat; % temporal step interval (s)
    params(i).deltaz = deltaz; % spatial step interval (m)
end;

%
% Input Pulse
%
pwr = linspace(1,3000,numruns); % Peak power (W)
%pwr = repmat([2035],1,numruns);
FWHM = 173e-15; % Full width half maximum (s)
C = 0.6; % chirp

```

```

tshift = 0; %-0.6*FWHM/1.665;
factor = 0; % 0.2;
m = 1.2; % Super-gaussian factor

t = -tmax : deltat : tmax*(2*zeropadfact-1)-deltat;
q = gaussian(FWHM, 1, t, C, tshift, factor, m);
%q = sechpulse(FWHM, 1, t, C);

%
% Run Simulation
%
for i=1:numruns
    qout=[];
    z=[];
    qin=q.*sqrt(pwr(i));
    qout=[qout qin];
    [qout, z, t_elapsed] = bpmgnlse(params(i), qin);
    %
    % Save Results
    %
    filename = [filepath, '/', dataset, '_', num2str(i, '%.4u')];
    save(filename);
    fid = fopen([filename, '.txt'], 'w');
    datetime = datestr(now, 'yyyy-mm-dd-HHhMM.SS');
    fprintf(fid, '**GNLSE BPM SIMULATION PARAMETERS**\n');
    fprintf(fid, 'Date/Time run: %s\n', datetime);
    fprintf(fid, 'Simulation time: %d\n\n', t_elapsed);
    fprintf(fid, 'Description:\n%s\n\n', description);
    fclose(fid);
end;

```

bpmxpm.m

```

function [qout_pm, qout_pb, z, t_elapsed] = bpmxpm(params, qin_pm, qin_pb)
%
% 1-D BPM code (time domain) for chi3 (Kerr) nonlinear materials with XPM.
%
% Dispersion (beta2,beta3), Kerr nonlinearity, TPA,
% self-steepening, Raman effect, cross-phase modulation (XPM).
%
% Note: This simulation is only for probe and pump at same wavelength, but
%       different polarization.
%
% March 23, 2005
% Sean Wagner
% Department of Electrical and Computer Engineering
% University of Toronto
%
% Based on code bpm_chi3.m originally written by D. Modotto
%
% $Id: bpmxpm.m,v 1.1 2006/03/23 22:27:07 Sean Exp $
%
% USAGE:
%
% Submit a structure (param) with the following fields and proper
% units:
%
% params.runnum      - Run number
% params.lambda_pm   - Center wavelength (m) for PUMP
% params.lambda_pb   - Center wavelength (m) for PROBE
% params.beta1_pm    - First-order dispersion (m^-1 s) for PUMP
% params.beta1_pb    - First-order dispersion (m^-1 s) for PROBE
% params.beta2_pm    - GVD (m^-1 s^2) for PUMP
% params.beta2_pb    - GVD (m^-1 s^2) for PROBE
% params.beta3_pm    - Third-order dispersion (m^-1 s^3) for PUMP
% params.beta3_pb    - Third-order dispersion (m^-1 s^3) for PROBE
% params.n2_pm       - Kerr coefficient (m^2/Watt) for PUMP
% params.n2_pb       - Kerr coefficient (m^2/Watt) for PROBE

```

```

% params.xn2_pm      - Cross Kerr coefficient (m^2/Watt) for PUMP
% params.xn2_pb      - Cross Kerr coefficient (m^2/Watt) for PROBE
% params.Aeff_pm     - Waveguide effective area (m^2) for PUMP
% params.Aeff_pb     - Waveguide effective area (m^2) for PROBE
% params.steep_on    - 1 to include self-steepening effect
% params.raman_on    - 1 to include Raman effect
% params.Tr_pm       - slope of Raman gain (s) for PUMP
% params.Tr_pb       - slope of Raman gain (s) for PROBE
% params.alpha_pm    - Linear loss coefficient (m^-1) for PUMP
% params.alpha_pb    - Linear loss coefficient (m^-1) for PROBE
% params.alpha2_pm   - 2-photon absorption coefficient (m Watt^-1) for PUMP
% params.alpha2_pb   - 2-photon absorption coefficient (m Watt^-1) for PROBE
% params.iterations  - number of iterations along z
% params.numplots    - number of points along z to return
% params.reportpnts  - number of points along z to report on screen
% params.deltat      - temporal step interval (s)
% params.deltaz      - spatial step interval (m)
% qin_pm             - PUMP input
% qin_pb             - PROBE input
%
% RETURNS
% qout_pm            - complex field envelope over t and z for PUMP
% qout_pb            - complex field envelope over t and z for PROBE
% z                  - vector of z coordinates (m)
% telapsed           - calculation time (s)
%
%
% Constants
%
j=sqrt(-1); % imaginary unit
c=299792458; % velocity of light (m s^-1)
%
% Constant parameters for calculations
%
runnum = params.runnum; % Run number
lambda_pm = params.lambda_pm; % Center wavelength (m)
lambda_pb = params.lambda_pb; % Center wavelength (m)
beta1_pm = params.beta1_pm; % First-order dispersion (m^-1 s) PUMP
beta1_pb = params.beta1_pb; % First-order dispersion (m^-1 s) PROBE
beta2_pm = params.beta2_pm; % GVD (m^-1 s^2) PUMP
beta2_pb = params.beta2_pb; % GVD (m^-1 s^2) PROBE
beta3_pm = params.beta3_pm; % Third-order dispersion (m^-1 s^3) PUMP
beta3_pb = params.beta3_pb; % Third-order dispersion (m^-1 s^3) PROBE
n2_pm = params.n2_pm; % Kerr coefficient (m^2/Watt) PUMP
n2_pb = params.n2_pb; % Kerr coefficient (m^2/Watt) PROBE
xn2_pm = params.xn2_pm; % Cross Kerr coefficient (m^2/Watt) PUMP
xn2_pb = params.xn2_pb; % Cross Kerr coefficient (m^2/Watt) PROBE
Aeff_pm = params.Aeff_pm; % Waveguide effective area (m^2) PUMP
Aeff_pb = params.Aeff_pb; % Waveguide effective area (m^2) PROBE
steep_on = params.steep_on; % 1 to include self-steepening effect
raman_on = params.raman_on; % 1 to include Raman effect
Tr_pm = params.Tr_pm; % slope of Raman gain (s) PUMP
Tr_pb = params.Tr_pb; % slope of Raman gain (s) PROBE
alpha_pm = params.alpha_pm; % Linear loss coefficient (m^-1) PUMP
alpha_pb = params.alpha_pb; % Linear loss coefficient (m^-1) PROBE
alpha2_pm = params.alpha2_pm; % 2-photon absorption (m Watt^-1) PUMP
alpha2_pb = params.alpha2_pb; % 2-photon absorption (m Watt^-1) PROBE
xalpha2_pm = params.alpha2_pm; %- cross 2-photon absorption (m Watt^-1) PUMP
xalpha2_pb = params.alpha2_pb; %- cross 2-photon absorption (m Watt^-1) PROBE
iterations = params.iterations; %- number of iterations along z
numplots = params.numplots; %- number of points along z to return
reportpnts = params.reportpnts; %- number of points along z to report on screen
deltat = params.deltat; %- temporal step interval (s)
deltaz = params.deltaz; %- spatial step interval (m)

%-----
%-----
tic;

```

```

gamma_pm=(2*pi/lambda_pm)*(n2_pm/Aeff_pm); % nonlinear parameter for PUMP
gamma_pb=(2*pi/lambda_pb)*(n2_pb/Aeff_pb); % nonlinear parameter for PROBE
xgamma_pm=(2*pi/lambda_pb)*(xn2_pb/Aeff_pb);
xgamma_pb=(2*pi/lambda_pm)*(xn2_pm/Aeff_pm);
d=beta1_pb-beta1_pm;
njump=iterations/numplots;
nreport=iterations/reportpnts;
pointt=length(qin_pm);
% vectors
indfreq=-pointt/2:1:pointt/2-1; % frequencies of the numerical algorithm
omega=(pi./(pointt*deltat)).*indfreq;
% dispersion in frequency domain PUMP
prop_pm=(beta2_pm/2)*(omega.^2)-(beta3_pm/6)*(omega.^3);
% dispersion in frequency domain PROBE
prop_pb=-d.*omega+(beta2_pb/2)*(omega.^2)-(beta3_pb/6)*(omega.^3);
qout_pm=[];
qout_pb=[];
qout_pm=[qout_pm qin_pm'];
qout_pb=[qout_pb qin_pb'];
z=[];
z=[z 0];
q_pm=qin_pm;
q_pb=qin_pb;

%
% MAIN PROGRAM
%
for loop_step=1:l:params.iterations
%
% FFT and (HALF) linear step
qs_pm=deltat*fftshift(fft(q_pm)); % FFT of PUMP
qs_pb=deltat*fftshift(fft(q_pb)); % FFT of PROBE
fact_pm=j.*prop_pm.*0.5*deltaz;
fact_pb=j.*prop_pb.*0.5*deltaz;
qs_pm=exp(fact_pm).*qs_pm; % propagation in frequency domain for PUMP
qs_pb=exp(fact_pb).*qs_pb; % propagation in frequency domain for PROBE
qs_pm_old=qs_pm;
qs_pb_old=qs_pb;
q_pm=(1/deltat)*ifft(ifftshift(qs_pm)); % iFFT of PUMP
q_pb=(1/deltat)*ifft(ifftshift(qs_pb)); % iFFT of PROBE
q_pm_save=q_pm;
q_pb_save=q_pb;
% self-steepening (in the frequency domain)
if steep_on==1
steepening_pm=deltat*fftshift(fft((abs(q_pm).^2).*q_pm));
steepening_pb=deltat*fftshift(fft((abs(q_pb).^2).*q_pb));
qs_pm=qs_pm-(n2_pm/(Aeff_pm*c))*(j*2*omega).*steepening_pm*deltaz;
qs_pb=qs_pb-(n2_pb/(Aeff_pb*c))*(j*2*omega).*steepening_pb*deltaz;
end
% Raman
if raman_on==1
term_fft_pm=deltat*fftshift(fft(abs(q_pm).^2));
term_fft_pb=deltat*fftshift(fft(abs(q_pb).^2));
convolution_pm=(1/(deltat*pointt))*conv(qs_pm_old,j*omega.*term_fft_pm);
convolution_pb=(1/(deltat*pointt))*conv(qs_pb_old,j*omega.*term_fft_pb);
convolution_pm=convolution_pm(pointt/2+1:1:pointt/2+pointt);
convolution_pb=convolution_pb(pointt/2+1:1:pointt/2+pointt);
qs_pm=qs_pm-j*gamma_pm*Tr_pm*convolution_pm*deltaz;
qs_pb=qs_pb-j*gamma_pb*Tr_pb*convolution_pb*deltaz;
end
% IFFT (back in the time domain)
q_pm=(1/deltat)*ifft(ifftshift(qs_pm));
q_pb=(1/deltat)*ifft(ifftshift(qs_pb));
% nonlinear step (Kerr effect)
q_pm=q_pm.*exp(j*(gamma_pm*abs(q_pm).^2+xgamma_pm*abs(q_pb_save).^2).*deltaz);
q_pb=q_pb.*exp(j*(gamma_pb*abs(q_pb).^2+xgamma_pb*abs(q_pm_save).^2).*deltaz);
% linear and nonlinear losses
q_pm=q_pm.*exp(-0.5*(alpha_pm+(alpha2_pm/Aeff_pm)*abs(q_pm).^2+(xalpha2_pm/Aeff_pb) ...
*abs(q_pb).^2).*deltaz);
q_pb=q_pb.*exp(-0.5*(alpha_pb+(alpha2_pb/Aeff_pb)*abs(q_pb).^2+(xalpha2_pb/Aeff_pm) ...
*abs(q_pm).^2).*deltaz);

```

```

% FFT and (HALF) linear step
qs_pm=deltat*fftshift(fft(q_pm)); % FFT
qs_pb=deltat*fftshift(fft(q_pb)); % FFT
fact_pm=j.*prop_pm.*0.5*deltaz;
fact_pb=j.*prop_pb.*0.5*deltaz;
qs_pm=exp(fact_pm).*qs_pm; % propagation in the frequency domain
qs_pb=exp(fact_pb).*qs_pb; % propagation in the frequency domain
% IFFT (back in the time domain)
q_pm=(1/deltat)*ifft(ifftshift(qs_pm));
q_pb=(1/deltat)*ifft(ifftshift(qs_pb));
% Record along z
if rem(loop_step,nreport)==0
    runnum
    loop_step
    qsqr_d_pm = abs(q_pm).^2;
    qsqr_d_pb = abs(q_pb).^2;
    calculated_energy_pm=deltat*sum(qsqr_d_pm)
    calculated_energy_pb=deltat*sum(qsqr_d_pb)
end
if rem(loop_step,njump)==0 % if loop_step multiple of njump, saves results
    qsqr_d_pm = abs(q_pm).^2;
    qsqr_d_pb = abs(q_pb).^2;
    qout_pm=[qout_pm q_pm'];
    qout_pb=[qout_pb q_pb'];
    zeta=loop_step*deltaz ;
    z=[z zeta];
end
end;
t_elapsed = toc

```

bpmxpm batch.m

```

%
% BPM XPM Batch
% Runs a series of 1-D BPM simulations using bpmxpm.m
%
% March 23, 2006
% Sean Wagner
% Department of Electrical and Computer Engineering
% University of Toronto
%
% Based on code bpm_chi3.m originally written by D. Modotto
%
% $Id:$
%
% USAGE:
%
% Submit a structure (param) with the following fields and proper
% units:
%
% params.runnum          - Run number
% params.lambda_pm      - Center wavelength (m) for PUMP
% params.lambda_pb      - Center wavelength (m) for PROBE
% params.beta1_pm       - First-order dispersion (m^-1 s) for PUMP
% params.beta1_pb       - First-order dispersion (m^-1 s) for PROBE
% params.beta2_pm       - GVD (m^-1 s^2) for PUMP
% params.beta2_pb       - GVD (m^-1 s^2) for PROBE
% params.beta3_pm       - Third-order dispersion (m^-1 s^3) for PUMP
% params.beta3_pb       - Third-order dispersion (m^-1 s^3) for PROBE
% params.n2_pm          - Kerr coefficient (m^2/Watt) for PUMP
% params.n2_pb          - Kerr coefficient (m^2/Watt) for PROBE
% params.B_pm          - SPM/XPM ratio for PROBE on PUMP
% params.B_pb          - SPM/XPM ratio for PUMP on PROBE
% params.Aeff_pm       - Waveguide effective area (m^2) for PUMP
% params.Aeff_pb       - Waveguide effective area (m^2) for PROBE
% params.steep_on       - 1 to include self-steepening effect
% params.raman_on       - 1 to include Raman effect

```

```

% params.Tr_pm          - slope of Raman gain (s) for PUMP
% params.Tr_pb          - slope of Raman gain (s) for PROBE
% params.alpha_pm       - Linear loss coefficient (m^-1) for PUMP
% params.alpha_pb       - Linear loss coefficient (m^-1) for PROBE
% params.alpha2_pm      - 2-photon absorption coefficient (m Watt^-1) for PUMP
% params.alpha2_pb      - 2-photon absorption coefficient (m Watt^-1) for PROBE
% params.iterations     - number of iterations along z
% params.numplots       - number of points along z to return
% params.reportpnts     - number of points along z to report on screen
% params.deltat         - temporal step interval (s)
% params.deltaz         - spatial step interval (m)
%
%
clear all

%
% Constants
%
j=sqrt(-1); % imaginary unit
c=299792458; % velocity of light (m s^-1)

%
% Description
%
description = 'Superlattice as-grown, TE pump, TM probe, WG31, 1545nm with XTPA';
filepath    = '\results\2006\07 2006\0507';
dataset     = 'dataset03';
scantype    = 'pwr';

%
% Setup results directory

system(['mkdir "', filepath, "'"])

%
% Batch run parameters
%
numruns     = 21; % Number of runs to do

%
% Temporal and spatial paramters
%
lambda_pm   = 1544.95e-9; % center wavelength (m)
lambda_pb   = 1544.95e-9; % center wavelength (m)
pointt      = 2^12; % number of points along t (time)
zeropadfact = 2^2; % zero padding factor
tmax        = 8e-12; % temporal window from -tmax to tmax (s)
zmax        = 0.012; % propagation from 0 to zmax (m)
iterations  = 400; % number of z points to take

deltat=2*tmax/pointt; % step along t
deltaz=zmax/(iterations); % step along z

%
% Simulation and material parameters
%
n2 = linspace(1.1e-17, 1.3e-17, numruns);

params=[];
for i=1:numruns
    params(i).runnum = i;
    params(i).lambda_pm = lambda_pm; % Center wavelength (m) for PUMP
    params(i).lambda_pb = lambda_pb; % Center wavelength (m) for PROBE
    params(i).beta1_pm = 10.767e-9; % First-order dispersion (m^-1 s) for PUMP
    params(i).beta1_pb = 10.695e-9; % First-order dispersion (m^-1 s) for PROBE
    params(i).beta2_pm = 0.728e-24; % GVD (m^-1 s^2) for PUMP
    params(i).beta2_pb = 0.622e-24; % GVD (m^-1 s^2) for PROBE
    params(i).beta3_pm = 0; % Third-order dispersion (m^-1 s^3) for PUMP
    params(i).beta3_pb = 0; % Third-order dispersion (m^-1 s^3) for PROBE
end

```

```

params(i).n2_pm      = 2.52e-17;    % Kerr coefficient (m^2/Watt) for PUMP
params(i).n2_pb      = 1.16e-17;    % Kerr coefficient (m^2/Watt) for PROBE
params(i).xn2_pm     = 0.98e-17;    % Cross Kerr coefficient (m^2/Watt) for PUMP
params(i).xn2_pb     = 0;          % Cross Kerr coefficient (m^2/Watt) for PROBE
params(i).Aeff_pm    = 7.44e-12;    % Waveguide effective area (m^2) for PUMP
params(i).Aeff_pb    = 9.85e-12;    % Waveguide effective area (m^2) for PROBE
params(i).steep_on   = 0;          % 1 to include self-steepening effect
params(i).raman_on   = 0;          % 1 to include Raman effect
params(i).Tr_pm      = 0;          % slope of Raman gain (s) for PUMP
params(i).Tr_pb      = 0;          % slope of Raman gain (s) for PROBE
params(i).alpha_pm   = 0.24e2;     % Linear loss coefficient (m^-1) for PUMP
params(i).alpha_pb   = 0.59e2;     % Linear loss coefficient (m^-1) for PROBE
params(i).alpha2_pm  = 14.5e-12;   % 2-photon absorption (m Watt^-1) for PUMP
params(i).alpha2_pb  = 5.32e-12;   % 2-photon absorption (m Watt^-1) for PROBE
params(i).xalpha2_pm = 0;          % cross 2-photon absorption (m Watt^-1) for PUMP
params(i).xalpha2_pb = 6.366e-12;  % cross 2-photon absorption (m Watt^-1) for PROBE
params(i).iterations = iterations; % number of iterations along z
params(i).numplots   = 1;          % number of points along z to return
params(i).reportpnts = 100;       % Number of points to report on-screen
params(i).deltat     = deltat;     % temporal step interval (s)
params(i).deltaz     = deltax;     % spatial step interval (m)
end;

%
% Input Pulse
%
pwr_pm = linspace(1,300,numruns); % Peak power (W) for PUMP
pwr_pb = repmat([157],1,numruns); % Peak power (W) for PROBE
FWHM   = 1.35e-12;                % Full width half maximum (s)
C      = 0.2;                     % chirp
tshift = 0; %-0.6*FWHM/1.665;
factor = 0; % 0.2;
m      = 1.0;                     % Super-gaussian factor

t = -tmax : deltat : tmax*(2*zeropadfact-1)-deltat;
q_pm = gaussian(FWHM, 1, t, C, tshift, factor, m);
q_pb = gaussian(FWHM, 1, t, C, tshift, factor, m);
%q_pm = sechpulse(FWHM, 1, t, C);
%q_pb = sechpulse(FWHM, 1, t, C);

%
% Run Simulation
%
for i=1:numruns
    qout_pm=[];
    qout_pb=[];
    z=[];
    qin_pm=q_pm.*sqrt(pwr_pm(i));
    qin_pb=q_pb.*sqrt(pwr_pb(i));
    qout_pm=[qout_pm qin_pm];
    qout_pb=[qout_pb qin_pb];
    [qout_pm, qout_pb, z, t_elapsed] = bpmxpm(params(i), qin_pm, qin_pb);
%
% Save Results
%
filename = [filepath,'\dataset','_',num2str(i,'%4u')];
save(filename);
fid = fopen([filename,'.txt'], 'w');
datetime = datestr(now, 'yyyy-mm-dd-HHhMM.SS');
fprintf(fid, '**GNLSE BPM XPM SIMULATION PARAMETERS**\n');
fprintf(fid, 'Date/Time run: %s\n', datetime);
fprintf(fid, 'Simulation time: %d\n\n', t_elapsed);
fprintf(fid, 'Description:\n%s\n\n', description);
fclose(fid);
end;

```

References

- [1] N. J. Doran and D. Wood, "Nonlinear-optical loop mirror," *Optics Letters*, vol. 13, pp. 56-58, 1988.
- [2] J. P. Sokoloff, P. R. Prucnal, I. Glesk, and M. Kane, "A terahertz optical asymmetric demultiplexer (TOAD)," *IEEE Photonics Technology Letters*, vol. 5, pp. 787-790, 1993.
- [3] G. P. Agrawal, *Nonlinear Fiber Optics*, 2 ed. San Diego: Academic Press, 1995.
- [4] Y. Silberberg and P. W. Smith, "All-Optical Guided-Wave Devices for Switching and Routing," in *Nonlinear Photonics, Springer Series in Electronics and Photonics*, H. M. Gibbs, G. Khitrova, and N. Peyghambarian, Eds. Berlin: Springer-Verlag, 1990, pp. 185-204.
- [5] H. S. Eisenberg, Y. Silberberg, R. Morandotti, A. R. Boyd, and J. S. Aitchison, "Discrete Spatial Optical Solitons in Waveguide Arrays," *Physical Review Letters*, vol. 81, pp. 3383 LP - 3386, 1998.
- [6] P. Dumais, A. Villeneuve, A. Saher-Helmy, J. S. Aitchison, L. Friedrich, R. A. Fuerst, and G. I. Stegeman, "Toward soliton emission in asymmetric GaAs/AlGaAs multiple-quantum-well waveguide structures below the half-bandgap," *Optics Letters*, vol. 25, pp. 1282-1284, 2000.
- [7] R. Salem, G. E. Tudury, T. U. Horton, G. M. Carter, and T. E. Murphy, "Polarization-Insensitive Optical Clock Recovery at 80 Gb/s Using a Silicon Photodiode," *IEEE Photonics Technology Letters*, vol. 17, pp. 1968-1970, 2005.

- [8] J. M. Ralston and R. K. Chang, "Optical Limiting in Semiconductors," *Applied Physics Letters*, vol. 15, pp. 164-166, 1969.
- [9] A. M. Streltsov, K. D. Moll, A. L. Gaeta, P. Kung, D. Walker, and M. Razeghi, "Pulse autocorrelation measurements based on two- and three-photon conductivity in GaN photodiode," *Applied Physics Letters*, vol. 75, pp. 3778-3780, 1999.
- [10] V. Mizrahi, K. W. DeLong, G. I. Stegeman, M. A. Saifi, and M. J. Andrejco, "Two-photon absorption as a limitation to all-optical switching," *Optics Letters*, vol. 14, pp. 1140-1142, 1989.
- [11] D. C. Hutchings, M. Sheik-Bahae, D. J. Hagan, and E. W. Van Stryland, "Kramers-Krönig relations in nonlinear optics," *Optical and Quantum Electronics*, vol. 24, pp. 1-30, 1992.
- [12] M. Sheik-Bahae, D. J. Hagan, and E. W. Van Stryland, "Dispersion and band-gap scaling of the electronic Kerr effect in solids associated with two-photon absorption," *Physical Review Letters*, vol. 65, pp. 96-99, 1990.
- [13] E. Garmire, "Resonant optical nonlinearities in semiconductors," *IEEE Journal of Selected Topics in Quantum Electronics*, vol. 6, pp. 1094-1110, 2000.
- [14] R. Claps, D. Dimitropoulos, V. Raghunathan, Y. Han, and B. Jalali, "Observation of stimulated Raman amplification in silicon waveguides," *Optics Express*, vol. 11, pp. 1731-1739, 2003.
- [15] H. Rong, R. Jones, A. Liu, O. Cohen, D. Hak, A. Fang, and M. Paniccia, "A continuous-wave Raman silicon laser," *Nature*, vol. 433, pp. 725-728, 2005.
- [16] P. Dainesi, A. Kung, M. Chabloz, A. Lagos, P. Fluckiger, A. Ionescu, P. Fazan, M. Declercq, P. Renaud, and P. Robert, "CMOS compatible fully integrated Mach-Zehnder interferometer in SOI technology," *IEEE Photonics Technology Letters*, vol. 12, pp. 660-662, 2000.

- [17] Q. Xu, B. Schmidt, S. Pradhan, and M. Lipson, "Micrometre-scale silicon electro-optic modulator," *Nature*, vol. 435, pp. 325-327, 2005.
- [18] V. R. Almeida, C. A. Barrios, r. R. Panepucci, and M. Lipson, "All-optical control of light on a silicon chip," *Nature*, vol. 431, pp. 1081-1084, 2004.
- [19] S. Y. Auyang and P. A. Wolff, "Free-carrier-induced third-order optical nonlinearities in semiconductors," *Journal of the Optical Society of America B*, vol. 6, pp. 595-605, 1989.
- [20] J. S. Aitchison, D. C. Hutchings, J. U. Kang, G. I. Stegeman, and A. Villeneuve, "The nonlinear optical properties of AlGaAs at the half band gap," *IEEE Journal of Quantum Electronics*, vol. 33, pp. 341-348, 1997.
- [21] J. S. Aitchison, A. H. Kean, C. N. Ironside, A. Villeneuve, and G. I. Stegeman, "Ultrafast all-optical switching in Al_{0.18}Ga_{0.82}As directional coupler in 1.55 μm spectral region," *Electronics Letters*, vol. 27, pp. 1709-1710, 1991.
- [22] P. Millar, R. M. D. L. Rue, T. F. Krauss, J. S. Aitchison, N. G. R. Broderick, and D. J. Richardson, "Nonlinear propagation effects in a AlGaAs Bragg grating filter," *Optics Letters*, vol. 24, pp. 685-687, 1999.
- [23] L. Esaki and R. Tsu, "Superlattice and Negative Differential Conductivity," *IBM Journal of Research and Development*, vol. 61, pp. 61-65, 1970.
- [24] T. Hayakawa, T. Suyama, K. Takahashi, M. Kondo, S. Yamamoto, and T. Hijikata, "Low current threshold AlGaAs visible laser diodes with an (AlGaAs)_m(GaAs)_n superlattice quantum well," *Applied Physics Letters*, vol. 49, pp. 636-638, 1986.
- [25] J. Holonyak, N., W. D. Laidig, M. D. Camras, J. J. Coleman, and P. D. Dapkus, "IR-red GaAs-AlAs superlattice laser monolithically integrated in a yellow-gap cavity," *Applied Physics Letters*, vol. 39, pp. 102-104, 1981.

- [26] A. Tredicucci, C. Gmachl, F. Capasso, D. L. Sivco, A. L. Hutchinson, and A. Y. Cho, "Long wavelength superlattice quantum cascade lasers at $\lambda = 17 \mu\text{m}$," *Applied Physics Letters*, vol. 74, pp. 638-640, 1999.
- [27] A. Tredicucci, R. Kohler, L. Mahler, H. E. Beere, E. H. Linfield, and D. A. Ritchie, "Terahertz quantum cascade lasers - first demonstration and novel concepts," *Semiconductor Science and Technology*, pp. S222-S227, 2005.
- [28] D. C. Hutchings, "Theory of ultrafast nonlinear refraction in semiconductor superlattices," *IEEE Journal of Selected Topics in Quantum Electronics*, vol. 10, pp. 1124-1132, 2004.
- [29] S. Adachi, *GaAs and Related Materials: Bulk Semiconducting and Superlattice Properties*. Singapore: World Scientific Publishing Co., 1994.
- [30] J. H. Marsh, "Quantum well intermixing," *Semiconductor Science and Technology*, vol. 6, pp. 1136-1155, 1993.
- [31] H. Leier, A. Forchel, G. Horcher, J. Hommel, S. Bayer, H. Rothfritz, G. Weimann, and W. Schlapp, "Mass and dose dependence of ion-implantation-induced intermixing of GaAs/GaAlAs quantum-well structures," *Journal of Applied Physics*, vol. 67, pp. 1805-1813, 1990.
- [32] D. C. Hutchings and T. C. Kleckner, "Quasi phase matching in semiconductor waveguides by intermixing: optimization considerations," *Journal of the Optical Society of America B*, vol. 19, pp. 890-894, 2002.
- [33] A. S. Helmy, D. C. Hutchings, T. C. Kleckner, J. H. Marsh, A. C. Bryce, J. M. Arnold, C. R. Stanley, J. S. Aitchison, C. T. A. Brown, K. Moutzouris, and M. Ebrahimzadeh, "Quasi phase matching in GaAs-AlAs superlattice waveguides through bandgap tuning by use of quantum-well intermixing," *Optics Letters*, vol. 25, pp. 1370-1372, 2000.

- [34] K. Zeaiter, D. C. Hutchings, R. M. Gwilliam, K. Moutzouris, S. V. Rao, and M. Ebrahimzadeh, "Quasi-phase-matched second-harmonic generation in a GaAs/AlAs superlattice waveguide by ion-implantation-induced intermixing," *Optics Letters*, vol. 28, pp. 911-913, 2003.
- [35] D. C. Hutchings, M. Sorel, K. Zeaiter, A. J. Zilkie, B. Leesti, A. Saher-Helmy, P. W. E. Smith, and J. S. Aitchison, "Quasi-phase-matched second harmonic generation with picosecond pulses in GaAs/AlAs superlattice waveguides," presented at *Nonlinear Guided Waves 2004 (NLGW 2004)*, 2004.
- [36] T. C. Kleckner, A. S. Helmy, K. Zeaiter, D. C. Hutchings, and J. S. Aitchison, "Dispersion and Modulation of the Linear Optical Properties of GaAs-AlAs Superlattice Waveguides Using Quantum-Well Intermixing," *IEEE Journal of Quantum Electronics*, vol. 42, pp. 280-286, 2006.
- [37] T. C. Kleckner, "Quasi-phase-matched nonlinear frequency conversion in periodically disordered GaAs/AlAs superlattice-core waveguides," Ph.D. dissertation, University of Glasgow, Glasgow, U.K., 2002.
- [38] O. P. Kowalski, C. J. Hamilton, S. D. McDougall, J. H. Marsh, A. C. Bryce, R. M. D. L. Rue, B. Vogeles, C. R. Stanley, C. C. Button, and J. S. Roberts, "A universal damage induced technique for quantum well intermixing," *Applied Physics Letters*, vol. 72, pp. 581-583, 1998.
- [39] M. W. Street, "Quantum Well Intermixing for Control of Second Order Non-linear Effects in GaAs/AlGaAs Asymmetric Quantum Well Waveguides," Ph.D. dissertation, University of Glasgow, Glasgow, Scotland, UK, 1997.
- [40] Y. Suzuki, H. Iwamura, T. Miyazawa, A. Wakatsuki, and O. Mikami, "Polarization-dependent refractive-index change induced by superlattice disordering," *IEEE Journal of Quantum Electronics*, vol. 32, pp. 1922-1931, 1996.

- [41] S. Adachi, "GaAs, AlAs, and $\text{Al}_x\text{Ga}_{1-x}\text{As}$: Material parameters for use in research and device applications," *Journal of Applied Physics*, vol. 58, pp. R1-R29, 1985.
- [42] M. A. Afromowitz, "Refractive index of $\text{Ga}_{1-x}\text{Al}_x\text{As}$," *Solid State Communications*, vol. 15, pp. 59-63, 1974.
- [43] R. J. Deri and M. A. Emanuel, "Consistent formula for the refractive index of $\text{Al}_x\text{Ga}_{1-x}\text{As}$ below the band edge," *Journal of Applied Physics*, vol. 77, pp. 4667-4672, 1995.
- [44] S. Gehrsitz, F. K. Reinhart, C. Gourgon, N. Herres, A. Vonlanthen, and H. Sigg, "The refractive index of $\text{Al}_x\text{Ga}_{1-x}\text{As}$ below the band gap: Accurate determination and empirical modeling," *Journal of Applied Physics*, vol. 87, pp. 7825-7837, 2000.
- [45] R. S. Grant, "Effective non-linear coefficients of optical waveguides," *Optical and Quantum Electronics*, vol. 28, pp. 1161-1173, 1996.
- [46] G. Keiser, *Optical Fiber Communications*, 3 ed. Boston: McGraw-Hill, 2000.
- [47] D. F. Clark and M. S. Iqbal, "Simple extension to the Fabry-Perot technique for accurate measurement of losses in semiconductor waveguides," *Optics Letters*, vol. vol 15, pp. 1291-1293, 2006.
- [48] A. J. Zilkie, "Characterization of the Linear and Nonlinear Absorption Dynamics of AlGaInAs Strained-Layer Multiple-Quantum-Well Semiconductor Optical Amplifiers," M.A.Sc. thesis, University of Toronto, Toronto, 2004.
- [49] J. S. Aitchison, C. J. Hamilton, M. W. Street, N. D. Whitbread, D. C. Hutchings, J. H. Marsh, G. T. Kennedy, and W. Sibbett, "Control of the second- and third-order nonlinearities in GaAs-AlGaAs multiple quantum wells," *Pure and Applied Optics*, vol. 7, pp. 327-333, 1998.

- [50] B. S. Wherrett, "Scaling rules for multiphoton interband absorption in semiconductors," *Journal of Optical Society of America B*, vol. 1, pp. 67-72, 1984.
- [51] M. Dinu, "Dispersion of Phonon-Assisted Nonresonant Third-Order Nonlinearities," *IEEE Journal of Quantum Electronics*, vol. 39, pp. 1298-1503, 2003.
- [52] W. L. Smith, "Two-Photon Absorption in Condensed Media," in *CRC Handbook of Laser Science and Technology*, vol. 3, M. J. Weber, Ed. Boca Raton, Florida, USA: CRC Press, 1986, pp. 259-282.
- [53] J. U. Kang, "Spatial Solitons in AlGaAs Waveguides," Ph.D. dissertation, University of Central Florida, Orlando, Florida, 1996.
- [54] M. Dinu, F. Quochi, and H. Garcia, "Third-order nonlinearities in silicon at telecom wavelengths," *Applied Physics Letters*, vol. 82, pp. 2954-2956, 2003.
- [55] A. Villeneuve, M. Sundheimer, N. Finlayson, G. I. Stegeman, S. Morasca, C. Rigo, R. Calvani, and C. D. Bernardi, "Two-photon absorption in $\text{In}_{1-x-y}\text{Ga}_x\text{Al}_y\text{As}/\text{InP}$ waveguides at communications wavelengths," *Applied Physics Letters*, vol. 56, pp. 1865-1867, 1990.
- [56] D. C. Hutchings and B. S. Wherrett, "Theory of anisotropy of two-photon absorption in zinc-blende semiconductors," *Physical Review B*, vol. 49, pp. 2418-2427, 1994.
- [57] M. N. Islam, C. E. Socolich, R. E. Slusher, A. F. J. Levi, W. S. Hobson, and M. G. Young, "Nonlinear spectroscopy near half-gap in bulk and quantum well GaAs/AlGaAs waveguides," *Journal of Applied Physics*, vol. 71, pp. 1927-1935, 1992.

- [58] C. C. Yang, A. Villeneuve, G. I. Stegeman, C. H. Lin, and H. H. Lin, "Measurements of two-photon absorption coefficient and induced nonlinear refractive index in GaAs/AlGaAs multiquantum well waveguides," *Electronics Letters*, vol. 29, pp. 37, 1993.
- [59] M. Sheik-Bahae, D. C. Hutchings, D. J. Hagan, and E. W. Van Stryland, "Dispersion of bound electron nonlinear refraction in solids," *IEEE Journal of Quantum Electronics*, vol. 27, pp. 1296-1309, 1991.
- [60] J. U. Kang, A. Villeneuve, M. Sheik-Bahae, G. I. Stegeman, K. Al-hemyari, J. S. Aitchison, and C. N. Ironside, "Limitation due to three-photon absorption on the useful spectral range fo nonlinear optics in AlGaAs below half band gap," *Applied Physics Letters*, vol. 65, pp. 147-149, 1994.
- [61] M. Sheik-bahaei, P. Mukherjee, and H. S. Kwok, "Two-photon and three-photon absorption coefficient of InSB," *Journal of the Optical Society of America B*, vol. 3, pp. 379-385, 1986.
- [62] D. Modotto, J. P. Mondia, S. Linden, H. W. Tan, R. Morandotti, T. C. Kleckner, A. Locatelli, C. D. Angelis, H. M. v. Driel, C. R. Stanley, and J. S. Aitchison, "Asymmetric spectrum evolution of high power short pulses in AlGaAs," *Optics Communications*, vol. 249, pp. 201-208, 2005.
- [63] O. Boyraz, T. Indukuri, and B. Jalali, "Self-phase-modulation induced spectral broadening in silicon waveguides," *Optics Express*, vol. 12, pp. 829-834, 2004.
- [64] D. C. Hutchings and B. S. Wherrett, "Theory of the anisotropy of ultrafast nonlinear refraction in zinc-blende semiconductors," *Physical Review B*, vol. 52, pp. 8150-8159, 1995.
- [65] D. C. Hutchings, J. S. Aitchison, B. S. Wherrett, G. T. Kennedy, and W. Sibbett, "Polarization dependence of ultrafast nonlinear refraction in an AlGaAs waveguide at the half-band gap," *Optics Letters*, vol. 20, pp. 991-993, 1995.

- [66] C. J. Hamilton, J. H. Marsh, D. C. Hutchings, J. S. Aitchison, G. T. Kennedy, and W. Sibbett, "Localized Kerr-type nonlinearities in GaAs/AlGaAs multiple quantum well structures at 1.55 μm ," *Applied Physics Letters*, vol. 68, pp. 3078-3080, 1996.
- [67] J. L. T. Waugh and G. Dolling, "Crystal Dynamics of Gallium Arsenide," *Physical Review*, vol. 132, pp. 2410-2412, 1963.
- [68] D. C. Hutchings, "Electronic bandstructure of disordered superlattices," *Superlattices and Microstructures*, vol. 26, pp. 195-209, 1999.
- [69] P. N. Butcher and D. Cotter, *The Elements of Nonlinear Optics*, vol. 9. Cambridge, UK: Cambridge University Press, 1990.
- [70] M. Sheik-Bahae, A. A. Said, T.-H. Wei, D. J. Hagan, and E. W. Van Stryland, "Sensitive measurement of optical nonlinearities using a single beam," *IEEE Journal of Quantum Electronics*, vol. 26, pp. 760-769, 1990.
- [71] A. Villeneuve, J. U. Kang, J. S. Aitchison, and G. I. Stegeman, "Unity ratio of cross- to self-phase modulation in bulk AlGaAs and AlGaAs/GaAs multiple quantum well waveguides at half the band gap," *Applied Physics Letters*, vol. 67, pp. 760-762, 1995.
- [72] P. K. Tien, "Integrated optics and new wave phenomena in optical waveguides," *Reviews of Modern Physics*, vol. 49, pp. 361-420, 1977.
- [73] S. Jensen, "The nonlinear coherent coupler," *IEEE Journal of Quantum Electronics*, vol. 18, pp. 1580-1583, 1982.
- [74] A. Villeneuve, C. C. Yang, P. G. J. Wigley, G. I. Stegeman, J. S. Aitchison, and C. N. Ironside, "Ultrafast all-optical switching in semiconductor nonlinear directional couplers at half the band gap," *Applied Physics Letters*, vol. 61, pp. 147-149, 1992.

- [75] P. LiKamWa, A. Miller, J. S. Roberts, and P. N. Robson, "130 ps recovery of all-optical switching in a GaAs multiquantum well directional coupler," *Applied Physics Letters*, vol. 58, pp. 2055-2057, 1991.
- [76] K. W. DeLong, K. B. Rochford, and G. I. Stegeman, "Effect of two-photon absorption on all-optical guided-wave devices," *Applied Physics Letters*, vol. 55, pp. 1823-1825, 1989.
- [77] G. Stegeman and E. Wright, "All-optical waveguide switching," *Optical and Quantum Electronics*, vol. 22, pp. 95-122, 1990.
- [78] K. Al-Hemyari, J. S. Aitchison, C. N. Ironside, G. T. Kennedy, R. S. Grant, and W. Sibbett, "Ultrafast all-optical switching in GaAlAs integrated interferometer in 1.55 μm spectral region," *Electronics Letters*, vol. 28, pp. 1090-1092, 1992.
- [79] A. M. Kan'an, P. LiKamWa, Mitra-Dutta, and J. Pamulapati, "Area-selective disordering of multiple quantum well structures and its applications to all-optical devices," *Journal of Applied Physics*, vol. 80, pp. 3179-3183, 1996.
- [80] D. C. Hutchings, University of Glasgow (personal communication, 2006)